

**ON THE REGIOSELECTIVITY OF H-ATOM ABSTRACTION  
FROM MODEL POLYOLEFINS BY ALKOXYL RADICALS**

by

Graham E. Garrett

A thesis submitted to the Department of Chemical Engineering  
In conformity with the requirements for  
the degree of Masters of Applied Science in Chemical Engineering

Queen's University  
Kingston, Ontario, Canada  
(October, 2011)

Copyright © Graham E. Garrett, 2011

## Abstract

Solvent-free peroxide-initiated polymer modifications are widely used to improve the physical and/or chemical properties of commodity plastics and elastomers. Although the reactions that underlie polymer grafting are known, our understanding of H-atom transfer reactions in this context is incomplete. Fundamental questions remain unanswered, such as the difference in reactivity between different polymers (polyethylene versus polypropylene and polyisobutylene) and differences in the regiochemical outcomes of grafting reactions upon them. Herein, experimental data pertaining to the H-atom transfers involved in polyolefin graft modifications were obtained to improve our fundamental understanding of these reactions by using radical-trapping techniques and quantum chemical calculations. In this project, experimental measurements of the efficiency of H-atom abstraction by *t*-butoxyl radicals from polyolefins, and suitable model compounds such as pentane, 2,4-dimethylpentane and 2,2,4,4-tetramethylpentane were determined. Insight is gained from alkyl-trapping experiments to quantify the relative reactivities of the primary, secondary and tertiary positions of the model compounds. Experimental data were compared to quantum chemical calculations, which revealed that entropic effects dictate the regioselectivity and preclude abstraction at the secondary position in favour of the less enthalpically-favourable primary abstraction site. MP2 and CBS-QB3 level calculations were able to reproduce experimental trends in model compound reactivity, while the highly common B3LYP density functional, used in other investigations on the subject, could not.

## **Acknowledgements**

I would like to thank Professors Derek Pratt and Scott Parent for their help and supervision throughout the course of my research. I would also like to thank my family for their support throughout my university career, as well as the members of the Chemical Engineering and Chemistry Departments at Queen's university, especially my lab colleagues in the Parent and Pratt groups. I would also like to acknowledge NSERC and DuPont for providing me with the funding to undertake this research project.

I would like to extend a large thank you to Jason J. Hanthorn for his assistance and guidance in the preparation of the radical trap used in this study.

## Table of Contents

Chapter 1.....	1
1.1 Polyolefin modification .....	1
1.2 Objective .....	4
1.3 Regioselectivity in model compounds .....	4
1.4 Quantum mechanical calculations .....	9
1.4.1 Computational methods .....	10
1.4.2 Assessing the methods .....	19
1.5 Thermochemistry in quantum chemical calculations.....	20
1.6 Quantum chemical calculations for H-atom abstractions .....	22
Chapter 2 Investigating the Regioselectivity of H-atom Transfer in Polymer Model Compounds	
Using the Radical Trapping Technique .....	25
2.1 Introduction.....	25
2.2 Results.....	26
2.2.1 Synthesis of di- <i>t</i> -butyl hyponitrite (DTBH).....	26
2.2.2 Complete synthesis of 1,1,3,3-tetramethylisindolin-2-oxyl (TMIO) .....	27
2.2.2.1 Synthesis of N-benzylphthalimide .....	27
2.2.2.2 Synthesis of 2-benzyl-1,1,3,3-tetramethylisindoline .....	27
2.2.2.3 Synthesis of 1,1,3,3-tetramethylisindoline.....	28
2.2.2.4 Synthesis of 1,1,3,3-tetramethylisindolin-2-yloxy.....	29
2.2.3 Characterization of model compound derivatives.....	29
2.2.4 Alkoxyamine product distributions.....	36
2.3 Discussion.....	38
2.4 Experimental.....	44
2.4.1 General data .....	44
2.4.2 Substrates .....	45
2.4.3 Radical trapping experiments.....	45
Chapter 3 Investigating the Regioselectivity of H-Atom Transfer in Polymer Model Compounds	
Using Quantum Chemical Calculations .....	47
3.1 Introduction.....	47
3.2 Results.....	48
3.2.1 Bond dissociation enthalpies.....	48
3.2.2 Thermodynamic parameters.....	50

3.2.2.1 Reaction thermodynamics.....	51
3.2.2.2 Transition state thermodynamics .....	52
3.2.3 Estimating rate constants and preexponential factors .....	54
3.2.4 Product Distributions .....	59
3.2.5 Transition state structures .....	60
3.3 Discussion.....	62
3.4 Methods of calculations .....	70
Chapter 4 Conclusions: Combining Experimentally Obtained Data with Quantum Chemical	
Calculations .....	71
4.1 Conclusions.....	71
4.2 Future work.....	72
Appendix A Miscellaneous computational data .....	76
Product Distributions .....	77
Pentane.....	77
2,4-Dimethylpentane.....	77
2,2,4,4-Tetramethylpentane .....	77
Appendix B Characterization of radically trapped products.....	78
Pentane derivatives .....	78
2,4-Dimethylpentane derivatives .....	88
2,2,4,4-Tetramethylpentane derivatives.....	108

## List of Figures

Figure 1-1: Slater and Gaussian type functions as a function of nuclear distance for an s orbital.	15
Figure 1-2: Three different primitive Gaussian type functions contracted to estimate a Slater type orbital. ....	16
Figure 3-1: Computed geometries of transition structures for H-atom abstraction from 2,2,4,4-tetramethylpentane (TMP) by: a) <i>t</i> -butoxyl; and b) methoxyl radicals at the CBS-QB3 level of theory. ....	60
Figure 3-2: Computed geometries of transition structures for H-atom abstraction from 2,4-dimethylpentane (DMP) by: a) <i>t</i> -butoxyl; and b) methoxyl radicals at the CBS-QB3 level of theory. ....	61
Figure B1: <sup>1</sup> H NMR spectrum of PEN-p with peak assignments referenced to chloroform at 7.26 ppm. ....	79
Figure B2: Aliphatic region of the <sup>1</sup> H NMR of PEN-p with peak assignments referenced to chloroform at 7.26 ppm. ....	80
Figure B3: <sup>13</sup> C NMR of PEN-p with peak assignments referenced to chloroform at 77.00 ppm. ....	81
Figure B4: <sup>1</sup> H NMR of the mixture of secondary products, PNE-s and PEN-s' referenced to chloroform at 7.26 ppm. ....	83
Figure B5: GS-MS injection trace of the PEN-s and PEN-s' mixture after HPLC separation. ....	84
Figure B6: Crude GC-MS injection of the PEN radical trapping experiment. ....	85
Figure B7: GS-MS injection trace of PEN-p after HPLC separation. ....	86
Figure B8: 10 μL HPLC injection in 85:15 MeOH:H <sub>2</sub> O of the crude pentane radical trapping reaction mixture. ....	87
Figure B9: <sup>1</sup> H NMR spectra of DMP-p with peak assignments referenced to chloroform at 7.26 ppm. ....	89
Figure B10: Aliphatic region of the <sup>1</sup> H NMR of DMP-p with peak assignments referenced to chloroform at 7.26 ppm. ....	90
Figure B11: COSY 2D NMR of DMP-p from 4.00 to 0.00 ppm with correlation assignments. ....	91
Figure B12: Aliphatic region of the 2D COSY NMR of DMP-p from 2.00 to 0.50 ppm with correlation assignments. ....	92
Figure B13: <sup>13</sup> C NMR of DMP-p with peak assignments referenced to chloroform at 77.00 ppm. ....	93
Figure B14: Aliphatic region of the HSQC 2D NMR of DMP-p with correlation assignments. ....	94
Figure B15: <sup>1</sup> H NMR of DMP-s with peak assignments referenced to chloroform at 7.26 ppm. ....	96

Figure B16: Aliphatic region of the $^1\text{H}$ NMR of DMP-s with peak assignments referenced to chloroform at 7.26 ppm.....	97
Figure B17: COSY 2D NMR of DMP-p from 4.00 to 0.85 ppm with correlation assignments....	98
Figure B18: $^{13}\text{C}$ NMR of DMP-s with peak assignments referenced to chloroform at 77.00 ppm. .....	99
Figure B19: Full HSQC 2D NMR spectra of DMP-s with correlation assignments. ....	100
Figure B20: Aliphatic region of the HSQC 2D NMR of DMP-s with correlation assignments..	101
Figure B21: Full $^1\text{H}$ NMR of DMP-t with peak assignments referenced to chloroform at 7.26 ppm. ....	103
Figure B22: Aliphatic region of the $^1\text{H}$ NMR of DMP-t with peak assignments. ....	104
Figure B23: COSY 2D NMR of the aliphatic region of DMP-t from 2.00 to 0.60 ppm with peak correlation assignments.....	105
Figure B24: Full $^{13}\text{C}$ NMR spectra of DMP-t with peak assignments referenced to chloroform at 77.00 ppm. ....	106
Figure B25: Aliphatic region of the HSQC 2D NMR of DMP-t with correlation peak assignments. ....	107
Figure B26: $^1\text{H}$ NMR of TMP-p with peak assignments referenced to chloroform at 7.26 ppm.	109
Figure B27: $^{13}\text{C}$ NMR of TMP-p with peak assignments referenced to chloroform at 77.00 ppm. .....	110
Figure B28: HSQC 2D NMR of TMP-p.....	111
Figure B29: $^1\text{H}$ NMR of TMP-s with peak assignments referenced to chloroform at 77.00 ppm. .....	113
Figure B30: Full $^{13}\text{C}$ NMR of TMP-s with peak assignments referenced to chloroform at 77.00 ppm. ....	114
Figure B31: Aliphatic region of the HSQC 2D NMR of TMP-s. ....	115

## List of Tables

Table 1-1: Some C-H BDEs of carbon-centered radicals (kcal/mol). .....	6
Table 2-1: Carbon and hydrogen NMR peak assignments for PEN-p.....	30
Table 2-2: Carbon and hydrogen NMR peak assignments for DMP-p.....	32
Table 2-3: Carbon and hydrogen NMR peak assignments for DMP-s. ....	33
Table 2-4: Carbon and hydrogen NMR peak assignments for DMP-t.....	33
Table 2-5: Carbon and hydrogen NMR peak assignments for TMP-p.....	34
Table 2-6: Carbon and hydrogen NMR peak assignments for TMP-s.....	35
Table 2-7:High-Res MS results and retention times for the TMIO radical trapped model compound products.....	35
Table 2-8: Relative yields and reactivity of model compounds towards <i>t</i> -butoxyl radicals at room temperature, determined by HPLC. ....	37
Table 3-1 Calculated Bond Dissociation Energies (BDE) $\Delta H^{\circ}_{298}$ in kcal/mol .....	49
Table 3-2: Thermodynamic reaction parameters in kcal/mol or cal/molK of the <i>t</i> -butoxyl and methoxyl H-atom abstraction as a function of the level of theory.....	51
Table 3-3: $\Delta H^{\ddagger}$ values in kcal/mol of the <i>t</i> -butoxyl and methoxyl H-atom abstraction as a function of the level of theory. ....	52
Table 3-4: $\Delta S^{\ddagger}$ values in kcal/mol of the <i>t</i> -butoxyl and methoxyl H-atom abstraction as a function of the level of theory .....	53
Table 3-5: $\Delta G^{\ddagger}$ values in kcal/mol of the <i>t</i> -butoxyl and methoxyl H-atom abstraction as a function of the level of theory.....	54
Table 3-6: logA values for the <i>t</i> -butoxyl radical H-atom abstraction as a function of the level of theory. ....	56
Table 3-7: Estimated rate constants, $k_{298} \times 10^{-2} (M^{-1}s^{-1})$ , for H-atom abstraction from the model compounds by <i>t</i> -butoxyl radicals as a function of the level of theory. ....	56
Table 3-8: Estimated rate constants, $k_{298} \times 10^{-2} (M^{-1}s^{-1})$ , for H-atom abstraction from the model compounds by methoxyl radicals as a function of the level of theory.....	56
Table 3-9: Estimated rate constants, $k_{298} \times 10^{-2} (M^{-1}s^{-1})$ , for H-atom abstraction from the model compounds by <i>t</i> -butoxyl and methoxyl radicals at the CBS-QB3 level of theory.....	57
Table 3-10: Estimated relative reactivity, $k_{298} \times 10^{-2} (M^{-1}s^{-1})$ , for H-atom abstraction from the model compounds by <i>t</i> -butoxyl and methoxyl radicals at the CBS-QB3 level of theory .....	58
Table 3-11: Estimated relative reactivity, $k_{298} \times 10^{-2} (M^{-1}s^{-1})$ , for the H-atom abstraction from the polymers by <i>t</i> -butoxyl and methoxy radicals at the CBS-QB3 level of theory.....	58



Table 3-12: Estimated product distributions of radical trapping experiments from rate constants calculated at 25 °C as a function of the level of theory.....	59
Table B4-1: Carbon and hydrogen NMR peak assignments for PEN-p .....	82
Table B4-2: Carbon and hydrogen NMR peak assignments for DMP-p. ....	95
Table B4-3: Carbon and hydrogen NMR peak assignments for DMP-s. ....	102
Table B4-4: Carbon and hydrogen NMR peak assignments for DMP-t. ....	108
Table B4-5: Carbon and hydrogen NMR peak assignments for TMP-p. ....	112
Table B4-6: Carbon and hydrogen NMR peak assignments for TMP-s. ....	116

## List of Abbreviations

AM1	Austin Model 1
BDE	Bond Dissociation Enthalpy
CCSD(T)	Couple Cluster Singlet and Doublet with some Triplet excitations
DFT	Density Functional Theory
DMP	2,4-Dimethylpentane
DMP-p	2-(2,4-Dimethylpentyloxy)-1,1,3,3-tetramethylisoindoline
DMP-s	2-(2,4-Dimethylpentan-3-yloxy)-1,1,3,3-tetramethylisoindoline
DMP-t	2-(2,4-Dimethylpentan-2-yloxy)-1,1,3,3-tetramethylisoindoline
DTBH	Di- <i>tert</i> -butyl hyponitrite
EPR	Electron Paramagnetic Resonance
Full CI	Full Configuration Interaction
GC-MS	Gas Chromatography coupled Mass Spectroscopy
HAT	H-atom Transfer
HF	Hartree Fock
HPLC	High Performance Liquid Chromatography
MSE	Mean Squared Error
MP2	second order Møller Plesset perturbation theory
PE	Polyethylene
PEN	Pentane
PEN-p	1,1,3,3-Tetramethyl-2-(pentyloxy)isoindoline
PEN-s	1,1,3,3-Tetramethyl-2-(pentan-2-yloxy)isoindoline
PEN-s'	1,1,3,3-tetramethyl-2-(pentan-3-yloxy)isoindoline
PIB	Polyisobutylene
PP	Polypropylene
PM3	Parameterized Model 3
TMIO	1,1,3,3-Tetramethylisoindolin-2-yloxy
TMP	2,2,4,4-Tetramethylpentane
TMP-p	1,1,3,3-Tetramethyl-2-(2,2,4,4-Tetramethylpentan-3-yloxy)isoindoline
TMP-s	1,1,3,3-Tetramethyl-2-(2,2,4,4-Tetramethylpentyloxy)isoindoline

## List of Symbols

$h$	Plank's constant
$\Delta G^\ddagger$	Gibbs Energy barrier to the reaction
$k$	Rate constant
$k_B$	Boltzmann constant
$K_{\text{HAT}_{\text{DMP}}}$	Overall H-atom abstraction rate constant for 2,4-dimethylpentane
$K_{\text{HAT}_{\text{PEN}}}$	Overall H-atom abstraction rate constant for pentane
$K_{\text{HAT}_{\text{PE}}}$	Overall H-atom abstraction rate constant for polyethylene
$K_{\text{HAT}_{\text{PIB}}}$	Overall H-atom abstraction rate constant for polyisobutylene
$K_{\text{HAT}_{\text{PP}}}$	Overall H-atom abstraction rate constant for polypropylene
$K_{\text{HAT}_{\text{TMP}}}$	Overall H-atom abstraction rate constant for 2,2,4,4-tetramethylpentane
$K_P$	Total H-atom abstraction reaction rate constant for the primary position
$K_S$	Total H-atom abstraction reaction rate constant for the secondary position
$K_T$	Total H-atom abstraction reaction rate constant for the tertiary position
$k_p$	H-atom abstraction reaction rate constant at the primary position
$k_s$	H-atom abstraction reaction rate constant at the secondary position
$k_t$	H-atom abstraction reaction rate constant at the tertiary position
$P$	Pressure.
$R$	Ideal gas constant
$T$	Temperature

# Chapter 1

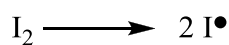
## Introduction

### 1.1 Polyolefin modification

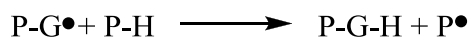
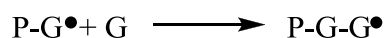
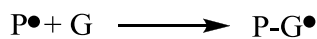
Solvent-free peroxide-initiated grafting reactions are used widely to alter the physical and/or chemical properties of polymers for commodity plastics and elastomers.<sup>1</sup> Graft copolymerization is one of the main methods used to modify polymers and is almost always achieved through a free radical reaction process, beginning with hydrogen atom (H-atom) abstraction from the polymer backbone. In the case of polypropylene (PP), after graft copolymerization the modified polymer generally has superior stability, dyeability, and hygroscopicity than the unmodified substrate.<sup>2</sup> For example, after grafting vinyl acetate on PP, the resulting copolymer gained enhanced mechanical, thermal and dyeability properties,<sup>3</sup> while copolymerization with butyl methacrylate improved the impact strength.<sup>4</sup> The adhesive and coating properties of PP can also be improved through free radical graft copolymerization; grafting with maleic anhydride can produce tear and peel resistant adhesives.<sup>5</sup>

The amenability of a polymer with respect to modification, and the structure of the graft-modified product, is dictated to a great extent by H-atom transfer reactions. Ideally, efficient H-atom transfer from the polymer to peroxide-generated initiator radicals provides a high yield of (polymer-derived) ‘macro-radicals’. These macro-radicals propagate through addition and H-atom transfer reactions to yield the grafted product. The efficiency of H-atom transfer is one of the main factors which control the overall yield of graft modified product per macro-radical initiated.

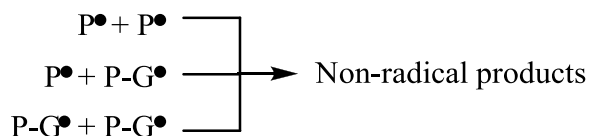
### Initiation



### Propagation



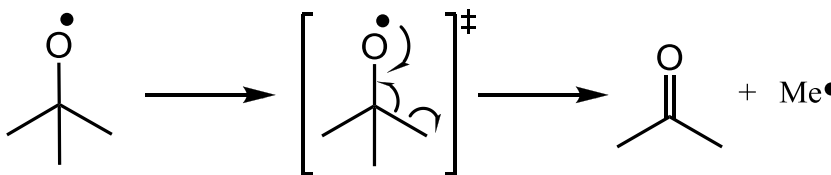
### Termination



**Scheme 1-1:** Reaction stages in graft copolymerization.

Scheme 1-1 shows the reaction steps relevant in this study for graft copolymerization reactions. Reactions are typically initiated by peroxide degradation. In the case of initiation by di-*t*-butyl peroxide, cleavage of the weak oxygen-oxygen bond ( $38.9 \pm 0.5$  for dimethyl peroxide at 25 °C)<sup>6</sup> produces two *t*-butoxyl radicals. Hydrogen abstraction from the polymer by a *t*-butoxyl radical can then occur. This produces *t*-butanol and a polymer macro-radical. Grafting is then possible and occurs through addition reactions with the polymer macro-radical and graft monomers. The regioselectivity of the grafting process is largely dictated by H-atom transfer reactions, whereby another H-atom is abstracted from the polymer backbone by the remaining radical on the graft chain. This sequence of reactions are the propagation steps, since they yield macro-radicals that can continue the chain reaction. The reaction then ends when two radicals combine to form an electron pair, or disproportionation occurs where hydrogen transfer occurs adjacent to a radical position creating a double bond instead of a propagating radical. These reactions are denoted as termination reactions.

Initiation of the free radical grafting process by peroxide degradation is driven by the higher hydrogen abstraction reaction rate with C-H bonds on the polymer back bone than recombination or radical addition reactions to a graft monomer. Monomers are generally electron deficient olefins; the electrophilic *t*-butoxyl radicals<sup>7</sup> therefore prefer hydrogen abstraction. For example, the bimolecular rate constant for the addition of *t*-butoxyl to methyl methacrylate at 60 °C is in the order of  $10^4 - 10^5 \text{ M}^{-1}\text{s}^{-1}$ ;<sup>8</sup> to compare, the rate constant for hydrogen atom abstraction from cyclohexene by *t*-butoxyl is  $5.4 \times 10^6 \text{ M}^{-1}\text{s}^{-1}$ .<sup>9</sup> The regioselectivity of this abstraction will dictate the location of grafting in the subsequent steps as monomer addition occurs in the propagation stages of copolymerization.



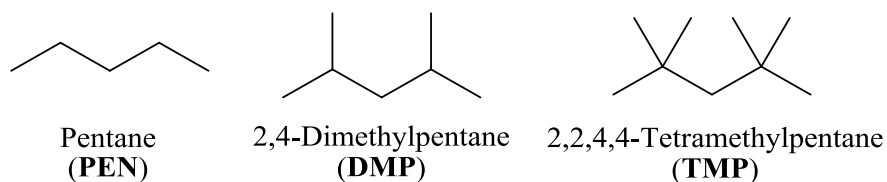
**Scheme 1-2:** The  $\beta$ -scission of *t*-butoxyl to form acetone and a methyl radical

One deterrent to initiation of graft copolymerization is the  $\beta$ -scission reactions of alkoxy radicals shown for *t*-butoxyl in Scheme 1-2.  $\beta$ -Scission is a unimolecular process whereby the alkoxy radical degrades to form a carbonyl and an alkyl radical.<sup>10</sup> In the case of *t*-butoxyl, this process produces acetone and a methyl radical with a rate constant of  $1.9 \times 10^5 \text{ s}^{-1}$  at 60 °C in benzene.<sup>8</sup> This rate constant varies slightly for different alkoxy radicals with the cumyloxy radical undergoing  $\beta$ -scission with a rate constant of  $2.6 \times 10^5 \text{ s}^{-1}$  in carbon tetrachloride at room temperature.<sup>11</sup>  $\beta$ -Scission reactions are also solvent dependent, higher polarity solvents will stabilize the transition state through increased solvation of the incipient carbonyl product.<sup>10,11</sup> In graft copolymerizations, substrates which are less reactive towards H-atom transfer will have greater proportions of  $\beta$ -scission products. Not only does  $\beta$ -scission decompose the initiator, the

alkyl radical produced can now participate in termination reactions. This causes an overall decrease in macro-radical yields.

## 1.2 Objective

Although these reactions that underlie polymer grafting are known, our understanding of H-atom transfer reactions is incomplete. Fundamental questions remain unanswered, such as the origin of differences in reactivity between various polymers. This project aims to quantify the difference in reactivity between different polymers (polyethylene (PE), polypropylene (PP) and polyisobutylene (PIB)) using suitable model compounds and quantum chemical calculations. In the case of PE, only one type of H-atom is present in the backbone and regioselectivity is not an issue. However, for PP, there are now primary, tertiary and secondary carbon-hydrogen bonds present, while PIB contains only primary and secondary positions. For these two polymers the reactivity at each carbon centre must be determined if one wants to understand the overall reactivity of the polymer. A convenient method to accomplish this involves experimental measurements of the regioselectivity of H-atom abstraction by *t*-butoxyl radicals from suitable model compounds. Used herein, and shown in Scheme 1-3, are pentane (PEN) for PE, 2,4-dimethylpentane (DMP) for PP, and 2,2,4,4-tetramethylpentane (TMP) for PIB.



**Scheme 1-3:** Polyolefin model compounds used in this study.

## 1.3 Regioselectivity in model compounds

The treatment and analysis using polymer model compounds is simplified over the treatment of polymer species and provides a convenient method for investigating polymer reactivity. The reaction conditions required for H-atom abstraction from model compounds does

not require the high temperatures required to reach the polymer melt state. At ambient temperatures, the model compounds used here are all liquid. Therefore H-atom abstraction reactions can be carried out at temperatures up to the boiling point of these liquids at ambient pressures without the need of pressurizing vessels. Carrying out these reactions in dilute neat solutions with adequate mixing also limits multiple abstractions from the same compound occurring, further simplifying the analysis. The regioselectivity of these reactions can be easily investigated using High Performance Liquid Chromatography (HPLC).

Some of the differences in results from model compound studies, compared to their polymer analogues, have been noted in the literature. For H-atom abstractions, reaction rates in model compounds are higher than those in polymers due to the chain folding, coiling, and entanglement of the polymer.<sup>12</sup> This shelters the H-atom abstraction sites and hinders the approach of the initiating radical. In extension to this, the regioselectivity of chain transfer reactions that occur in the propagation stage of graft copolymerization will be more sensitive to steric crowding. During chain transfer the carbon-centered radical is on a considerably bulkier center than the oxygen atom during initiation. Because of this, chain transfer reactions will be more selective for less hindered sites. The regioselectivity of these reactions has been studied through EPR experiments<sup>13</sup> on model compounds, as well as EPR studies on polymer and model reactivities<sup>14</sup> and competition experiments.<sup>15</sup> However, the factors that contribute to regioselectivity have not yet been fully studied. Enthalpic and steric effects that play a role in the regioselectivity and reactivity of polymer grafting reactions are not yet understood.

The reactivity of carbon-hydrogen bonds towards radical abstraction generally follows the established trend from carbocation and carbanion stabilization.<sup>16,17</sup> Radicals experience the same hyperconjugative stabilization effects as carbocations.<sup>18</sup> In radicals, hyperconjugation is the delocalization of the unpaired electron to sigma bonded neighbouring groups via the p-orbitals; this interaction stabilizes the radical and lowers the bond dissociation energy of the C-H bond, see

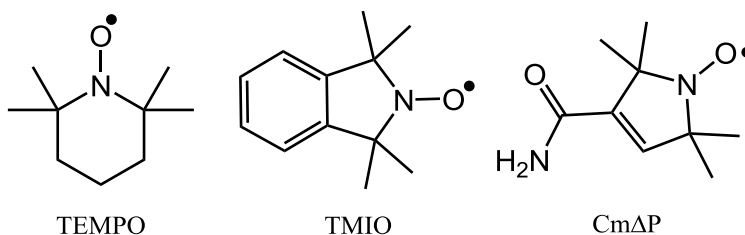


Table 1-1. Based on bond strengths, and in the absence of steric effects, abstraction is expected predominantly at the tertiary position, followed by the secondary, and then the primary positions.

**Table 1-1:** Some C-H BDEs of hydrocarbons (kcal/mol).<sup>18</sup>

Radical formed, R•	R-H BDE
H <sub>3</sub> C•	105.0
H <sub>3</sub> CCH <sub>2</sub> •	101.1
(H <sub>3</sub> C) <sub>2</sub> CH•	98.6
(H <sub>3</sub> C) <sub>3</sub> C•	96.5

Recent work on H-atom abstraction regioselectivity in polymers and model compounds has revealed that this trend is not carried over to these systems. Experimentally, this selectivity has been studied on model PP compounds by Dokolas et al.<sup>19,20</sup> using the trapping technique of Rizzardo and Solomon.<sup>21</sup> This technique relies on the near diffusion controlled reaction rate ( $10^{-7}$  –  $10^{-9}$  M<sup>-1</sup> s<sup>-1</sup>) of nitroxyl radicals combining with alkyl centered radicals to afford relatively stable alkoxyamines.<sup>22</sup> This reaction occurs faster than any subsequent H-atom transfer reaction, and the low reaction rate with oxygen-centered radicals prevents the trapping agent from halting initiation, and any reaction with oxygen-centered radicals (e.g. initiating alkoxy) will yield unstable products which simply decompose back to the starting oxygen-centered radicals. The trapping agent's lack of reactivity with monomers also ensures that propagation continues.<sup>21</sup>

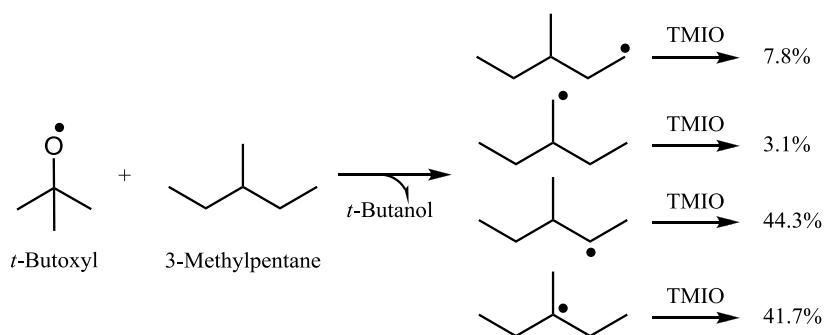


**Scheme 1-4:** Some popular nitroxyls used as radical traps in the literature.

Illustrated in Scheme 1-4 are several nitroxyls that are commonly used in the literature. Herein we employ the TMIO radical trap which contains a chromophore that can be used to

locate the trapped compounds using UV-spectroscopy. After trapping, the products can be separated by HPLC and the relative yields of each product determined to calculate the relative reaction rate at each location.

Carrying out the study on DMP and 3-methylpentane and using di-*t*-butyl peroxalate as a low temperature source of *t*-butoxyl radicals, Dokolas<sup>19</sup> found that in neat 3-methylpentane, tertiary and secondary abstraction made up approximately 90% of the products. The overall reactivity at each site in 3-methylpentane was determined to be 39.7 (tertiary) : 10.2 (secondary) : 1.3 (primary acyclic methyl) : 1.0 (primary branched methyl) and noting that per hydrogen, the tertiary (i.e. methine) C-H bond is 3.9 times more reactive towards H-atom abstraction than a methylene hydrogen.



**Scheme 1-5:** Results obtained by Dokolas for the *t*-butoxyl initiated radical trapping experiment on 3-methylpentane using TMIO as the nitroxyl radical trap.<sup>19</sup>

Their results are presented in Scheme 1-5. When carrying out the same reaction in benzene the regioselectivity remained unchanged, but the overall reactivity fell and a higher yield of the  $\beta$ -scission product<sup>10</sup> was obtained. To ensure the observed product ratios were the result of trapping the first formed carbon-centered radical, and not from rapid rearrangement followed by radical-trapping, the researchers increased the nitroxyl concentration. They found no change in the product distribution and concluded that the resultant alkoxyamines were formed from the first created carbon-centered radicals.

When carrying out the same reactions on DMP, Dokolas<sup>19</sup> found a decrease in overall yield when compared to 3-methylpentane and in neat solution found relative yields of 67.3 (tertiary) : 23.9 (primary) : 9.1 (secondary) for the trapped alkoxyamine products. In contrast to 3-methylpentane where the ratios remained largely unchanged in benzene, in the case of DMP in benzene, a relative yield of 64.3 (tertiary) : 33.2 (primary) : 2.6 (secondary). If one compares the relative reactivity per hydrogen, in 3-methylpentane this value was 3.9, in neat DMP this increases to 7.5, and for DMP in benzene, 24.7. Dokolas calculated a relative reactivity of 16.9 (tertiary) : 2.3 (secondary) : 1 (primary) for DMP in neat solution.<sup>19</sup> The researchers also found that in DMP, almost no abstraction occurs at the secondary position and radical formation predominates at the primary and tertiary locations. The authors attribute this affect to *t*-butoxyl solvation, increasing the steric bulk of the abstracting radical. For 3-methylpentane there is “an absence of steric hindrance associated with a 2,4-dimethyl arrangement...” creating a larger effect on regioselectivity in DMP.

Camara et al. also conducted an extensive EPR study on PP model compounds, examining DMP, 3-methylpentane and 2,4,6-trimethylheptane.<sup>13</sup> They found in both DMP and 2,4,6-trimethylheptane that abstraction occurred at the primary and tertiary positions, with tertiary abstraction predominating over primary. They were unable to quantify abstraction from the secondary positions of these compounds. By contrast, 3-methylpentane showed abstraction from the secondary position in amounts greater than primary. This led Camara and coworkers to the conclusion that bulkiness and the sterics of the carbon center next to the abstraction position plays a large role in the reactivity of a site.

In 1962, Beckwith<sup>23</sup> studied H-atom abstraction regioselectivity from a similar compound, 2,2,4-trimethylpentane, using the thermal decomposition of di-*t*-butyl peroxide and anthracene as a radical trap. Beckwith was able to isolate several products and from them concluded that *t*-butoxyl radicals abstract mainly from the primary positions and was unable to

isolate any abstraction from the secondary or tertiary positions. He explained this phenomenon through steric effects, noting that the primary positions were the least hindered sites on the molecule.

In studying the H-atom abstraction by *t*-butoxyl radicals using laser flash photolysis, Finn<sup>24</sup> found in tertiary amines that the rate of H-atom abstraction did not necessarily follow the C-H bond strength. In fact, what they found was that at ambient temperatures, most hydrogen abstractions by *t*-butoxyl radicals in solution are entropy controlled. This means that the regioselectivity of H-atom transfers with *t*-butoxyl radicals is dictated and controlled by orientation and accessibility rather than the strength of the C-H bonds.

While it is clear from these results that steric effects are playing a role in these reactions, the extent of these steric and enthalpic effects have not yet been fully explained. Herein, along with carrying out an extensive model compound study that focuses on the regioselectivity phenomenon at the secondary position, these H-atom abstraction methods will also be investigated using quantum chemical calculations. Probing these reactions *in silico* provides an attractive means to separate the enthalpic and steric effects in these reactions. Looking at the trends in the thermodynamic parameters for abstraction from the different possible positions in each model compound, and the corresponding positions (primary, secondary, tertiary) in the other model compounds, one can isolate the cause of, and explain, the decreased selectivity at the secondary positions found in DMP.

#### **1.4 Quantum mechanical calculations**

Computational methods provide an appealing route to determining the thermodynamic parameters that govern the selectivity of these chemical reactions. Enthalpic and steric effects that play a role in the regioselectivity and reactivity of polymer grafting reactions are not yet understood. Two general theories of electronic structure determination exist, *ab initio* calculations

and Density-Functional Theory (DFT). *Ab initio* calculations model the molecule from first principles, approximating the electronic wavefunction first, and then determining the electron density, thermodynamic properties and vibrational modes. DFT methods work in a similar way, but first determine the electron density of the molecule. From this DFT then calculates the electronic wavefunction and subsequent properties.<sup>25</sup>

Both methods have their advantages and disadvantages. High level *ab initio* calculations are the most accurate calculations of an atomic system possible, but scale poorly to large molecular sizes. DFT calculations provide an attractive alternative, they scale better with molecular size than *ab initio* calculations, and the accuracy of the results challenge those of the *ab initio* calculations at the lower, and more practical, level of theory.<sup>25</sup> Because of this, over the past forty years or so, DFT has become increasingly more popular and is currently the calculation method of choice over the lowest level *ab initio* calculation method, Hartree Fock (HF).<sup>26</sup> The fundamental differences that make these methods so different will be discussed in detail later.

Many computational packages exist which take advantage of these methods to model molecules and estimate parameters (eg. Gaussian, NWChem, GAMESS). Here, all calculations will be carried out employing the Gaussian suite of programs. Quantum mechanical calculations carried out through these programs can be used to estimate or predict molecular geometries, dynamics, IR/Raman spectra, UV/Vis spectra and much more. The literature provides a wide range of areas and situations where computational methods have been used. Understanding the methods helps to properly assess the literature for quality and accuracy.

#### **1.4.1 Computational methods**

Several different modeling techniques exist to estimate the energy of a system. Continuum models ignore the molecular structure and focus on the bigger picture. They are well suited for exploring the bulk properties of materials, using techniques such as finite difference

methods. Force-field models treat the atoms or molecules as individual particles and do not include the electrons and their effects in the calculations. The interactions between the particles are parameterized to experiment or high level calculations (an example of this would be using a Morse or Leonard-Jones potential to model a chemical bond). Force field methods are more computationally efficient than quantum chemical methods, but are not suitable for modeling reactions.

Unlike these methods, quantum chemical calculations treat the electrons explicitly using quantum mechanics. One approximation employed by all quantum chemical methods which allows the estimation of the solution to the time independent Schrödinger equation, and in turn of molecular energies and thermodynamic parameters, is the Born-Oppenheimer approximation.<sup>27</sup> The Born-Oppenheimer Approximation is developed from the relative mass of protons and electrons. The mass of a single proton is about two thousand times the mass of an electron. That alone is a big difference, and when considering that nuclei are usually composed of many protons and neutrons the difference in mass between the nuclei of a molecule and its electrons becomes extremely large. Because of this difference, nuclei move and vibrate much slower than the motion of the electrons around them. At the time scale of the movement of an electron, the nuclei appear to be stationary. Applying this assumption to the full Hamiltonian eliminates the term corresponding to the kinetic energy of the nucleus and models the electrons as though they are moving in a field of fixed nuclei. By solving the Hamiltonian, molecular properties and reactions can be modeled directly by the electronic wavefunction of the molecule. The cost approximating the solution of the time independent Schrödinger equation and in turn the high accuracy is paid for by the computationally intensive nature of the calculations. Because of this, many different quantum chemical calculation methods exist for a researcher to select from for a wide range of accuracy and computational cost.

*Ab initio* methods, such as HF solve the quantum mechanical calculations using only mathematical approximations and focus directly on the wavefunction of the molecule. HF is the simplest *ab initio* method, and has several problems associated with it. The first problem originates from the average electron field that used to model the coulomb repulsion between the electrons which leads to errors in the energy estimation. The second issue arises from the method HF uses to satisfy the Pauli Exclusion Principle, which states that two electrons with the same spin cannot occupy the same orbital. The method which HF uses to account for this (the Slater determinant) causes opposite spin electrons to be treated independently of one another to ensure the Pauli Exclusion Principle is upheld, while electrons of the same spin are correlated. This causes instantaneous repulsion interactions between electrons to be ignored and as a result two electrons of the opposite spin can occupy the same point in space. Another fault in HF is called static correlation which is caused by HF only being able to consider one electron configuration at a time. When two or more electron configurations are close in energy the electrons can spread out into these configurations to lower total energy and HF does not account for this. Because of these problems, HF can never determine the true energy of the molecule. The difference between the energy estimation at the limit of the HF method, and the true energy caused by these issues is called electron correlation.

All other *ab initio* methods work to improve upon the HF energy and are conveniently termed as post-HF methods or electron correlation methods. The first area which exists to improve upon HF are multideterminant methods where electrons are promoted to higher energy unoccupied orbitals (by using multiple Slater determinants) and these energies are weighted. The result of this is creating more space for the electrons to occupy and lowering electron repulsion. This includes, at the extreme, the full Configuration Interaction (Full CI) method which includes all the possible excitations from HF and solves the Schrödinger equation exactly at an infinitely large basis set, producing the exact energy of the molecule and exact reaction energies within the

limits of the Born-Oppenheimer approximation. Multideterminant methods also include the slightly more practical CCSD(T) method which examines only excitations at the singlet and doublet level, with some triplet excitations considered. CCSD(T) calculations are currently considered the gold standard in computational calculations.

The other area which improves upon HF is called perturbation theory which expresses corrections to the energy, Hamiltonian, and wavefunction as perturbations. In Moller-Plesset (MP) perturbation theory the perturbation is the difference between the ways electrons see each other in HF, and how they see each other in reality. MP methods correct the energy by examining excited states of the system based off the reference energy from HF. The number denotes the extent of the perturbation after the MP prefix, such as MP2 or MP4. In theory, one can perturb an infinite amount, but in practice only up to fourth order corrections are used. MP2 generally accounts for about 90% of the correlation energy.

All the *ab initio* methods which work to improve HF come with a wide range of range of accuracies and computational costs. One of the greatest limitations in any molecular modeling is the time required to complete the calculation. The biggest factors that determine the length of a calculation (besides the method used) is the size of the molecule and the size of the basis set used to describe the system. Generally, the size of the system cannot be manipulated. The system of interest is defined before one sets out to run any quantum chemical calculations. However, there are a few methods that can help lower the computational time and not affect the accuracy of the calculation to a large extent. One technique is to truncate alkyl groups or benzyl groups that do not participate directly in the reaction center. As long as these groups do not have conjugative effects or a steric presence on the reactive site, truncating these to a methyl group generally does not harm the accuracy of the calculations.

The second factor is the basis set size in the calculation. Within a basis set are basis functions. These functions are analogous to atomic orbitals and define where in the molecule the



electrons can be found. Basis functions can take any form but they should provide a good description of the electron density. The two most common basis functions are Slater functions and Gaussian functions shown in Equation 1-1 and Equation 1-2.

$$\phi_s(\theta, \phi, r) = Y_m^l(\theta, \phi) \left( \frac{\alpha^3}{\pi} \right) e^{-\alpha|r-R_a|}$$

**Equation 1-1:** Slater type basis function

$$\phi_g(\theta, \phi, r) = Y_m^l(\theta, \phi) \left( \frac{2\alpha}{\pi} \right)^{3/4} e^{-\alpha|r-R_a|^2}$$

**Equation 1-2:** Gaussian type basis function

The first part of each of these functions,  $Y_m^l(\theta, \phi)$ , represents the spherical harmonic portion of the basis function which is unique for each orbital (s, p<sub>x</sub>, p<sub>y</sub>, d<sub>xy</sub>, ect.). For example, in an s orbital, the spherical harmonic function is equal to one. The second half of these functions is what makes them unique. In each case,  $\alpha$  is a parameter that controls the decay of the function,  $r$  is the position and  $R_a$  is the position of the nucleus that the function is centered on. Therefore,  $|r - R_a|$  represents the distance from the nucleus. Ideally, the wavefunction should peak at a cusp at the nucleus, and tail away further from the nucleus.

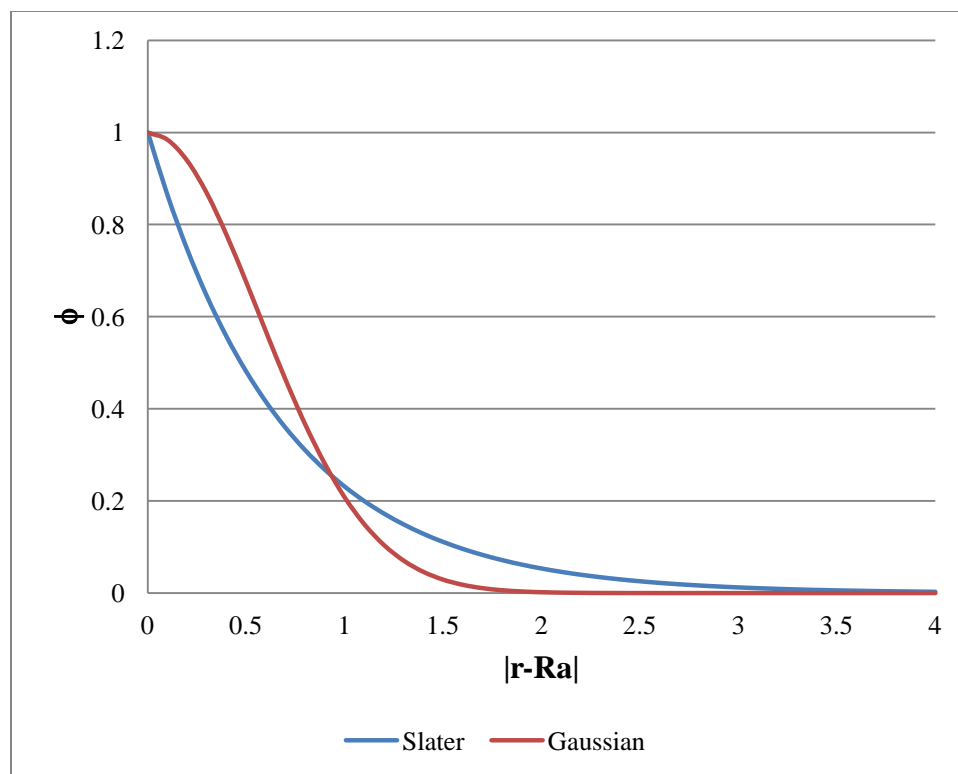


**Figure 1-1:** Slater and Gaussian type functions as a function of nuclear distance for an s orbital.

Figure 1-1 illustrates the behaviours of these two functions. It can be seen that the Slater function describes the desired behavior quite well and produces a cusp at the nucleus and trails off as further from the nucleus. The Gaussian function does not reproduce this trend very well. The cusp is not recreated and the function falls off too quickly. Even though this is the case, Gaussian functions are more popular because the integral can be computed analytically, whereas the solution to the Slater function must be solved in a more time consuming numerical manner.

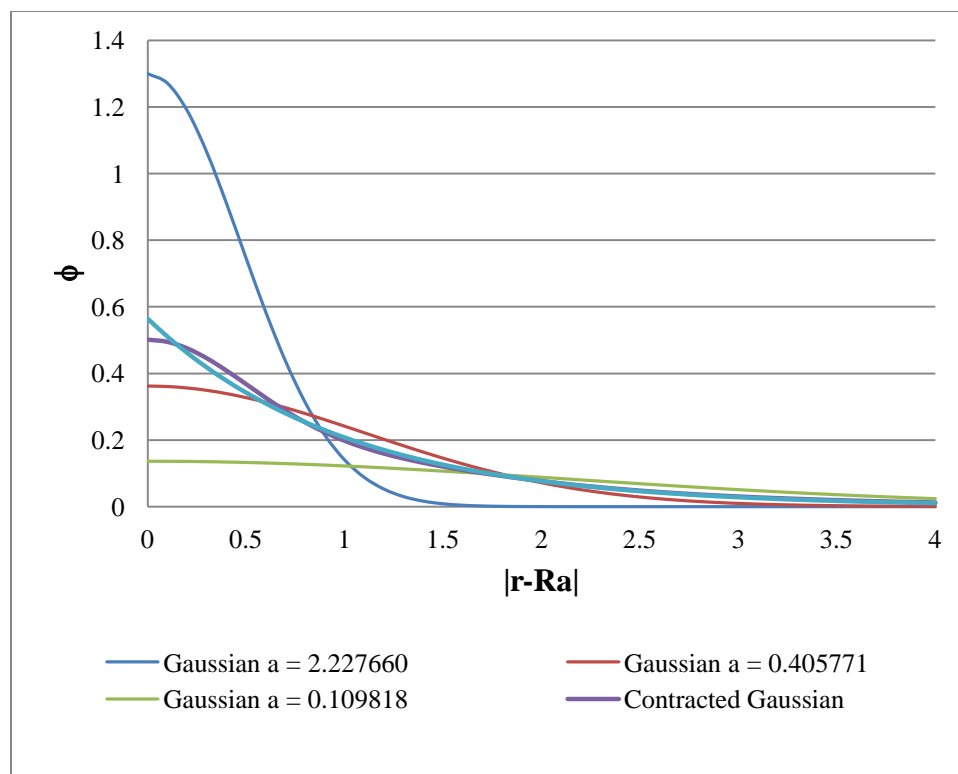


**Figure 1-2:** Three different primitive Gaussian type functions contracted to estimate a Slater type orbital.

To overcome the inaccuracies of the Gaussian functions, they can be linearly combined to estimate the original Slater function. Figure 1-2 demonstrates this by combining three Gaussian functions in an attempt to form a Slater orbital. The contracted Gaussian is the sum of the primitive Gaussians used to create it. The contracted Gaussian approximates the Slater function better than any of the primitives on their own and does a well at modeling the orbital at large distances from the nucleus, but still does not describe the cusp one should expect at the center of the orbital. In fact, a contracted Gaussian will never describe the cusp correctly no matter how many primitive Gaussians are used to form the contracted. The coefficients used to combine the primitive Gaussians and those used to describe the primitive Gaussians themselves (the  $\alpha$  values) are defined within the basis set selection and are not altered during the optimization process.

In order to make computations easier and to make it so one does not have to choose each orbital type or the number Gaussians for each atom, Slater and Gaussian type orbitals are grouped together into basis sets. Within the basis set is defined the contracted Gaussians and the number of Gaussians or Slater type orbitals per atom. The linear combination of basis functions defines where the electrons can be and different basis sets can be chosen which have a larger number of, or differently shaped, basis functions.

Since basis functions attempt to reproduce the atomic orbitals in the molecule, the more atoms present in the system, the more basis functions that are required. This is why molecular size is one of the limitations in these calculations, the greater the number of basis functions the more parameters that have to be optimized and the longer the calculations take. Along with truncation, one can also decrease the size of the basis set used, to limit the number of basis functions present. Many calculations then become a balance between basis set size, molecular size and level of theory used to reach an acceptable calculation run time.

Different levels of theory scale differently with the number of basis functions ( $N$ ) used, dependent on how they deal with the electrons in the molecule. HF scales at  $N^4$ , and Full-CI scales at  $N!$ . Because of this, Full-CI methods are well beyond the reach of all but the simplest molecules. These methods are also not limited only to ground state energies and can be applied to excited state calculations.

Semi-empirical methods, such as Austin-Model 1 (AM1) or Parameterized-Model 3 (PM3), apply approximations to HF that are derived from experimental data to lower the computational cost of the calculation. Many of the integrals that describe electron interactions are ignored or set to fit experimental data. These methods scale very well ( $N^2$ ) but are only as accurate as the approximations and parameters used. Molecules or bonds that are similar to the experimental data set will be modeled quite well, but dissimilar bonds will not be modeled accurately. Like *ab initio* methods, they can be applied to ground states and excited states.

The last group is those methods derived from DFT and do not rely on HF. DFT methods can be designed like *ab initio* methods where the quantum mechanical equations are solved using only mathematical approximations, or they can operate by using some experimental data and in some cases completely empirical relations in the calculations. In implementation, the mode of optimization is identical to that of Hartree Fock, but instead of using the wavefunction to calculate the energy, the density is used. The principle relies on the Hohenberg-Kohn theorems. The first theorem states that two unique densities are described by two unique wavefunctions and that no two densities can be made by the same wavefunction or vice-versa. The second theorem states that minimizing the energy of the density obeys the variational principle, which states that that for any trial wavefunction or initial guess at the wavefunction the energy of the wavefunction must be greater than or equal to the true ground state energy of the wavefunction defined by the functional used. In all variational methods, by minimizing the energy we can never overshoot the true energy of the compound, or in the case of DFT, the true energy of the functional used. The variational principle was not discussed above, but HF and some other methods agree with this principle.

DFT therefore uses the electronic density to calculate the energy of the system. This is in contrast to *ab initio* methods where the electronic wavefunction is determined, and from this the density and energy calculated. By manipulating the electron density instead of electrons, the number of dimensions is lowered, (3 spatial dimensions down from 3 coordinates for each electron, plus 1 for spin) but other problems caused by the implementation of this method arise. Corrections to these issues are included within unique functionals. In the case of DFT, these functionals take in the density and return the energy of the system. Many different functionals exist. Some functions are created from first principles, using no experimental data and purely theory to develop the functional. Some functionals are empirical and rely on experimentally derived coefficients and there also exist those in between, which rely on theory, as well as

empirical data. The most commonly used functional is the B3LYP functional, which is a hybrid functional that uses theory and empirical values.

As well as these advantages, by manipulating the electron density directly electron correlation is inherently accounted for. DFT methods are among the most computationally efficient methods, generally scaling by a factor of  $N^3$  (some DFT methods scale, in principle, linearly), and provide results which are much more accurate than HF, and usually more accurate than MP2, but at a lower cost. Because of this, DFT has become very popular and surpassed the use of HF and MP2.<sup>26</sup> DFT, along with increases in computer power and availability, has provided researchers an easy way to undertake computational modeling on large molecules and obtain accurate results.

Herein we utilize a composite method called CBS-QB3. The CBS-QB3 method involves a geometry calculation using DFT and the B3LYP functional, followed by a singlepoint energy calculation at the CCSD(T) level and basis set extrapolation using MP2. The CBS-QB3 method has been found to reproduce BDEs within an error of 1 kcal/mol.<sup>28</sup>

#### **1.4.2 Assessing the methods**

Over the years, trends in the different methods have emerged in the literature. When determining transition state structures for H-atom abstraction reactions, DFT has a difficult time optimizing due to the low reaction barriers. The computed barriers to activation using DFT can often be too low and sometimes negative in the case of small molecule radicals. However, HF and second order Møller Plesset Perturbation theory (MP2) considerably overestimate these barriers in small molecule radicals.<sup>29</sup>

More confusing results appear when examining accuracy by changing the basis set. In theory, the larger the basis set, the closer to the theoretical limit of the method one approaches. With more variables to modify, forming the closest approximation to the electronic wavefunction

should be possible. At the extremes, with an infinitely large basis set, this is indeed true,<sup>25</sup> but at the basis set sizes used in practical calculations a larger set does not always lead to a more accurate result.<sup>29,30</sup> Different basis sets may provide better more accurate results for different values of interest.<sup>31</sup>

Many articles exist where a molecular system, or set of structures, is used to try and determine the best method and basis set combination to use for estimating experimental results. Results vary depending on the molecular set of interest and these experiments only provide a best method for the molecules studied, or at best similar molecules. Only if a study of this type has been done on the system of interest does one have a stepping stone from which to proceed.

When there is no previous study on which to base methodology, choice of theoretical method and basis set becomes seemingly arbitrary. Basis set choice falls under the theory that larger is better, but a balance must be reached with the computational resources available. Method selection is generally more concrete at the higher levels of theory, but the computational resources required for these studies are large, and limits the scope, or the size of the molecules studied. However, like basis sets, methodology in the mid-range of theory is more subjective. Studies on a molecular set also become more complicated when basis sets and methodology are varied and the results compared. No single method is the best for every situation. The main limitation will always be the computational resources available. The weaknesses and strengths of each method must be understood before a particular methodology is chosen.

### **1.5 Thermochemistry in quantum chemical calculations**

Thermochemistry information in Gaussian is determined through frequency calculations, specified through the 'Freq' keyword. Frequency calculations are used to determine vibrational, rotational and translational modes of the nuclei in the molecule and only provide relevant information on ground state or transition state structures. After a successful completion of the

optimization sequence and electronic wavefunction of the ground or excited state is determined, the frequency calculation takes the electronic wavefunction and uses it as the potential in which the nuclei vibrate to determine the nuclear wavefunction, which describes the motion of the nuclei. With this, the derivatives and second derivatives of the energy with respect to nuclear positions can be determined.

In geometry optimizations, Gaussian optimizes for structures where the first derivative of the energy is zero with respect to nuclear position. If successful, this will locate so-called stationary points on the potential energy surface. These stationary points will be in a potential energy well or a transition state on a saddle point on the potential energy surface. In a frequency calculation, Gaussian calculates the second derivatives of energy with respect to nuclear positions. If all second derivatives are positive the molecule is at the bottom a potential energy well. If only one derivative is negative the stationary point is a first order transition state, a minimum in all directions except for the reaction pathway where it is a maximum. More than one negative second derivative is possible, but these correspond to higher order transition states which generally will not be the lowest energy reaction pathway.

The values of the second derivatives of energy with respect to the nuclear positions also provide the force constants for bond vibrations. The frequency of these vibrations is approximated using the theory of simple harmonic motion. If the second derivatives are positive in all directions on the potential energy surface, all the normal modes are positive. However, when there is a negative second derivative an imaginary frequency is obtained from the negative force constant, often referred to as a negative frequency. By checking the frequency output for a negative frequency it can be determined what type of stationary point the molecule is located at on the potential energy surface.

Once the stationary points are characterized, the next step is to determine the thermodynamic contributions to enthalpy, entropy and the Gibbs free energy. A great reference



for this is by J. W. Ochterski<sup>32</sup> where the procedure for using the partition functions that Gaussian employs to calculate thermodynamic parameters is described. Conceptually, a partition function is a representative equation of all the thermodynamic states in equilibrium for a given set of molecules. Different partition functions (ensembles) can be derived which restrict different parameters within the function. These parameters include, but are not limited to: temperature, volume, the number of particles or the chemical potential of the system. Using these partition functions and their derivatives, the thermodynamic parameters for stationary points on the potential energy surface can be determined.

With thermodynamic parameters in hand, one can now begin to estimate heats of reaction, BDEs, activation energies, rate constants and much more. For the current research, the focus is on steric and enthalpic affects that can be analyzed directly from the raw thermochemical data, but also on reaction barriers and rate constants for abstraction from different positions within a molecule. Using the calculated rate constants and activation parameters a more detailed analysis and investigation of the reaction pathway can be pursued.

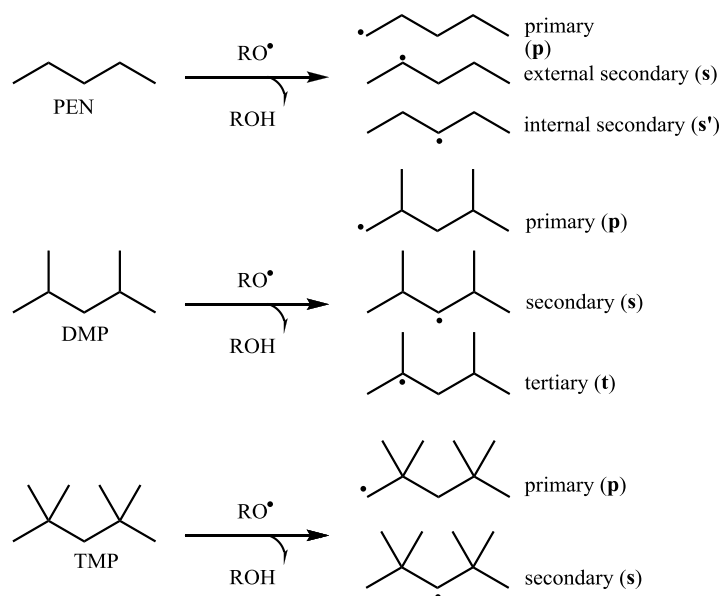
## **1.6 Quantum chemical calculations for H-atom abstractions**

To probe the regioselectivity of H-atom transfer in polyolefins, model compounds will be used to simulate the chemical environments present in the polymers that the initiators encounter during H-atom abstraction. Computationally, model compounds also allow us to undertake higher level calculations and achieve a better description of the electronic structure due to the decrease in the size of the system. The smaller the molecule the lower the number of electrons present and the fewer degrees of freedom that need to be optimized. Computations generally scale exponentially with the number of electrons, and as a result, using smaller molecules limits prohibitively long calculations.

H-atom abstractions have been widely studied using computational methods. Basch<sup>33</sup> carried out an extensive comparison of different H-atom abstractions on a range of molecules from methane to ammonia where he compared Becke's B3LYP DFT method to Moller-Plesset (MP2) and the CCSD(T) levels of theory. They found that the B3LYP method compares well to MP2 and generally underestimates reaction energies.

Specifically related to polyolefin graft copolymerization, in 2007, Marque and Siri<sup>34</sup> carried out a DFT study using the B3LYP functional and a large basis set to estimate the reactivity of 2,4,6-trimethylheptane towards hydrogen abstraction by *t*-butoxyl radicals. They focused their modeling attempts towards reproducing EPR data by Niki et al<sup>14</sup> using DFT methods that had not been used previously to study these types of systems. Up to this point, the majority of H-atom abstractions with *t*-butoxyl were modeled using *ab initio* methods due limitations imposed by the availability of computational power required to run correlation corrected methods.<sup>35,36</sup> As well as DFT, they also used a solvent surface approach to assess the accessibility of different hydrogen locations on the molecule as well as mathematical modeling using Predici to model the decay of produced radicals to simulate the EPR data.

Their results were inconclusive. They examined the reaction in a variety of different ways and were not able to reproduce the experimental results until they modeled the system using Predici. However, some of the rate constants were chosen almost arbitrarily with no other analysis or verification for them. However, they do state that these constants "...must be used with high caution". They noted that modeling the system correctly requires accurate modeling of the enthalpic as well as steric contributions to the reaction. However, their study was not carried out at a very high level of theory, and some errors may have been present in their stationary point analysis. Because of this there is still more work that can be done on this system using quantum mechanical calculations to try and delineate the thermodynamics of H-atom abstractions in these systems.



**Scheme 1-6:** Carbon-centered radicals produced through reaction with alkoxy radicals. p, s and t denote primary, secondary and tertiary radicals, respectively.

In Scheme 1-6 is shown the possible H-atom abstraction products from the three model compounds examined in this study. Since the main goal is to determine the thermodynamic parameters and delineate entropic and enthalpic effects on the rate of H-atom abstraction, two radical initiators will be examined to help expose the entropic effects: *t*-butoxyl and methoxyl. *t*-Butoxyl radicals will be used in the radical trapping experiments and will provide a means of direct comparison to the computational data. Methoxyl radicals, being the simplest possible alkoxy radical, allow us to investigate the use of a less bulky initiator to compare with *t*-butoxyl. Since methanol and *t*-butanol have essentially the same O-H BDEs, the enthalpic component of their reactions with the model compounds should be highly similar, making any differences in their regioselectivity clearly attributable to steric interactions.

## Chapter 2

# Investigating the Regioselectivity of H-atom Transfer in Polymer Model Compounds Using the Radical Trapping Technique

### 2.1 Introduction

Investigated herein is the origin behind the differences in reactivity, and as a result the difference in graft copolymerization yields, of various polymers – specifically polyethylene, polypropylene and polyisobutylene. Direct investigation on the polymers themselves is troublesome, and while some studies have been carried out,<sup>14</sup> here the model compounds shown in Scheme 1-3 have been used to simplify the analysis. Using suitable model compounds avoids the high temperatures required to reach the polymer melt state, and the smaller molecule size allows direct comparison to quantum chemical calculations.<sup>34</sup>

Several studies on H-atom abstraction regioselectivity have already been carried out in this area using model compounds. Camara<sup>13</sup> carried out an EPR study on a wide variety of small chain alkanes and found that the majority of H-atom abstractions occur at the tertiary position in DMP but not at the secondary position. Niki<sup>14</sup> also obtained a similar result again using EPR and found selective abstraction from the tertiary position.

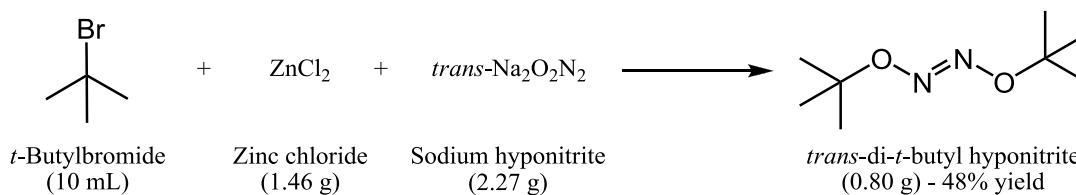
One issue with EPR in these systems is overlap in the spectra of the tertiary and secondary radicals making it difficult to obtain accurate measurements.<sup>14</sup> To improve upon these results, Dokolas,<sup>19</sup> using the nitroxyl radical trapping technique developed by Rizzardo and Solomon,<sup>21</sup> determined the regioselectivity of reactions of *t*-butoxyl radicals with DMP. They found increased sensitivity in their measurements, being able to identify small amounts of products derived from abstraction from the secondary position.

It has been proposed that steric interactions and entropic barriers are the cause of the unusual lack of abstraction at the secondary position in DMP.<sup>15,21</sup> To expand upon these results and further explore the environment proximal the secondary position, herein is reported the regioselectivity of H-atom abstraction by *t*-butoxyl radicals in a molecular data set that begins at PEN, with unhindered secondary positions, progressing to TMP which has two *t*-butyl groups eclipsing each side of the secondary reaction site.

Insight is gained from alkyl radical trapping techniques previously found to be effective in this system.<sup>19</sup> In these experiments the model compounds are exposed to *t*-butoxyl radicals and the generated alkoxy radicals are trapped. The regioisomers formed from the initial H-atom abstractions are then separated and their relative abundances quantified. In this case, the thermal decomposition of di-*tert*-butyl hyponitrite (DTBH) was used as the oxy radical precursor. DTBH decomposes readily at bench top temperatures and its kinetics have been previously studied.<sup>37</sup> Similar to the commonly used radical trap (2,2,6,6-Tetramethylpiperidin-1-yl)oxyl (TEMPO), the radical trap 1,1,3,3-Tetramethylisindolin-2-yloxy (TMIO) reacts at the diffusion controlled limit with carbon centered radicals but also contains a chromophore which can be used as a tag during separation by HPLC.<sup>38</sup>

## 2.2 Results

### 2.2.1 Synthesis of di-*t*-butyl hyponitrite (DTBH)



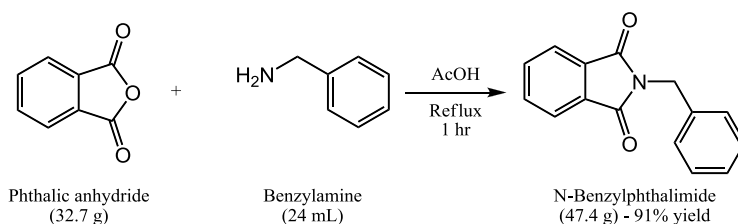
**Scheme 2-1:** Synthetic route for di-*t*-butyl hyponitrite.

10 mL of diethyl ether was placed in a 25 mL round bottom flask, followed by the addition of *t*-butylbromide (10 mL, 89 mmol) and zinc chloride (1.46 g, 11 mmol). To this,

sodium hyponitrite (2.27 g, 21 mmol) was added slowly with stirring over the course of 20 minutes. It was then left to stir for 100 minutes, filtered and washed twice with water. The yellow crystals were recrystallized from methanol to yield the product as 0.80 g (5.1 mmol, 48% yield) of white needle-like crystals. <sup>1</sup>H NMR analysis obtained one singlet at 1.4 ppm.

## 2.2.2 Complete synthesis of 1,1,3,3-tetramethylisindolin-2-oxyl (TMIO)

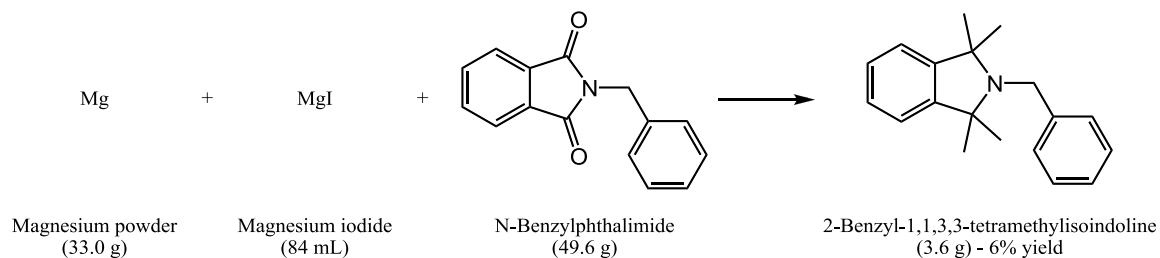
### 2.2.2.1 Synthesis of N-benzylphthalimide



**Scheme 2-2:** Synthetic route for N-benzylphthalimide.

250 mL of acetic acid and phthalic anhydride (32.7 g, 221 mmol) were heated in a 500 mL round bottom flask to 90 °C, followed by the addition of benzylamine (24 mL, 220 mmol). The mixture was heated to reflux for 1 hour then cooled to room temperature, followed by an ice bath. The reaction was then quenched with water to precipitate out the product. The product was filtered and washed with cold water and recrystallized from ethanol to yield 47.4 g of the product (200 mmol, 91% yield) as white needle-like crystals.

### 2.2.2.2 Synthesis of 2-benzyl-1,1,3,3-tetramethylisindoline

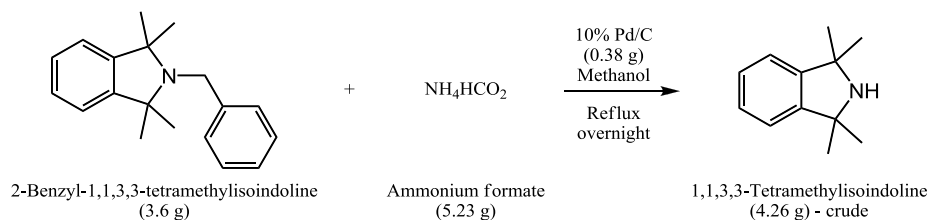


**Scheme 2-3:** Synthetic route for 2-benzyl-1,1,3,3-tetramethylisindoline.

Diethyl ether was dried over sodium over night and ~700 mL were distilled into a 1000 mL three neck round bottom flask which contained magnesium powder (33.0 g, 1.36 mol). To this, two iodine crystals were added. Magnesium iodide (84 mL, 1.35 mol) was placed into a dropping funnel and ~10 mL were added to the ether and left until boiling began. The remainder of the magnesium iodide was then added dropwise over the course of 3.5 hours while removing ether until the internal temperature reached 80 °C.

N-Benzylphthalimide (49.6 g, 210 mmol) was dissolved with slight heating in ~600 mL of freshly distilled toluene which was dried over calcium hydride. This was then added to the Grignard via a cannula with stirring, keeping the internal temperature at 60 °C. The reaction was left at 60 °C overnight, then slowly distilled to ~400 mL. This was diluted with petroleum ether and hot filtered through Celite, concentrated, and passed through a short column of basic alumina until the eluent was amine free. The liquor was then concentrated and placed in the freezer overnight to yield 3.56 g of product (13.4 mmol, 6% yield), a white powder.

### 2.2.2.3 Synthesis of 1,1,3,3-tetramethylisindoline

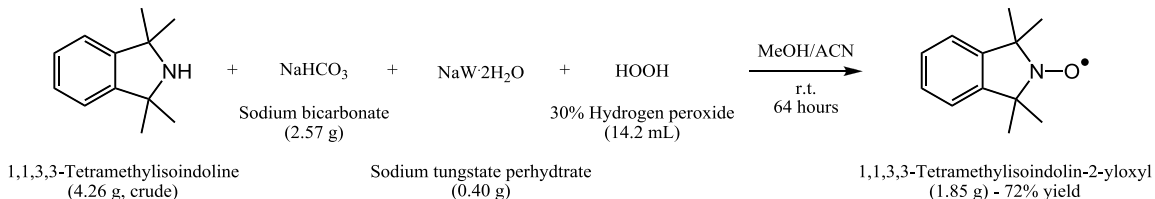


**Scheme 2-4:** Synthetic route for 1,1,3,3-tetramethylisindoline.

10% Pd/C (0.38 g) was placed in a 100 mL round bottom flask, evacuated, and filled with argon. 2-Benzyl-1,1,3,3-tetramethylisindoline (3.56 g, 13.4 mmol) was dissolved in 45 mL of methanol and added carefully with a syringe to the flask. Ammonium formate (5.23 g, 82.9 mmol) was then added. The mixture was heated to reflux and left overnight. GC-MS analysis the

next morning revealed that no 2-Benzyl-1,1,3,3-tetramethylisoindoline remained. The mixture was filtered through Celite and concentrated to yield 4.261 g of crude material.

#### 2.2.2.4 Synthesis of 1,1,3,3-tetramethylisoindolin-2-yloxy



**Scheme 2-5:** Synthetic route for 1,1,3,3-tetramethylisoindolin-2-yloxy.

35 mL of methanol and 2.5 mL of acetonitrile were added to 1,1,3,3-tetramethylisoindoline (4.26 g, crude from previous step). To this was added sodium bicarbonate (1.26 g, 15.0 mmol), sodium tungstate perhydrate (0.18 g, 0.55 mmol) and 30% hydrogen peroxide (7 mL, 62 mmol). After 44 hours, GC-MS showed residual starting material so an additional 1.31 g of sodium bicarbonate, 0.22 g of sodium tungstate perhydrate and 7.2 mL of 30% hydrogen peroxide were added. After another 20 hours, GC-MS showed little remaining starting material. The mixture was diluted with water which caused a precipitate to crash out. This was washed twice with 75 mL of petroleum ether. The petroleum ether was washed twice with 50 mL of 1 molar sulfuric acid, and once with 50 mL of brine. The organic layer was dried over magnesium sulfate and evaporated to yield 2.5 g of crude product. This was recrystallized from petroleum ether to yield 1.85 g of product (9.7 mmol, 72% yield) as yellow crystals.

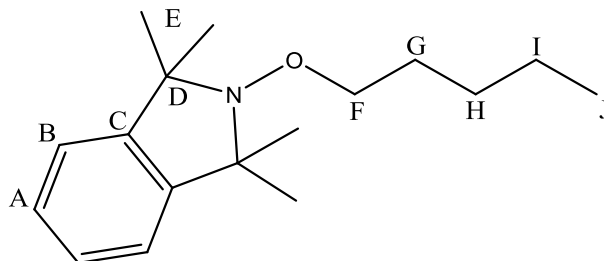
#### 2.2.3 Characterization of model compound derivatives

A full in-depth characterization of the model compounds can be found in Appendix B. Presented here is the pertinent characterization data.



## Pentane derivatives

### *1,1,3,3-Tetramethyl-2-(pentyloxy)isoindoline (PEN-p)*

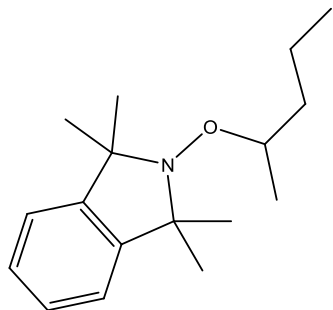


**Scheme 2-6:** Carbon and hydrogen labeling scheme for NMR characterization of the primary trapped radical product of pentane (DMP-p)

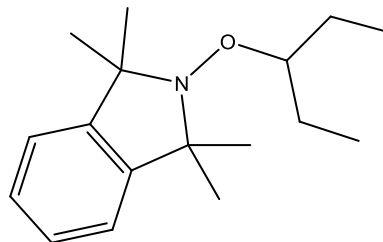
**Table 2-1:** Carbon and hydrogen NMR peak assignments for PEN-p

Position	<sup>13</sup> C Chemical Shift (ppm)	<sup>1</sup> H Chemical Shift (ppm)	Multiplicity	J (Hz)	H Integration
A	121.44	7.09	dd	5.5,3.2	2
B	127.08	7.22	dd	5.5, 3.2	2
C	-	-	-	-	-
D	-	-	-	-	-
E	29.05, 28.68	1.42	br s	-	12
F	99.97	3.91	t	6.6	2
G	34.65	1.64	m	-	2
H	25.27	1.26	m	-	2
I	20.68	1.26	m	-	2
J	11.41	0.98-0.92	m	-	3

***1,1,3,3-Tetramethyl-2-(pentan-2-yloxy)isoindoline and 1,1,3,3-tetramethyl-2-(pentan-3-yloxy)isoindoline (PEN-s and PEN-s')***



**Scheme 2-7:** PEN-s carbon and hydrogen labeling system for NMR characterization.

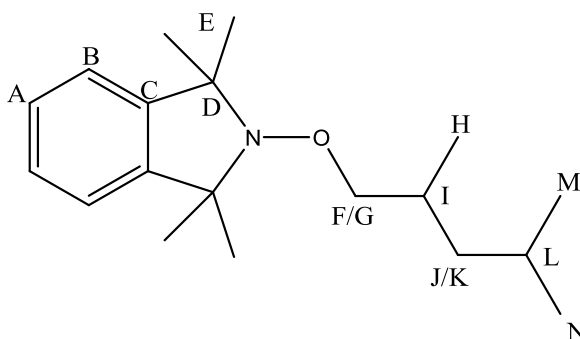


**Scheme 2-8:** PEN-s' carbon and hydrogen labeling system for NMR characterization

The two isomers form from trapping at the secondary positions of pentane, PEN-s and PEN-s' shown in Scheme B2 and Scheme B3, could not be isolated from one another by HPLC. The mixture was characterized partially by NMR to identify that the two compounds are present followed by the determination of their product ratio by NMR and GC-MS. The full analysis can be seen in Appendix B. It was found that two isomers appear in a ratio of 2.4:1 PEN-s: PEN-s'

**2,4-Dimethylpentane derivatives**

***2-(2,4-Dimethylpentyloxy)-1,1,3,3-tetramethylisoindoline (DMP-p)***

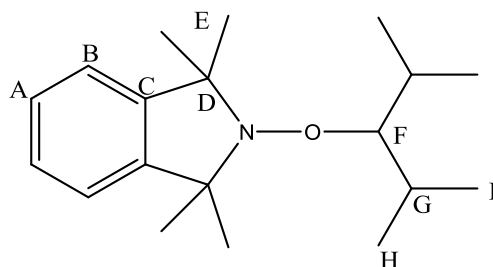


**Scheme 2-9:** Carbon and hydrogen labeling convention for NMR characterization of the primary trapped radical product of 2,4-dimethylpentane (DMP-p).

**Table 2-2:** Carbon and hydrogen NMR peak assignments for DMP-p.

Position	<sup>13</sup> C Chemical Shift (ppm)	<sup>1</sup> H Chemical Shift (ppm)	Multiplicity	J (Hz)	H Integration
A	121.42	7.09	dd	5.5,3.2	2
B	127.06	7.22	dd	5.5, 3.2	2
C	145.42	-	-	-	-
D	67.18	-	-	-	-
E	-	1.43	br s	-	12
F	83.08	3.81	dd	8.7, 5.1	1
G	83.08	3.69	dd	8.7, 6.9	1
H	17.94	1.01	dd	6.7	3
I	31.03	1.88	m	-	1
J/K	43.31	1.05-1.33	m	-	2
L	25.31	1.71	m	-	1
M	23.34	0.92	d	6.6	3
N	22.36	0.89	d	6.6	3

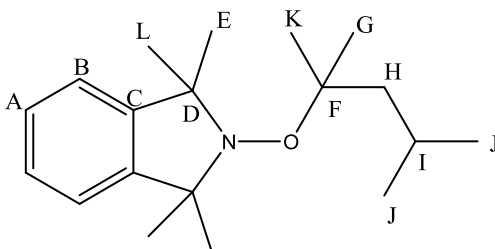
*2-(2,4-Dimethylpentan-3-yloxy)-1,1,3,3-tetramethylisoindoline (DMP-s)*



**Scheme 2-10:** Carbon and hydrogen labeling convention for NMR characterization of the secondary trapped radical product of 2,4-dimethylpentane (DMP-s).

**Table 2-3:** Carbon and hydrogen NMR peak assignments for DMP-s.

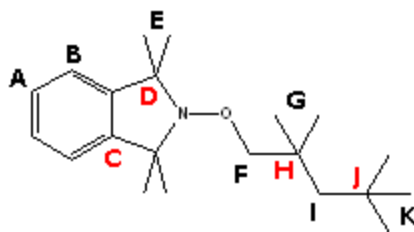
Position	<sup>13</sup> C Chemical Shift (ppm)	<sup>1</sup> H Chemical Shift (ppm)	Multiplicity	J (Hz)	H Integration
A	121.37	7.09	dd	5.5,3.2	2
B	127.04	7.22	dd	5.5, 3.2	2
C	139.69	-	-	-	-
D	67.18	-	-	-	-
E	30.24	1.51	br s	-	6
E'	25.62	1.4	br s	-	6
F	90.21	3.47	s	-	1
G	28.13	2.26	m	-	2
H	20	1.04	d	7	6
I	19.67	1	d	7	6

**2-(2,4-Dimethylpentan-2-yloxy)-1,1,3,3-tetramethylisoindoline (DMP-t)****Scheme 2-11:** Carbon and hydrogen labeling convention for NMR characterization of the tertiary trapped radical product of 2,4-dimethylpentane (DMP-t).**Table 2-4:** Carbon and hydrogen NMR peak assignments for DMP-t.

Position	<sup>13</sup> C Chemical Shift (ppm)	<sup>1</sup> H Chemical Shift (ppm)	Multiplicity	J (Hz)	H Integration
A	126.99	7.08	dd	5.6, 3.2	2
B	121.69	7.22	dd	5.6, 3.2	2
C	145.68	-	-	-	-
D	68.09	-	-	-	-
E	30.7	1.58	s	-	6
F	79.13	-	-	-	-
G	25.947	1.32	s	-	6
H	52.09	1.52	d	5.6	2
I	24.57	1.85	m	-	1
J	25.15	0.98	d	6.7	6
K	30.7	1.29	s	-	6
L	27.51	1.48	s	-	6

## 2,2,4,4-Tetramethylpentane derivatives

### 1,1,3,3-Tetramethyl-2-(2,2,4,4-Tetramethylpentan-3-yloxy)isoindoline (TMP-p)

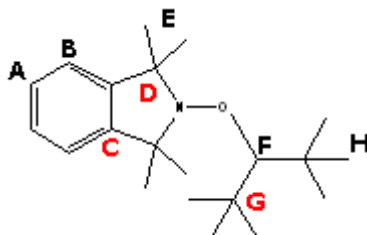


**Scheme 2-12:** Carbon and hydrogen labeling convention for NMR characterization of the primary trapped radical product of 2,4-dimethylpentane (DMP-t). Quaternary positions are denoted in red.

**Table 2-5:** Carbon and hydrogen NMR peak assignments for TMP-p.

Position	<sup>13</sup> C Chemical Shift (ppm)	<sup>1</sup> H Chemical Shift (ppm)	Multiplicity	J (Hz)	H Integration
A	127.22	7.1	dd	5.5, 3.2	2
B	121.54	7.23	dd	5.5, 3.2	2
C	145.65	-	-	-	-
D	67.51	-	-	-	-
E	-	1.45	br s	-	12
F	88.21	3.67	s	-	2
G	32.24	1.12	s	-	6
H	36.99	-	-	-	-
I	52.27	1.42	s	-	2
J	29.86	-	-	-	-
K	26.782	1.03	s	-	9

*1,1,3,3-Tetramethyl-2-(2,2,4,4-Tetramethylpentyl-2-yl)isoindoline (TMP-s)*



**Scheme 2-13:** Carbon and hydrogen labeling convention for NMR characterization of the primary trapped radical product of 2,4-dimethylpentane (DMP-t). Quaternary positions are denoted in red.

**Table 2-6:** Carbon and hydrogen NMR peak assignments for TMP-s.

Position	<sup>13</sup> C Chemical Shift (ppm)	<sup>1</sup> H Chemical Shift (ppm)	Multiplicity	J (Hz)	H Integration
A	127.21	7.22	dd	5.6, 3.2	2
B	121.24	7.07	dd	5.6, 3.2	2
C	146.07	-	-	-	-
D	69.48	-	-	-	-
E	-	1.64, 1.54	s	-	6, 6
F	93.04	3.71	s	-	1
G	38.83	-	-	-	-
H	31.54	1.22	s	-	18

**Retention times and High-Res MS analysis**

**Table 2-7:** High-Res MS results and retention times for the TMIO radical trapped model compound products

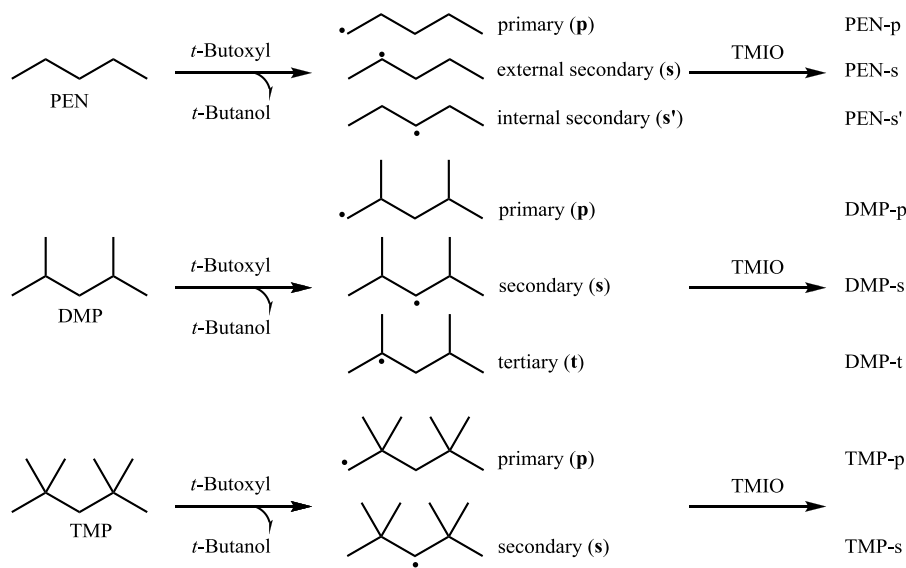
Compound	Calculated Mass	Mass Found	ppm	Retention time (min)
PEN-p	261.2093	261.2088	-1.8	20.7 <sup>a</sup>
PEN-s PEN-s'	261.2093	261.2087	-2.2	21.6 <sup>a</sup>
DMP-p	289.2406	289.2412	2.2	35.3 <sup>a</sup>
DMP-s	289.2406	289.2416	3.6	38.8 <sup>a</sup>
DMP-t	298.2406	289.2417	3.9	43.4 <sup>a</sup>
TMP-p	317.2719	317.2731	3.9	20.7 <sup>b</sup>
TMP-s	317.2719	317.2727	2.6	25.7 <sup>b</sup>

a) Using 85:15 MeOH:H<sub>2</sub>O at 4 mL/min

b) Using 90:10 MeOH:H<sub>2</sub>O at 4 mL/min

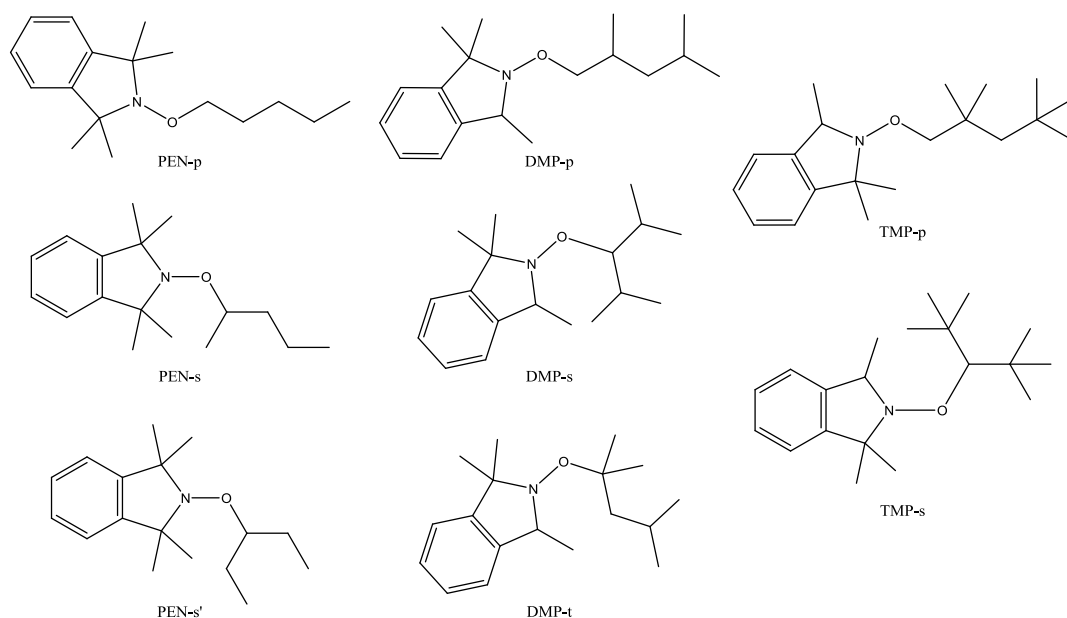
## 2.2.4 Alkoxyamine product distributions

To initiate the H-atom abstraction reactions, the thermal decomposition of DTBH was used to create a source of *t*-butoxyl radicals.<sup>37</sup> Abstraction of a H-atom from any of the model compounds can then occur followed by radical trapping by TMIO to afford stable alkoxyamines.<sup>21</sup> This reaction is presented in Scheme 2-14.



**Scheme 2-14:** Compounds produced through the radical trapping of the model compounds with TMIO in the presence of *t*-butoxyl radicals.

Exposing the three model compounds to DTBH and TMIO at room temperature gave a mixture of products that were separated by preparatory HPLC, see Scheme 2-15. All the produced alkoxyamines were isolated and characterized fully with the exception of the two secondary radical trapped products of pentane, PEN-s and PEN-s'. NMR and GC-MS analyses of mixtures of these two isomers revealed that they appear in a 2.4:1 ratio of PEN-s: PEN-s'. It should also be noted that the product DMP-p is actually a mixture of diastereomers. The trapping at the primary position in DMP creates a stereocenter at the tertiary position. The yields for both sets of compounds will be reported as combined yields of isomers or diastereomers whether for PEN-s and PEN-s' or DMP-p.



**Scheme 2-15:** Products of the reaction of the model compounds with *t*-butoxyl radicals in the presence of TMIO

The product distributions shown in Table 2-8 were determined from the ratio of individual alkoxyamine products to the total produced for each model compound. The product distribution correlates to the relative rates of hydrogen abstraction from the different positions in the model compounds and their selectivity. The relative reactivity per hydrogen accounts for the varying number of H-atoms available at each position and represents a normalized relative reactivity per H-atom. Errors are presented as standard deviations from replicate HPLC analyses of one sample.

**Table 2-8:** Relative yields and reactivity of model compounds towards *t*-butoxyl radicals at room temperature, determined by HPLC.

Abstraction position	PEN		DMP		TMP	
	Relative yield (%)	Relative reactivity <sup>a</sup>	Relative yield (%)	Relative reactivity <sup>a</sup>	Relative yield (%)	Relative reactivity <sup>a</sup>
p	6.8 ± 0.1	1	20.9 ± 0.2	1	99.5 ± 0.2	1
s	93.1 ± 0.1	13.6 ± 0.2	4.24 ± 0.04	1.22 ± 0.02	0.5 ± 0.2	0.04 ± 0.01
t	-	-	74.9 ± 0.2	21.5 ± 0.2	-	-

a) Per H-atom and normalized to the primary position



In PEN there are an equal number of primary carbon-hydrogen bonds as there are secondary, yet over 90% of the H-atom abstractions happen at the secondary position. On a per hydrogen basis, the relative rate of hydrogen abstraction is 13.6 (secondary) : 1 (primary). DMP is more interesting than pentane. Here, there are primary, secondary and tertiary sites available for abstraction as well as a more sterically hindered secondary site. In contrast to pentane, over 95% of abstractions occur on the primary and tertiary sites with the remaining occurring at the secondary position. Tertiary abstraction dominates here which is to be expected based on the stability of the tertiary radical intermediate. On a per hydrogen basis, the relative rate of H-atom abstraction is 21.5 (tertiary) : 1.22 (secondary) : 1 (primary). It is interesting to note that when moving from PEN to DMP (the addition of two methyl groups at the 2 and 4 carbons) the ratio of H-atom abstraction at the secondary position compared to the primary position decreases by a factor of 11. TMP is the most sterically crowded about the secondary position of all the model compounds. In this case 99% of abstraction occurs at the primary position with almost no abstraction from the secondary position. Introducing two additional methyl groups and the removal of the tertiary position creates a relative rate of H-atom abstraction on a per hydrogen basis of 0.04 (secondary) : 1 (primary). These are alarming 315 and 28 fold decreases in the ratio of reactivity at the primary and secondary position when compared to PEN and DMP, respectively.

### 2.3 Discussion

The reported product distributions in Table 2-8 represent the trapping of the initially formed carbon-centered radical and not of a fast radical rearrangement prior to trapping. Dokolas previously carried out the reaction of *t*-butoxyl radicals and TMIO with DMP.<sup>19</sup> By increasing the TMIO concentration to favour radical trapping over rearrangement they found no change in the

product distribution, confirming that radical rearrangement was not occurring prior to radical trapping.

Several factors are responsible for the selectivity in H-atom abstraction from these model compounds. Among them, the most important are enthalpic and entropic effects, which contribute to the Gibbs free energy on the reaction. Enthalpic effects are represented by changes in bonding energy during the reaction. In this system, the driving force for enthalpic change is dictated by the reactivity of the *t*-butoxyl radical and the formation of *t*-butanol after H-atom abstraction as well as the stability of the resulting carbon-centered radical. Radical stability is affected by hyperconjugative effects, whereby primary radicals are less stable than secondary radicals which are less stable than tertiary radicals. The more stable the product the more exergonic the reaction, and according to the Hammond postulate this results in an earlier transition state with a lower barrier to activation. As a result, based on enthalpic contributions alone, one would expect abstraction from these model compounds to occur in the reverse order. That is, tertiary abstractions dominating, and primary abstractions are the least prevalent.

For pentane, indeed, this is what is seen. Over 90% of H-atom abstractions by *t*-butoxyl radicals occur at the secondary position. Being the least sterically hindered of all the model compounds the selectivity is likely dominated by enthalpic effects caused by the stability of the secondary radical intermediate over the relative instability of the primary radicals. If enthalpic effects were not dominating in this system, given random abstraction one would expect equal abstraction from both the secondary and primary position since PEN has six H-atoms available in each. It is when one moves to the other two model compounds that the enthalpic contribution begins to be outweighed by entropic forces.

Entropy represents the amount of disorder present in the system. The less ordering necessary in attaining the transition state the lower the barrier. In this system, one *t*-butoxyl radical reacts with one model compound to produce *t*-butanol and a radical intermediate that is

quickly trapped by TMIO. This mechanism applies regardless of the model compound. Differences in entropy of activation arise between sites in the restriction in the degrees of freedom (an increase in order) related to rehybridization or steric effects.

PEN, being the least sterically hindered model compound has the lowest entropic contribution to the Gibbs free energy of activation of all the model compounds. Here, abstraction at any position by a *t*-butoxyl radical occurs with minimal steric interference. During the abstraction there is also a rearrangement from a tetrahedral  $sp^3$  carbon center to a trigonal planar  $sp^2$  configuration. In PEN the restriction in freedom this causes is minimal. At a secondary center two linear carbon chains must be moved, along with the remaining C-H bond that is not being transferred.

In DMP two methyl groups are added, creating two more primary positions, two tertiary positions, and removing two secondary sites. Here, tertiary abstractions are most facile, accounting for 75% of all H-atom transfers. Enthalpically, this site has the largest driving force. Entropically, abstraction from the tertiary position requires the *t*-butoxyl radical to abstract from a site hindered by two methyl groups and an isobutane group as well as rehybridization.

The secondary site in DMP has the second largest enthalpic driving force, but only accounts for 4% of all abstractions. Entropically the *t*-butoxyl radical must abstract from a site hindered on each side by two isopropyl groups. The primary position is the least sterically hindered of all but also has the lowest enthalpic driving force. Yet, primary abstractions account for 21% of all the products.

The selectivity in DMP is caused by the balance of these two contributing forces, entropy and enthalpy. Based upon our knowledge of hyperconjugative effects and radical stability, enthalpically the ease of H-atom abstraction follows the order of tertiary > secondary > primary. With entropy, the primary position is the least sterically hindered with secondary and tertiary sites being less entropically favoured. Comparing all the positions, the enthalpic contribution to

abstraction at the tertiary site far outweighs the steric effects, and the greatest amount of H-atom transfers occurring here. At the secondary position, the steric effects far outweigh the entropic effects. The interference of the isopropyl groups with the *t*-butoxyl radical and rehybridization, restricting the freedom of the molecule, causes a large entropic barrier that the intermediate enthalpic driving force cannot overcome. The primary position is between these two. Here the entropic barrier is the lowest and the weakest enthalpic driving force of all the positions is enough to overcome this and provide a 21% relative yield of primary trapped radical products.

The strongest supporter of steric effects dominating these reactions is in the TMP data set, the bulkiest model compound used. Here abstraction occurs almost exclusively at the primary position accounting for 99% of all the products formed. As in PEN, this model compound is composed solely of primary and secondary sites. Again, the C-H BDEs of the primary and secondary positions dictate that the secondary sites should be the most reactive. That was the case in PEN, but here the steric bulk of the two isobutyl groups make the abstraction by *t*-butoxyl unfavorable. Even when accounting for the statistical contribution of having eighteen available primary H-atoms to two secondary, the primary sites are 23 times more reactive on a per hydrogen basis. Unlike in the abstractions from DMP, there is no balance and interplay between the two dominating forces, here entropic effects dictate the regioselectivity entirely.

The results presented here agree well with the literature. Dokolas carried out a similar study using 3-methylpentane and DMP in neat and benzene solutions using the thermal decomposition of di-*t*-butyl peroxalate at 60°C (as opposed to 25°C used here) as the source of *t*-butoxyl radicals and TMIO as the radical trap.<sup>19</sup> Their relative yields were within a few percent of those found here, 24, 9, and 67% for the primary, secondary, and tertiary products of DMP, respectively, and a selectivity of 16.9 (tertiary) : 2.3 (secondary) : 1 (primary). The authors present an extensive comparison of their results to those of Niki et al,<sup>14</sup> Beckwith,<sup>23</sup> and Beck<sup>39</sup> and find agreement, and the same holds true here. Also, both Camara<sup>13</sup> and Jacknow<sup>17</sup> found that

at higher temperatures the selectivity for the secondary sites increases. This is likely an example of kinetic control versus thermodynamic control. If entropic effects are playing a role in the regioselectivity of H-atom transfers, the steric effects present at the secondary position create a larger barrier to activation when compared to primary abstraction site. At higher temperatures more energy is available and a larger percentage of the reactants will have sufficient energy to proceed through the higher energy secondary abstraction pathway, which may help to explain the discrepancy between the DMP results of Dokolas<sup>19</sup> and those presented here.

Walling and Jacknow carried out a reactivity study using *t*-butyl hypochlorite as a radical initiator on n-butane from temperatures ranging from 0 to 40°C.<sup>17</sup> At 20°C they found a relative reactivity of 9.2 (secondary) : 1 (primary) which is in fair agreement with the results presented here for pentane. Camara carried out an EPR study on a series of alkanes, among them octane, decane, and DMP.<sup>13</sup> In octane and decane they found exclusively secondary abstraction with equal contributions from each secondary site. In DMP, Camara found only primary and tertiary abstractions at a ratio of 25:75 primary:tertiary, which is in good agreement with the results presented here. In the EPR study carried out by Niki,<sup>14</sup> as well as those by Camara, discrepancies between the results can be attributed in part to signal overlap in the EPR.

While no work has been done yet in this area with TMP, a fair amount of research has been carried out on intermediately hindered molecules between the set of model compounds used here. Beckwith found that in 2,2,4-trimethylpentane the majority of H-atom abstractions occur from the primary positions.<sup>23</sup> This was attributed to the statistical factor in favor of the primary positions but also to the sterics about the secondary and tertiary positions. This agrees with the results found for TMP where the larger steric bulk of this molecule only increases the reactivity of the primary positions over the secondary site.

Several studies have also been carried out on 3-methylpentane,<sup>15,19</sup> and 4-methylpentane.<sup>13</sup> Like DMP these molecules have primary, secondary and tertiary abstraction

sites. However, unlike DMP, in each case abstraction at the tertiary and secondary sites are unhindered and produce about the same number of tertiary and secondary radicals. Chenier et al<sup>15</sup> attributed this difference in reactivity between 3-methylpentane and DMP to the size of the substituents adjacent to the carbon center and to the degree of branching from the carbon chain.

Dokolas also investigated solvation of the *t*-butoxyl radical and its effect on the selectivity of these reactions.<sup>19</sup> Carrying out the trapping experiments in benzene, he found that in 3-methylpentane the relative yields did not change significantly per site, but in DMP reactivity at the secondary position decreased. In benzene, the *t*-butoxyl radical becomes solvated and for abstraction to occur this solvation shell must be displaced to allow the oxy radical to react with the C-H bond. This solvation shell not only increases the steric bulk of the radical, but also a restriction of freedom as the solvation shell is displaced. This in turn increases the entropic barrier to reaction.

This solvation effect supports the hypothesis that the steric effects at the secondary position are dominating the regioselectivity of these compounds. Extending this to the addition of methyl groups to the adjacent carbon, after the addition of two methyl groups from PEN to DMP and again to TMP, causes an 11 and 18 fold decrease of reactivity at the secondary position at each step, an overall 315 fold loss in reactivity in TMP compared to PEN.

Dokolas<sup>19</sup> also investigated overall reactivity of 3-methylpentane and DMP by comparing the amounts of methyl radical trapped products created from  $\beta$ -scission of the *t*-butoxyl radicals. Less reactive molecules will react slower with *t*-butoxyl allowing more time for  $\beta$ -scission to occur. Therefore, the larger the amount of methyl radical trapped products produced, the lower the reactivity of the compound. For 3-methylpentane an overall yield of 96.9% was achieved while for DMP this value dropped to 91.3%. Reactivity decreased even though the total number of C-H bonds increased when moving to DMP.

The same should hold true for the model compound set presented here. The overall reactivity of the least sterically hindered model compound, PEN, should be larger than that of DMP which is then larger than TMP. Expanding this to polymer grafting reactions, the hydrogen abstraction efficiencies in graft copolymerization should parallel this trend. Even though the introduction of methyl groups from PE to PP creates tertiary sites that are enthalpically more reactive, the increased entropic barriers decrease the overall reactivity of these compounds. At the extremes, TMP and polyisobutylene have no tertiary sites and any enthalpic gain is lost causing H-atom abstraction from this system to be the slowest.

## **2.4 Experimental**

### **2.4.1 General data**

$^1\text{H}$ ,  $^{13}\text{C}$ , COSY and HSQC nuclear magnetic resonance spectra were recorded on a Bruker spectrometer using (D)chloroform as a solvent at 400 and 100 MHz for  $^1\text{H}$  and  $^{13}\text{C}$  spectra, respectively. High resolution mass spectra were collected on a QStar XL QqTOF instrument. High-performance Liquid Chromatography (HPLC) was performed on a Waters system using a 600E system controller employing a model 600 pump, 2487 dual wavelength absorbance detector set to measure at 226 and 270 nm, and controlled by the Empower software program. An XBridge<sup>TM</sup> semipreparative C18 column (10 by 150 mm) with a 5  $\mu\text{m}$  diameter support size was used in all preparative and analytic studies. All analytical measurements were carried out using 85:15 methanol/water at a flow rate of 4 mL/min. For preparative separation of the radically trapped products, the pentane and 2,4-dimethylpentane adducts were isolated in the same fashion, while the isolation of the 2,2,4,4-tetramethylpentane radically trapped products were carried out using a mobile phase of 90:10 methanol/water at 4 mL/min. All preparative separation used a Waters fraction collector II set to collect a sample at 30 second intervals.

### 2.4.2 Substrates

Di-*t*-butyl hyponitrite was prepared by the previously published method of Mendenhall<sup>40</sup> recrystallized and stored in the freezer prior to use. The radical trap used in this study, 1,1,3,3-tetramethylisoindolin-2-oxyl (TMIO) was prepared according to the method of Solomon.<sup>38</sup> The model compounds; pentane (Caledon Laboratory Chemicals), 2,4-dimethylpentane (Aldrich), and 2,2,4,4-tetramethylpentane (Alfa Aesar) were used without purification. HPLC grade methanol (Fisher Scientific) was used as supplied and water obtained from a Mili-Q Synthesis A10 water purification system.

### 2.4.3 Radical trapping experiments

All radical trapping experiments were conducted in an analogous fashion to those previously used by Dokolas and Solomon,<sup>19</sup> but with slight modifications. Preparatory reactions contained di-*t*-butyl hyponitrite (1.0 mmol), 1,1,3,3-tetramethylisoindolin-2-oxyl (2.2 mmol) and either pentane, 2,4-dimethylpentane or 2,2,4,4-tetramethylpentane (60 mmol). The solutions were placed in a Schlenk flask and de-oxygenated by three freeze/pump/thaw cycles. Due to boiling point limitations, the 2,4-dimethylpentane and 2,2,4,4-tetramethylpentane reactions were carried out at 55°C for 20 hours (11 initiator half-lives),<sup>37</sup> while the pentane reaction was carried out at 30°C for 11 days (4 initiator half-lives). The reaction mixtures were then concentrated using a rotary evaporator, diluted in methanol to a concentration of 5 mg/100 µL and purified by semi-preparative reverse-phase HPLC.

Fractions were collected and combined, and then concentrated under reduced pressure until a white precipitate began to form, *but not until dryness*. The concentrated solution was then extracted with dichloromethane, dried (MgSO<sub>4</sub>) and filtered. The organic layer was concentrated, diluted with methanol and extracted once with an equal volume of hexanes. The hexanes were removed under reduced pressure to yield the alkoxyamines as viscous clear oils.



For quantitative analysis, the preparatory experiments were scaled down by a factor of 10 and carried out at 25°C for 11 days (2 initiator half-lives). The reaction mixtures were then concentrated using a rotary evaporator and diluted to a concentration of 5 mg/100  $\mu$ L and analyzed by reverse phase HPLC. Integrated HPLC peak areas were converted directly into percent yields under the assumption that the extinction coefficients for each alkoxyamine at 270 nm were identical.<sup>41</sup>

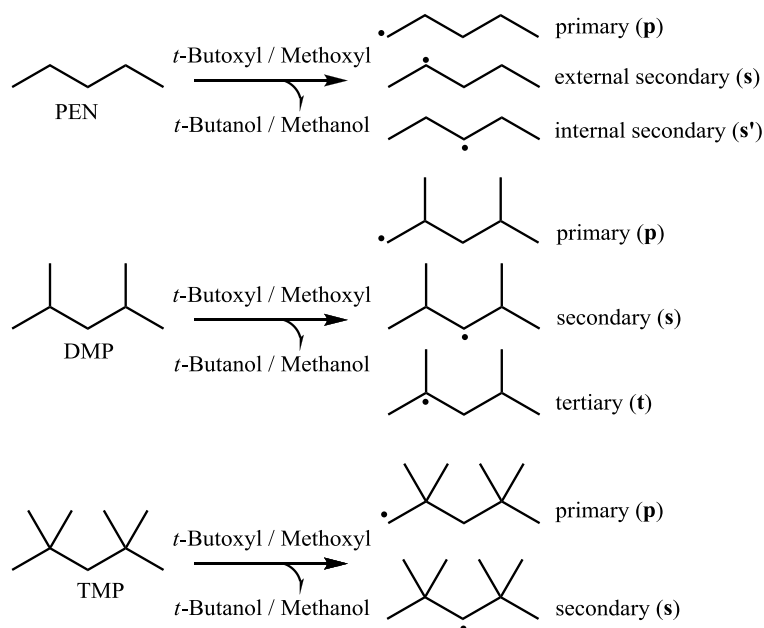
## Chapter 3

# Investigating the Regioselectivity of H-Atom Transfer in Polymer Model Compounds Using Quantum Chemical Calculations

### 3.1 Introduction

Computational methods provide an appealing route to determining the thermodynamic parameters of these chemical reactions. Enthalpic and steric effects that play a role in the regioselectivity and reactivity of polymer grafting reactions are not yet understood. To probe the regioselectivity of H-atom transfer in polyolefins, herein is described the use of model compounds to simulate the chemical environments present in the polymers that the initiators encounter during H-atom abstraction. Experimentally, this allows the reactions to be conducted using the model compounds as the solvent and avoids the need for high temperature reaction vessels. Computationally, model compounds also allow us to undertake higher level calculations. The smaller the molecule the lower the number of electrons present in the system. Computations generally scale exponentially with the number of electrons, and as a result, using smaller molecules does not require prohibitively long calculations.

Scheme 3-1 illustrates the possible H-atom abstraction products from the model compounds and their abbreviations that will be used in this study.



**Scheme 3-1:** Derived carbon centered radicals after reaction with *t*-butoxyl or methoxy radicals. p, s and t denote primary, secondary and tertiary derived radicals, respectively.

Since the main goal is to determine the thermodynamic parameters and their effect on the rate of H-atom abstraction, two radical initiators will be examined in this study to help expose the entropic effects. *t*-Butoxyl radicals will be used due to their popularity in the literature in addition to methoxyl radicals. Being the smallest alcoholic initiator possible, methoxyl allows the use of a less bulky initiator to compare with *t*-butoxyl. If there are steric interactions they should present themselves when comparing the two initiators.

## 3.2 Results

### 3.2.1 Bond dissociation enthalpies

The optimization of transition states and energy minima is generally the most time consuming step in the calculations. However, the geometries do not vary to a large extent

between methods. This fact can be used to advantage to perform high accuracy calculations while limiting computational costs. One popular strategy is to run the highly demanding structure optimizations at a lower level of theory then perform high level energy calculations on these structures. This method was used in both the DFT and MP2 methods herein, where the optimizations were carried out using a smaller basis set, 6-31G(d,p), and single point energy calculations using larger basis sets, 6-311++G(3df,3pd). In general, the larger the basis set size the more accurate the calculation. However, this is subject to the law of diminishing returns, with larger basis sets comes longer computational times.

The CBS-QB3<sup>42</sup> method takes these strategies one step further by carrying out the optimization and thermodynamic corrections using DFT. It then determines the energy at this geometry using an extremely high *ab initio* coupled cluster energy calculation (CCSD(T)/6-31+G(d')) followed by an MP2 (MP2/CBSB3) and an MP4 (MP4SDQ/CBSB4) calculation to extrapolate the couple cluster energy to an infinite basis set size. The thermodynamic corrections from the DFT calculation are then applied to this energy to achieve the enthalpic and entropic parameters. The CBS-QB3 level of theory is the highest used in this study. All three of these methods are used herein and their strengths and weaknesses assessed.

One way to measure the accuracy of the calculations is to calculate Bond Dissociation Enthalpies (BDEs) and compare them to available experimental values which are known to be accurate to better than 1 kcal/mol. BDEs are an efficient way to gauge the performance of the different methods as they take into account the stability of the formed radical and show how each method measures the strength of different bonds. The BDE estimations are less computationally intensive than determining transition states, as they require only the optimization of the compounds in their ground state and their radical counter parts.

**Table 3-1** Calculated Bond Dissociation Energies (BDE)  $\Delta H_{298}^{\circ}$  in kcal/mol at the UB3LYP/6-311++G(3df,3pd)//UB3LYP/6-31G(d,p), UMP2/6-311++G(3df,3pd)//UMP2/6-31G(d,p) and CBS-QB3 level of theory.

Mean Squared Error values were obtained by difference from direct experimental data or from similar compounds when no experimental value was available. Experimental BDEs were obtained from the CRC handbook.<sup>43</sup>

Compound	Position	Experimental	DFT		MP2		CBS-QB3	
			Calculated	Error	Calculated	Error	Calculated	Error
Butanol	O-H	106.3	101.5	-4.8	111.3	5.0	107.0	0.7
Methanol	O-H	105.2	100.1	-5.1	109.2	4.0	105.2	0.1
PEN	p	100.6 <sup>a</sup>	99.1	-1.5	100.4	-0.2	102.2	1.5
	s	99.2	95.1	-4.1	98.3	-0.9	99.1	-0.1
	s'	-	95.3	-	98.7	-	99.1	-
DMP	p	100.1 <sup>b</sup>	101.0	0.9	103.0	2.9	104.4	4.2
	s	-	95.1	-	99.6	-	99.6	-
	t	95.7 <sup>c</sup>	91.8	-3.9	96.8	1.1	96.9	1.2
TMP	p	100.3 <sup>d</sup>	98.1	-2.2	100.1	-0.2	101.5	1.2
	s	-	93.9	-	98.0	-	98.2	-
<b>MSE</b>			<b>12.68</b>		<b>7.42</b>		<b>3.42</b>	

a) butane b) 2-methylpropane c) 2-methylbutane d) 2,2-dimethylpropane

All three methods were examined and the results are found in Table 3-1. The mean squared error is presented for each method. DFT is on average the least accurate, followed by MP2 and CBS-QB3. CBS-QB3 is by far the most accurate, but importantly CBS-QB3 does much better at calculating the O-H bond strength in methanol and butanol. Methoxyl and *t*-butoxyl radicals will be used as the H-atom abstractor in all the calculations, as a result their accuracy will be an important source of error present throughout the data.

### 3.2.2 Thermodynamic parameters

The next step is to determine the kinetics and thermodynamic parameters for the reactions of interest, namely the H-atom abstraction at each position in PEN, DMP, and TMP. The lowest energy states of the products and reactants were optimized and transition states located at each level of theory. All transition states were located on first order saddle points, and their corresponding negative frequencies were checked to ensure the transition state corresponded to H-atom transfer.

### 3.2.2.1 Reaction thermodynamics

The reaction thermodynamics for methoxyl and *t*-butoxyl H-atom abstractions are shown below in Table 3-2.

**Table 3-2:** Thermodynamic reaction parameters in kcal/mol or cal/molK of the *t*-butoxyl and methoxyl H-atom abstraction as a function of the level of theory at 298.15 K and 1 atm. DFT and MP2 values were calculated at the UB3LYP/6-311++G(3df,3pd)//UB3LYP/6-31G(d,p) and UMP2/6-311++G(3df,3pd)//UMP2/6-31G(d,p) theory level.

Compound		PEN			DMP			TMP	
Position		p	s	s'	p	s	t	p	s
<b><i>t</i>-Butoxyl</b>									
DFT	$\Delta H_r$	-2.4	-6.4	-6.2	-0.5	-6.5	-9.7	-3.5	-7.6
	$\Delta G_r$	-3.9	-8.0	-7.7	-0.9	-7.9	-11.4	-4.3	-8.9
	$\Delta S_r$	4.9	5.3	5.1	1.4	4.9	5.5	2.8	4.2
MP2	$\Delta H_r$	-10.9	-13.0	-12.6	-8.3	-11.8	-14.5	-11.3	-13.3
	$\Delta G_r$	-12.0	-14.3	-13.9	-8.8	-13.1	-15.8	-12.0	-14.3
	$\Delta S_r$	3.5	4.3	4.5	1.7	4.4	4.5	2.3	3.2
CBS-QB3	$\Delta H_r$	-4.8	-7.9	-7.9	-2.6	-7.4	-10.1	-5.5	-8.8
	$\Delta G_r$	-6.5	-9.5	-9.5	-3.0	-8.6	-11.7	-6.3	-10.0
	$\Delta S_r$	5.6	5.4	5.4	1.3	3.9	5.2	2.6	3.9
<b>Methoxyl</b>									
DFT	$\Delta H_r$	-1.0	-5.0	-4.8	0.9	-5.1	-8.3	-2.1	-6.2
	$\Delta G_r$	-2.8	-6.9	-6.6	0.2	-6.8	-10.2	-3.2	-7.8
	$\Delta S_r$	5.8	6.2	6.1	2.3	5.8	6.5	3.7	5.1
MP2	$\Delta H_r$	-8.7	-10.9	-10.5	-6.2	-9.6	-12.3	-9.1	-11.2
	$\Delta G_r$	-10.1	-12.5	-12.1	-7.0	-11.3	-14.0	-10.1	-12.4
	$\Delta S_r$	4.6	5.4	5.5	2.8	5.5	5.6	3.4	4.3
CBS-QB3	$\Delta H_r$	-3.1	-6.1	-6.1	-0.9	-5.7	-8.3	-3.8	-7.1
	$\Delta G_r$	-5.0	-8.1	-8.1	-1.6	-7.1	-10.2	-4.9	-8.5
	$\Delta S_r$	6.6	6.5	6.5	2.3	4.9	6.3	3.7	4.9

Both systems show the expected characteristics, with tertiary radicals being more stable than secondary radicals, which in turn are more stable than primary radicals. Enthalpically, the stabilization provided by the more substituted positions lowers the energy of radicals relative to one another. Entropically, the effects are most dramatic when removing a H-atom from a tertiary position, but also from secondary positions. After transfer of the H-atom, the carbon center is rehybridized to a pyramidal type hybridization from tetrahedral. This allows the substituents on

the carbon center to separate from one another and reduce steric hindrance providing an increase in entropy. This effect becomes larger as the reactive site moves from one C and three smaller H atoms in a primary abstraction to three C bonds and one H bond in a tertiary abstraction. The larger groups on a tertiary radical benefit more from the added space than smaller substituents. All reactions are exergonic, except for the primary abstraction from DMP by methoxyl as calculated by the DFT method.

### 3.2.2.2 Transition state thermodynamics

The difference in thermodynamic parameters can also be determined between the reactants and the transition state. These calculations quantify the entropic, enthalpic, and Gibbs free energy barriers to activation. To begin, Table 3-3 presents the enthalpic parameters for the methoxy and *t*-butoxyl H-atom abstractions.

**Table 3-3:**  $\Delta H^\ddagger$  values in kcal/mol of the *t*-butoxyl and methoxyl H-atom abstraction as a function of the level of theory at 298.15 K and 1 atm. DFT and MP2 values were calculated using an unrestricted formalism at the UB3LYP/6-311++G(3df,3pd)//UB3LYP/6-31G(d,p) and UMP2/6-311++G(3df,3pd)//UMP2/6-31G(d,p) level.

Compound	PEN			DMP			TMP	
	p	s	s'	p	s	t	p	s
Method	<b><i>t</i>-Butoxyl</b>							
DFT	7.4	6.7	6.7	8.0	7.9	6.5	8.3	9.7
MP2	5.7	3.3	3.3	4.9	2.9	2.1	4.5	3.7
CBS-QB3	4.9	1.5	1.5	4.1	2.0	0.7	3.8	2.4
	<b>Methoxyl</b>							
DFT	7.9	4.9	4.9	7.3	5.1	3.9	7.5	5.4
MP2	7.8	5.3	4.8	6.9	4.0	3.2	6.7	3.3
CBS-QB3	6.7	3.7	3.7	6.0	2.4	1.7	5.8	1.8

Enthalpically, each transition state follows the expected trend, where the barrier to abstraction decreases from primary, to secondary, to tertiary H-atoms. This trend is found in results obtained with all the methods, except for the DFT calculations on DMP and TMP. In DMP DFT predicts almost equal enthalpic barriers at the secondary and primary abstraction site, while in TMP barrier at the secondary site is 1.4 kcal/mol larger than at the primary. This effect is likely

due to the failure of DFT to capture dispersion interactions in these congested transition states. Using the smaller methoxyl initiator, we see that DFT now produces the expected enthalpic trends in each model compound. The enthalpic barriers also differ by about 1 to 2 kcal/mol between the methoxy and *t*-butoxyl radicals, due to their different BDEs. DFT produces the highest enthalpic barriers, while CBS-QB3 the lowest. The MP2 and CBS-QB3 calculations seem to be producing the trends that one would expect to find in the data. The entropic parameters can also be calculated, and they are shown in Table 3-4.

**Table 3-4:**  $T\Delta S^\ddagger$  values in kcal/mol of the *t*-butoxyl and methoxyl H-atom abstraction as a function of the level of theory at 298.15 K and 1 atm. DFT and MP2 values were calculated using an unrestricted formalism at the UB3LYP/6-311++G(3df,3pd)//UB3LYP/6-31G(d,p) and UMP2/6-311++G(3df,3pd)//UMP2/6-31G(d,p) level.

Compound Position	PEN			DMP			TMP	
	p	s	s'	p	s	t	p	s
Method	<b><i>t</i>-Butoxyl</b>							
DFT	-9.6	-10.9	-10.9	-11.0	-11.7	-12.2	-10.5	-11.9
MP2	-10.3	-11.3	-11.3	-11.1	-11.7	-12.0	-11.0	-12.0
CBS-QB3	-9.7	-10.6	-10.6	-10.7	-11.3	-12.0	-10.8	-12.3
	<b>Methoxyl</b>							
DFT	-8.7	-9.7	-9.7	-10.0	-10.6	-10.8	-9.8	-10.8
MP2	-8.6	-9.0	-9.5	-9.8	-10.6	-10.5	-10.4	-11.1
CBS-QB3	-9.0	-9.2	-9.2	-10.2	-10.8	-10.8	-9.9	-10.9

Entropically, there is also a trend of increasing steric strain as the position of abstraction moves to more sterically hindered sites and the entropy of activation decreases when moving from *t*-butoxyl radicals to the less hindered methoxyl radical. All levels of theory follow this trend of decreasing entropic strain as the initiator changes to a smaller molecule.



**Table 3-5:**  $\Delta G^\ddagger$  values in kcal/mol of the *t*-butoxyl and methoxyl H-atom abstraction as a function of the level of theory at 298.15 K and 1 atm. DFT and MP2 values were calculated using an unrestricted formalism at the UB3LYP/6-311++G(3df,3pd)/UB3LYP/6-31G(d,p) and UMP2/6-311++G(3df,3pd)/UMP2/6-31G(d,p) level.

Compound	PEN			DMP			TMP	
Position	p	s	s'	p	s	t	p	s
Method	<b><i>t</i>-Butoxyl</b>							
DFT	17.0	17.6	17.6	19.1	19.6	18.7	18.9	21.7
MP2	15.9	14.7	14.6	16.0	14.5	14.0	15.5	15.7
CBS-QB3	14.6	12.1	12.1	14.8	13.3	12.7	14.6	14.7
	<b>Methoxyl</b>							
DFT	16.6	14.6	14.6	17.2	15.7	14.7	17.2	16.2
MP2	16.4	14.3	14.3	16.7	14.6	13.8	17.1	14.4
CBS-QB3	15.7	12.9	12.9	16.2	13.2	12.5	15.6	12.6

Together, both the enthalpic and entropic contributions are weighed together in the Gibbs free energy of activation shown in Table 3-5. With the *t*-butoxyl radical data, both MP2 and CBS-QB3 provide consistent results and trend similarly, their difference being about 2 kcal/mol. However, free energy barriers from the DFT calculations are much larger than those provided by MP2 and the CBS-QB3 methods and they do not trend in the same manner. These values are likely accounted for by the over estimation of the DFT enthalpic parameters.

When examining the change of initiator, MP2 and CBS-QB3 results no longer provide the same trends. MP2 stays consistent with the *t*-butoxyl results and trends in the same manner as before, while in CBS-QB3 the activation energy of the secondary position in TMP, now becomes 3 kcal/mol lower than with *t*-butoxyl. In general, CBS-QB3 and MP2 provide consistent results while the DFT data does not agree with these, nor produce the trends one would expect in the data.

### 3.2.3 Estimating rate constants and preexponential factors

Another way to quantify these results is by estimating the rate constants of the reaction between the initiators and each position on the model compounds. Using the Gibbs free energies

of activation found in Table 3-5, Equation 3-1 can be invoked to estimate rate constants for H-atom abstractions from each position.

$$k = \frac{k_B T}{h c_0} e^{(\Delta S^\ddagger/R)} e^{(-\Delta H^\ddagger/RT)}$$

**Equation 3-1:** Rate constant, as defined by the Eyring equation

Where  $k$  is the rate coefficient,  $k_B$  is the Boltzmann constant,  $T$  is the temperature,  $h$  is Plank's constant,  $\Delta S^\ddagger$  and  $\Delta H^\ddagger$  are the entropic and enthalpic barriers to the reaction,  $R$  is the ideal gas constant, and  $c_0$  is a normalization factor required for a bimolecular reaction such that  $c_0 = P/RT$  where  $P$  is the pressure. The Eyring equation looks similar to the Arrhenius equation and one might think that  $\frac{k_B T}{h c} e^{-\Delta S^\ddagger/R}$  is equivalent to  $A$ , the preexponential factor, and  $\Delta H^\ddagger$  is equal to  $E_a$ , the activation energy. The error in this assumption is that the Eyring equation is based on transition state theory and based on microscopic rate constants for a single reaction path, whereas the Arrhenius equation is based upon empirical observation and macroscopic rate constants independent of reaction path.<sup>44</sup> For a bimolecular reaction the relation between the Eyring and Arrhenius equations is

$$E_a = \Delta H^\ddagger + RT$$

$$\Delta S^\ddagger = 4.574(\log A - 10.753 - \log T)$$

Using this relation the preexponential factors can be estimated. The preexponential factors are convenient because they provide another means to compare the entropic barriers at each H-atom transfer site and at the same time allow for comparison to experimental data. The preexponential factors have been calculated for the *t*-butoxyl H-atom abstractions and are presented in Table 3-6.

**Table 3-6:** logA values for the *t*-butoxyl radical H-atom abstraction as a function of the level of theory at 298.15 K and 1 atm. DFT and MP2 values were calculated using an unrestricted formalism at the UB3LYP/6-311++G(3df,3pd)//UB3LYP/6-31G(d,p) and UMP2/6-311++G(3df,3pd)//UMP2/6-31G(d,p) level.

Compound	PEN			DMP			TMP	
	p	s	s'	p	s	t	p	s
DFT	11.1	10.8	10.8	10.8	10.7	10.6	10.9	10.6
MP2	11.0	10.8	10.8	10.8	10.7	10.6	10.8	10.6
CBS-QB3	11.1	10.9	10.9	10.9	10.8	10.6	10.9	10.5

By using the entropic and enthalpic activation values in Equation 3-1, the reaction rate constants for H-atom abstraction for each model compound can be estimated. These values have been tabulated in Table 3-7 and Table 3-8 for the *t*-butoxyl and methoxyl radical initiated reactions, respectively.

**Table 3-7:** Estimated rate constants,  $k_{298} \times 10^{-2} \text{ (M}^{-1}\text{s}^{-1}\text{)}$ , for H-atom abstraction from the model compounds by *t*-butoxyl radicals as a function of the level of theory. DFT and MP2 values were calculated using an unrestricted formalism at the UB3LYP/6-311++G(3df,3pd)//UB3LYP/6-31G(d,p) and UMP2/6-311++G(3df,3pd)//UMP2/6-31G(d,p) level.

Compound	PEN			DMP			TMP	
	p	s	s'	p	s	t	p	s
DFT	0.5	0.2	0.2	0.02	0.01	0.03	0.02	0.0002
MP2	3.2	26.6	27.9	2.9	33.9	77.8	6.2	5.0
CBS-QB3	28.7	1981.8	1981.8	22.0	276.4	748.7	28.6	25.3

**Table 3-8:** Estimated rate constants,  $k_{298} \times 10^{-2} \text{ (M}^{-1}\text{s}^{-1}\text{)}$ , for H-atom abstraction from the model compounds by methoxyl radicals as a function of the level of theory. DFT and MP2 values were calculated using an unrestricted formalism at the UB3LYP/6-311++G(3df,3pd)//UB3LYP/6-31G(d,p) and UMP2/6-311++G(3df,3pd)//UMP2/6-31G(d,p) level.

Compound	PEN			DMP			TMP	
	p	s	s'	p	s	t	p	s
DFT	1.0	29.3	29.3	0.3	4.6	26.3	0.4	2.0
MP2	1.5	54.3	52.5	0.8	31.2	125.5	0.4	45.6
CBS-QB3	4.5	525.1	525.1	1.9	337.6	1087.0	5.2	860.2

An interesting trend arises in the data when the rate constants at the secondary and primary positions are compared. Shown in Table 3-9 are the estimated rate constants at the CBS-QB3 level of theory for H-atom abstraction from the model compounds by *t*-butoxyl and methoxyl radicals.

**Table 3-9:** Estimated rate constants,  $k_{298} \times 10^{-2}$  ( $M^{-1}s^{-1}$ ), for H-atom abstraction from the model compounds by *t*-butoxyl and methoxyl radicals at the CBS-QB3 level of theory determined at 298.15 K

Compound	<b>t-Butoxyl</b>			<b>Methoxyl</b>	
	p	s		p	s
PEN	28.7	1981.8		4.5	525.1
DMP	22.1	276.4		1.9	337.6
TMP	28.6	25.3		5.2	860.2

Regardless of the compound, the least sterically hindered primary position maintains approximately the same rate of abstraction. However, using *t*-butoxyl a dramatic order of magnitude decrease in reactivity occurs at the secondary position when moving to more sterically hindered compounds. Using the less bulky methoxy radical, the rate of abstraction at the secondary site is relatively compound independent.

Using the estimated rate constants in Table 3-7 and Table 3-8, the overall relative reactivities of the model compounds can be estimated. Using DMP as an example, the total rate of H-atom transfer can be expressed as

$$\frac{dHAT}{dt} = K_{HAT_{DMP}}[DMP]$$

Where  $\frac{dHAT}{dt}$  the rate of H-atom is transfer, and  $K_{HAT_{DMP}}$  is the overall H-atom transfer rate constant for DMP.  $K_{HAT_{DMP}}$  is composed of the total reaction rate constants at each position within DMP, i.e.

$$K_{HAT_{DMP}} = K_P + K_S + K_T$$

Where  $K_P$ ,  $K_S$ , and  $K_T$  are the total reaction rate constants for the primary, secondary and tertiary positions and are determined by taking the rate constants at each position and multiplying

them by the number of H-atoms available in that compound. As a result, for DMP,  $K_p = 12k_p$ ,  $K_S = 2k_s$ , and  $K_T = 2k_t$  where  $k_p$ ,  $k_s$ , and  $k_t$  are the reaction rate constants found in Table 3-7 and Table 3-8. Carrying this process out for each model compound and both initiators generates the data presented in Table 3-10, which was calculated at the CBS-QB3 level of theory.

**Table 3-10:** Estimated relative reactivity,  $k_{298} \times 10^{-2} \text{ (M}^{-1}\text{s}^{-1}\text{)}$ , for H-atom abstraction from the model compounds by *t*-butoxyl and methoxyl radicals at the CBS-QB3 level of theory determined at 298.15 K

Compound	<i>t</i> -Butoxyl	Methoxyl
$K_{HAT_{PEN}}$	12063	3177
$K_{HAT_{DMP}}$	2315	2872
$K_{HAT_{TMP}}$	565	1813

The relative reactivities clearly show a trend of decreasing reactivity as one moves from the least sterically hindered model compounds to the most hindered using the bulkier *t*-butoxyl radical. However, using the less bulky methoxyl initiator the trend still exists but less dramatically, 1.75:1 rather than 21.4:1. Using the same rate constants the reactivity of their polymer counterparts can also be estimated.

The results presented in Table 3-11 represent the relative reactivities per monomer unit, that is ethylene ( $C_2H_4$ ) for PE, propylene ( $C_3H_6$ ) for PP, and isobutylene ( $C_4H_{10}$ ) for PIB from these gas phase calculations. The same trend appears for the polymers as well, with decreased reactivity in the bulkier polymers with *t*-butoxyl while only a slight decrease using methoxyl.

**Table 3-11:** Estimated relative reactivity,  $k_{298} \times 10^{-2} \text{ (M}^{-1}\text{s}^{-1}\text{)}$ , for H-atom abstraction from the polymers by *t*-butoxyl and methoxy radicals at the CBS-QB3 level of theory determined at 298.15 K.

Compound	<i>t</i> -Butoxyl	Methoxyl
$K_{HAT_{PE}}$	7927	2100
$K_{HAT_{PP}}$	1368	1768
$K_{HAT_{PIB}}$	222	1751

### 3.2.4 Product Distributions

Rate constants are a useful tool to relate the reactivity between positions, but they cannot be directly applied to the relative rates of reactions between positions without considering the statistical number of available positions in each molecule. Experimental product distributions can be estimated that take this factor into account, but it must be stressed that their values are determined from gas phase rate constants and that these do not directly when compared to condensed phase reactions. In solution, the initiator will be solvated, and once a radical is formed and escapes the solvent cage containing its radical counterpart, it will remain solvated (for a brief instant) until it can abstract an H-atom. This solvation effect will increase the bulk of the hydrogen abstractor, and amplify any steric effects present in the gas phase. In order for the radical to react with a primary position, less of its solvation shell needs to be disrupted in comparison with a secondary or tertiary position

**Table 3-12:** Estimated product distributions of radical trapping experiments from rate constants calculated at 25 °C as a function of the level of theory. DFT and MP2 values were calculated using an unrestricted formalism at the UB3LYP/6-311++G(3df,3pd)//UB3LYP/6-31G(d,p) and UMP2/6-311++G(3df,3pd)//UMP2/6-31G(d,p) level.

Compound	PEN			DMP			TMP	
	p	s	s'	p	s	t	p	s
<b>t-Butoxyl</b>								
DFT	74%	17%	9%	72%	5%	22%	100%	0%
MP2	11%	59%	31%	14%	26%	60%	92%	8%
CBS-QB3	1%	66%	33%	11%	24%	65%	91%	9%
<b>Methoxyl</b>								
DFT	3%	64%	32%	6%	14%	80%	62%	38%
MP2	3%	66%	32%	3%	19%	78%	8%	92%
CBS-QB3	1%	66%	33%	1%	24%	76%	5%	95%

The estimated product distributions were calculated according to the equations found in Appendix A and are presented in Table 3-12. The most notable differences are found when comparing the DMP and TMP product distributions between the two initiators. In DMP, when methoxyl radicals are used the tertiary position becomes more accessible to the smaller initiator and reactivity at the primary position suffers. In TMP, the secondary position also becomes more

accessible and almost all of the abstraction occurs at the secondary site, where with *t*-butoxyl radicals abstraction happened almost exclusively at the primary position.

### 3.2.5 Transition state structures

In Figure 3-1 the transition state structures of the *t*-butoxyl and methoxyl H-atom abstractions from the secondary position in TMP are presented. These images represent stationary points at the saddle point of the lowest energy pathway between products and reactants.

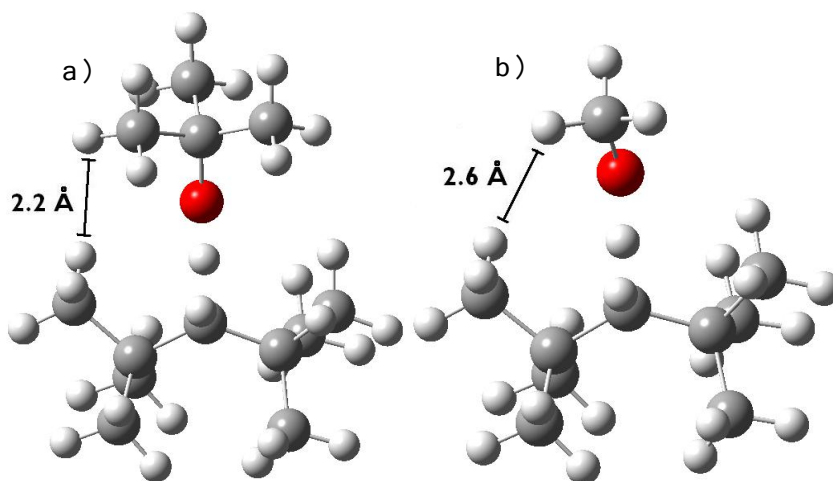


**Figure 3-1:** Computed geometries of transition structures for H-atom abstraction from 2,2,4,4-tetramethylpentane (TMP) by: a) *t*-butoxyl; and b) methoxyl radicals at the CBS-QB3 level of theory.

The closest distances between H-atoms on the alkoxy radical and methyl groups on TMP are labeled. In the *t*-butoxyl case, not only is there a 0.4 Å difference between the two structures, but the methyl groups on the opposite side are also closer in proximity than in the methoxy radical case. For methoxyl, it can pass in between the *t*-butyl groups on either side of the secondary position relatively unopposed when compared to *t*-butoxyl, which has its own *t*-butyl groups that have to compete. Additionally, if the secondary position is considered to be stationary in space, each of the *t*-butyl groups on DMP and the initiator are spinning and will interfere with one another. In the end, the radii of the spinning groups dictate steric hindrance about the secondary position.

This steric effect can also be seen to a lesser extent in DMP. With the smaller initiator the secondary and tertiary positions become more accessible to H-atom transfer. Because of this, primary abstraction suffers, while the oxygen radical favours abstraction at the tertiary over the secondary position due to the lower enthalpic barrier and comparable entropic barriers to activation. If the transition state structures of the *t*-butoxyl and methoxyl hydrogen abstraction reaction from DMP in the secondary position are examined, shown in Figure 3-2, similar to the TMP, there is a 0.4 Å difference between the two. Similarly to TMP, the isopropyl groups adjacent to the secondary position also rotate and will have the same effective radius as the *t*-butyl groups in TMP. Because of this, methoxyl radicals can abstract from the secondary (or tertiary) position more readily than *t*-butoxyl radicals.

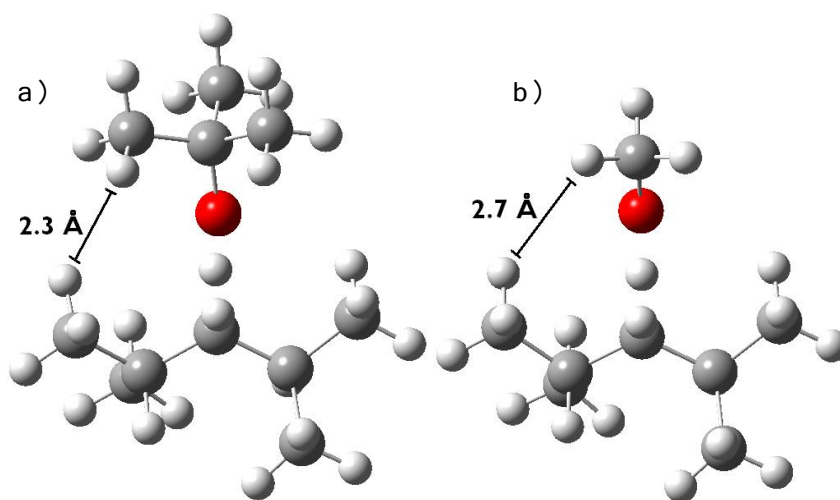


**Figure 3-2:** Computed geometries of transition structures for H-atom abstraction from 2,4-dimethylpentane (DMP) by: a) *t*-butoxyl; and b) methoxyl radicals at the CBS-QB3 level of theory.

It should also be noted, that an alternative transition state was also found for H-atom abstraction from all the secondary positions. The structures shown above in Figure 3-1 and Figure 3-2 are in an orientation where the initiators are pointing above or away from the carbon backbone. In an alternative structure, the alkoxy radical lies above the backbone. In this form, the Gibbs free energy of activation is 2.5 kcal/mol higher in energy than for the non-eclipsed



case. These two states were Boltzmann averaged to determine the effect on rate predictions. It was found that the extra barrier imposed by the eclipsed form was too large, and ultimately did not affect the final prediction. For this reason it was ignored as a transition state that was too high in energy to be relevant. Alternate transition states were also located for the primary H-atom abstraction transition states. In those cases the alternative transition states were so close in energy that their effect was negligible.

### 3.3 Discussion

Throughout the data presented, DFT consistently provided the least accurate results and often generated trends in ways that were inconsistent. Because of this, higher level calculations (MP2 and CBS-QB3) had to be carried out to ensure the trends observed in the data were not a limitation of quantum chemical calculations, but of the DFT method used. One of the downfalls to using DFT is its inability to correctly treat dispersion binding in molecular systems. Due to DFT's use of the independent electron approximation, it fails to incorporate long-range dispersion interactions. Dispersion interactions are either repulsive or attractive forces of instantaneous dipole moments within molecules. Several dispersion interaction DFT methods have developed over the past years which attempt to address this issue.<sup>45</sup> When modeling H-atom abstraction reactions from polymer systems, steric interactions and therefore dispersion effects play a significant role. Because of this, the UB3LYP DFT functional used here provides the least accurate enthalpic parameters in these crowded transition states.

Table 3-1 presents the calculated BDEs and their errors relative to experimental data where available, either directly or estimated from experimental values obtained for similar chemical structures. There is one outlier in the data set which appears in all the methods, the error associated with the BDE estimation at the primary position of DMP. In the DFT calculations, this value is at 0.9 kcal/mol, where all other DFT errors are well under -1. The same is true for the

MP2 and CBS-QB3 calculations, if one looks only at C-H BDE estimations, this outlier is 1.8 kcal/mol and 2.7 kcal/mol higher in energy than the closest error in the MP2 and CBS-QB3 calculations respectively. If this value is removed, which could be appropriate given that the experimental value is not direct but is taken from the primary BDE of 2-methylpropane, the mean squared errors now become 14.66, 7.22, and 0.97 for the DFT, MP2 and CBS-QB3 methods respectively.

Carrying this out does not change the trend in accuracy; CBS-QB3 is still the most accurate; with the outlier the CBS-QB3 method is almost 4 times more accurate than DFT, and 15 times more accurate without. The value was left in Table 3-1 as the experimental value was taken from the most similar molecule where an experimental BDE was available for that position. Most of the values in Table 3-1 come from experimental approximations, and while it appears that in the case of a primary C-H BDE from 3-methylpentane approximating the primary position in DMP is not accurate, this was not known until the comparison with the other BDEs took place. From the data, this approximation appears to be poor, but it was retained for the sake of completeness.

If the outlier previously discussed is ignored, each method is relatively consistent in the errors associated with C-H BDE estimation. However, there are striking differences in the O-H BDE errors between the methods. The MP2 method calculated the O-H bonds in methanol and butanol to be at least 4 kcal/mol stronger, and DFT determines the bond strength to be about 5 kcal/mol weaker. If the O-H bond is calculated to be too strong, as in MP2, the Gibbs free energy for abstraction will be too small, causing rate estimates to be too high. Conversely, in DFT where the O-H bond is 5 kcal/mol weaker than the experimental value, one can expect the calculated rates of H-atom abstraction to be smaller. This is indeed the case in DFT as it has the lowest estimated rate constants of all the methods used. The smallest errors associated with O-H BDEs arise from the CBS-QB3 calculations. It is important to note that all the abstractions are

performed by either methoxyl or *t*-butoxyl radicals. Any errors associated with O-H BDEs will be consistent and present in all the calculations. As such, minimizing this error will affect all the calculations and improve the accuracy of the data set. CBS-QB3 is by far and away the best method for approximating these bond strengths. Also, for the only hydrocarbon where there is direct experimental data (the secondary position of pentane) CBS-QB3 is best at estimating the bond strength. Overall, CBS-QB3 appears to be the best at calculating BDEs for this system, which is reassuring since it is the highest level calculation of the set.

The transition state thermodynamics provide the greatest insight into the differences in regioselectivity between the model compounds. Enthalpically, each transition state follows the expected trend in the MP2 and CSB-QB3 calculations, where the barrier to abstraction lowers from primary, to secondary, to tertiary H-atoms. Due to the inability of DFT to correctly address dispersion interactions,<sup>45</sup> it does not produce these trends in the *t*-butoxyl data set, but does so in the less crowded methoxyl H-atom abstractions. Entropically, the barriers to activation increase when moving from primary positions to secondary and finally to the tertiary abstraction site. This entropic stress is caused by two factors. The first, and major contributor, is the rearrangement of the carbon centre where the radical is forming. The opening up of the tetrahedral center to form an almost planar, pyramidal structure, restricts the degrees of freedom and decreases the entropy in the transition state. The arrangement of the radical initiator must also be taken into account, as it begins to abstract the H-atom its range of motion and freedom is also decreased.

The second effect is the presence of the radical initiator, its size, and how much of the carbon backbone has to be displaced for the H-atom to be abstracted. This can be seen when comparing entropic contributions between the methoxy and *t*-butoxyl calculations in Table 3-4, where moving from the bulkier *t*-butoxyl radical to methoxyl decreases the entropy of activation by around 0.6 kcal/mol. If entropic strain through rearrangement is the same between initiators,

then the difference in entropic values corresponds to steric interactions with the initiator and the carbon backbone of the model compounds.

Combining the entropic and steric factors to form the Gibbs free energy and from this estimating rate constants for H-atom transfer in Table 3-7 and Table 3-8 allows for a simple way of examining regioselectivity, and one which is amenable to comparison with previously determined experimental results. In general, CBS-QB3 and MP2 provide consistent results in the *t*-butoxyl data set, while the DFT data does not agree with these or produce rational trends. The same trends can also be found in the Gibbs energy values in Table 3-5, as the Gibbs free energy is the only variable in the estimation of the rate constant using Equation 3-1.

Before examining the trends in the rate constants, their accuracy should first be assessed. In 1978, Pauy et al.<sup>9</sup> determined a variety of rate constants for H-atom abstraction using laser flash photolysis. Among those values, he determined a value of  $8.8 \times 10^5 \text{ M}^{-1}\text{s}^{-1}$  for the abstraction from cyclopentane using *t*-butoxyl. Using the secondary position in PEN as a comparison, both DFT and MP2 fall short of this by about four orders and two orders of magnitude, respectively, and CBS-QB3 approaches this with a value of  $2 \times 10^5 \text{ M}^{-1}\text{s}^{-1}$ . Trend wise, both CBS-QB3 and MP2 provide the same results, but coupled with the BDE assessment, CBS-QB3 provides the most accurate results.

The preexponential factors obtained in Table 3-6 can also be assessed. Sway,<sup>46</sup> through gas phase measurements at 0.66 atm and 137 °C, found a logA value for the *t*-butoxyl H-atom abstraction from cyclohexane to be  $10.43 \pm 0.05$ , while Li<sup>47</sup> found a value of  $10.0 \pm 0.5$  for the abstraction from hexane at 299 °C and 1 atm. These experimental results represent overall preexponential factors obtained from H-atom abstraction from all the available sites. Computationally, the values in Table 3-6 represent logA values from each individual site. However, the product distributions estimated in Table 3-12 suggest that 99% of abstractions occur at the secondary positions in pentane, as a result we can use the logA values determined at

the secondary sites to compare to the experimental data. All methods approach the experimental values, obtaining a logA of 10.8 by DFT and 10.9 from MP2 and CBS-QB3 for the secondary abstraction from pentane.

Ignoring for now the DFT results, the most striking data in Table 3-7 is the decrease in reactivity at the secondary position between the model compounds. Within each model compound the differences in reactivities are not drastically different, and would not at first indicate anything different than expected – the rate of reaction is fastest at the tertiary positions, and slowest at the primary positions. The first indication towards steric effects playing a role in these reactions is seen in the TMP data set. Here, and unlike PEN or DMP, the secondary position has essentially the same reaction rate as the primary position. Considering that the secondary position of TMP is the most sterically hindered secondary position of all the model compounds studied here, it is clear that entropic effects are playing a role in these reactions.

Additionally, if the rates between model compounds at the primary and secondary positions are examined, see Table 3-9, some interesting trends present themselves. Across the primary positions the rate constants remain essentially the same between each compound. This is to be expected as the primary positions are the most remote; the *t*-butoxyl radical can interact with these H-atoms without interfering too much with the rest of the molecule. Interestingly, if the reaction rate constants at the secondary positions are compared, moving to more sterically hindered sites (going from PEN, to DMP, to TMP), the rate constants decrease by an order of magnitude as the H-atoms become more sterically hindered.

Furthermore, within the rate constants estimated using methoxyl radicals that are shown in Table 3-9, the same independence of rate constant at the primary position is observed, but there is no longer the same decrease at the secondary positions when moving from the least hindered to the most hindered model compounds. With the *t*-butoxyl radical, an order of magnitude decrease between compounds was found. Here, with methoxyl the same trend is not present, what is

observed is a decrease in rate moving from PEN to DMP, but then an increase between DMP and TMP. In this case, the enthalpic effects are overpowering the weaker entropic effects presented by the methoxy radical initiator.

When comparing the overall reactivities of the model compounds found in Table 3-10, it can be seen that even though there is an increase in the number of available H-atoms for abstraction when substituting one secondary carbon hydrogen bond with a methyl group and creating a tertiary center, the overall reactivity of the compounds decreases. This agrees with literature precedent, where Dokolas et al.<sup>19</sup> compared the overall yields of 3-methylpentane with DMP in his radical trapping experiment. They found DMP to have a 5.6% move overall yield than 3-methylpentane, a less sterically hindered model compound.

Examining the methoxyl entropic parameters of the CBS-QB3 results in Table 3-4, the entropic barrier to activation at the secondary position is the essentially the same between DMP and TMP (0.3 cal/molK), but the enthalpic barrier (found in Table 3-3) differs by 0.6 kcal/mol. If this is compared to the *t*-butoxyl case, there is an entropic difference of 1.0 kcal/mol and an enthalpic difference of 0.4 kcal/mol between DMP and TMP. This entropic barrier at room temperature is twice as large as the enthalpic barrier. As a rough estimate using the barriers calculated at room temperature, at 400 K (~127 °C) this entropic difference will account for ca. 1.3 kcal/mol, now more than 3 times larger than the 0.4 kcal/mol barrier imposed by the enthalpy.

To date, only two computational studies have been carried out in this area. In 2007, Bertin<sup>34</sup> carried out a DFT study using the B3LYP functional and a large basis set to estimate the reactivity of 2,4,6-trimethylheptane towards hydrogen abstraction by *t*-butoxyl radicals. They focused their modeling attempts towards reproducing EPR data by Niki et al.<sup>14</sup> using DFT methods that had not been used at that point to model hydrogen abstractions. Up to this point, H-atom abstractions were traditionally modeled using *ab initio* methods. Additionally to employing DFT, they also used a solvent surface approach to assess the accessibility of different hydrogen

locations on the molecule. The study also included mathematical modeling using Predici to simulate the decay of the produced radicals in their EPR data.

Bertin's results were inconclusive.<sup>34</sup> They examined the reaction in a variety of different ways and were not able to reproduce the experimental results until they modeled the system using Predici. However, some of the rate constants were chosen almost arbitrarily with no other analysis or verification for them. However, they do state that these constants "...must be used with high caution". They noted that modeling the system correctly requires accurate modeling of the enthalpic as well as steric contributions to the reaction. As is seen here, DFT does not adequately treat this system and the experimental product ratios that they determined were 94% primary abstraction and 6% tertiary abstraction with none occurring at the secondary position. Bertin also compared their results to the observed product ratios determined via EPR by Camara<sup>13</sup> who found that the bulk of the radicals present (75%) were located at the tertiary positions in 2,4,6-trimethylheptane.

This study began from the structures previously optimized by Bertin as a starting point for our calculations, and found that there was a transition state for abstraction from the secondary position located 2.5 kcal/mol lower in energy. Even so, in our case with DMP and DFT, there is only a 5% abstraction rate at the secondary position and again abstraction is dominated by the primary position. It is not until using MP2 and CBS-QB3 that ratios which approach the experimental values are calculated, with abstraction now dominated at the tertiary positions. Dokolas,<sup>19</sup> in neat DMP, determined relative yields of 23.9% primary, 9.1% secondary, and 67.3% tertiary. Herein is estimated a product distribution of 11% primary, 24% secondary, and 65% tertiary from gas phase calculations. If one considers the added steric effects that will play a role in the condensed phase, abstraction at the secondary position will become more difficult and primary abstractions will become more favoured. This is supported by the drastic change in

selectivity found in our calculations when comparing *t*-butoxyl to the much smaller methoxyl radical initiator.

Moving to the higher level of theory does help to improve the results, but it must be stressed again that the calculations are carried out in the gas phase, and any solvation effects on the radical will play a role in increased the entropic strain in the transition states and reduce the abstraction that occurs at the secondary and tertiary position. This undoubtedly will play a role since moving to methoxy radicals from *t*-butoxyl lowered the entropy so much that in DMP in the gas phase, almost all the primary abstraction converts to tertiary.

Camara<sup>13</sup> also carried out a DFT study on DMP, complementing EPR experiments that found no traces of secondary abstraction from the secondary position. With DFT the authors were unable to quantitatively explain the lack of abstraction at the secondary position. It is clear now from looking at the results presented that the DFT methods used here, and in previous papers, do not accurately describe this system. It is not until moving to high level *ab initio* calculations or composite methods such as CBS-QB3 that accurate results are achieved.

CBS-QB3 begins by calculating the geometry and thermodynamic corrections to the energy using DFT and the B3LYP functional, the same that was used in the DFT methods here. However, that is where the similarities end. The electronic energy is then calculated at the gold standard CCSD(T) level and the value extrapolated to an infinite basis set size using MP2 and MP4 based calculations, with the energy contribution of the spin contamination corrected for. The zero point energy correction is determined from the frequencies obtained in the DFT calculation, scaled by a factor of 0.91844. The final energy also contains an empirical correction which minimizes the error in electron overlap interference.<sup>42</sup> Put together, this provides a very accurate value for the electronic energy which the DFT thermodynamic corrections are applied to create the enthalpic parameters. The entropic parameters are still calculated using DFT and originate from the vibrational modes of the molecule, but it is the improved treatment of dispersion



interactions by the CCSD(T) and infinite basis set extrapolation of the singlepoint energy calculation with empirical corrections that properly treats the enthalpic barriers, produces the correct trends, and more accurately predicts H-atom abstraction rate constants.

### 3.4 Methods of calculations

All calculations below were performed using either the Gaussian 03<sup>48</sup> or Gaussian 09<sup>49</sup> programs. DFT calculations were carried out at the UB3LYP level, with all stationary points optimized using the 6-31G(d,p) basis set. Singlepoint calculations were then performed on the optimized stationary points at the 6-311++G(3df,3pd) level. MP2 calculations were similarly performed using the same basis sets and methodology as for the DFT calculations. Vibrational frequency calculations were performed to characterize each stationary point as a minimum (no imaginary frequencies) or saddle point (one imaginary frequency) on the potential energy surface. Frequencies were scaled by a factor of 0.9804 for DFT results, and 0.9646 for MP2.<sup>25</sup> The CBS-QB3 calculations were performed without modification. The spin contaminations of all the stationary points were reasonable, with the maximum  $\langle s^2 \rangle$  values of 0.757, 0.785, and 0.797 for the DFT, MP2 and CBS-QB3 CCSD(T) calculations respectively. All frequency calculations were carried out at 1 atm and 298.15 K.

## Chapter 4

# Conclusions: Combining Experimentally Obtained Data with Quantum Chemical Calculations

### 4.1 Conclusions

In this investigation, experimental and computational studies of three polymer model compounds were carried out in order to determine the factors that govern the selectivity with which they react with *t*-butoxyl radicals by H-atom abstraction. The results of radical trapping experiments utilizing the UV-absorbing nitroxyl TMIO enabled the experimental determination of product distributions and corresponding relative reactivities of each C-H in the model compounds. A drastic reduction in the rate of H-atom abstraction was evident at the secondary abstraction position as they become more congested, i.e., on moving from PEN to DMP and TMP.

By using a range of theoretical methods it was possible to assess the validity of each in this system. It was found that despite their essentially universal use to address this problem, DFT methodologies do not adequately model the dispersive interactions about the sterically hindered secondary reaction site. It was found that the *ab initio* MP2 method and the composite CBS-QB3 method more accurately treat the enthalpic and entropic effects, and as a result compare more favourably to experimental values. Both MP2 and CBS-QB3 provided similar trends. Therefore, if the computational power is not available, these reactions should be examined with at least the MP2 level of theory. It was found that the balance between the enthalpic advantages created by radical stabilization at more substituted carbon centers and the entropic disadvantages afforded by adjacent groups to the abstraction site controlled the regioselectivity.

Through these computational analyses, evidence that entropic effects play a large role in the reactivity of these model compounds towards H-atom abstraction has been found. The highest-level calculations carried out show that the reactivity of the secondary position in TMP is almost 80-fold lower than secondary sites in PEN when *t*-butoxyl is used at the radical initiator, supporting the experimental results. The reactivities of the primary positions were found to be relatively compound-independent, and a 65-fold decrease in reactivity at the secondary position in TMP compared to PEN was found.

When moving from the relatively bulky *t*-butoxyl radical to the smaller methoxy radical, drastic changes were observed in the selectivity of these H-atom transfer reactions. The *t*-butoxyl initiator showed an order of magnitude decrease in abstraction rate when moving to subsequent, more sterically hindered, compounds. By contrast, the less bulky methoxyl radical did not share this trend, and the rate of abstraction was unaffected by the bulkiness on the compound. The loss in reactivity calculated at the secondary positions with *t*-butoxyl outweighed added reactivity of tertiary and primary groups resulting in an overall loss in abstraction reactivity in DMP and TMP over PEN.

## 4.2 Future work

To compare the estimated overall reactivities, a competition experiment can be conducted where two model compounds are present during H-atom abstraction and radical trapping. Differences in overall reactivity can then be determined by comparing the relative yields of the alkoxyamines derived from the different model compounds. High temperature radical trapping experiments can also be carried out at temperatures more relevant to industrial graft copolymerization processes. Computationally, there also exist dispersion corrected DFT methods which can be investigated and may provide more accurate results at sufficiently lower computational cost than MP2 and CBS-QB3.

## References

- <sup>1</sup> K. E. Russell; *Prog. Polym. Sci.* **2002**, 27, 1007.
- <sup>2</sup> G. Xu, S. Lin; *J. Macromol. Sci, Rev. Macromol. Chem. Phys.* **1994**, 34, 555.
- <sup>3</sup> S. Torikai, M. Kato, E. Mukoyama; *Kobunshi Kagaku* **1964**, 21, 132.
- <sup>4</sup> Asahi Chemical Ind. Co.; *Fr. Pat.* **1968**, 1,533,691.
- <sup>5</sup> a) Toyo Ink Mfg. Co.; *Japanese Patent* **1981**, 81 62,147 b) Toyo Ink Mfg. Co.; *Japanese Patent*, **1981**, 81 93,789 c) Mitsubishi Petrochemical Co.; *Japanese Patent*, **1984**, 59 198,135 d) Mitsubishi Petrochemical Co.; *Japanese Patent*, **1984**, 59 198,136.
- <sup>6</sup> W. Reints, D. A. Pratt, H. Korth, P. Mulder; *J. Phys. Chem. A.* **2000**, 104, 10713.
- <sup>7</sup> F. Minisci, R. Galli; *Tet. Lett*, **1962**, 12, 533.
- <sup>8</sup> E. Sato, P.B. Zetterlund, B. Yamada, W.K. Busfield, I. D. Jenkins; *Macromol. Chem. Phys.* **2003**, 15, 1882.
- <sup>9</sup> H. Pauy, R. D. Small, Jr., and J. C. Scaiano; *J. Am. Chem. Soc.* **1978**, 14, 4520.
- <sup>10</sup> C. Walling; *Pure. Appl. Chem.* **1967**, 15, 69
- <sup>11</sup> D. V. Avila, C. E. Brown, K. U. Ingold, J. Lusztyk; *J. Am. Chem. Soc.* **1993**, 115, 466.
- <sup>12</sup> E. Niki, Y. Kamiya; *J. Org. Chem.* **1973**, 38, 1403.
- <sup>13</sup> S. Camara, B.C. Gilbert, R.J. Meier, M. van Duin, A.C. Whitwood; *Org. Biomol. Chem.* **2003**, 1, 1181.
- <sup>14</sup> E. Niki, N. Ohto, T. Kanauchi, Y. Kamiya; *Eur. Polym. J.* **1980**, 16, 559.
- <sup>15</sup> J. J. B. Chenier, S. B. Tong,, J. A. Howard. J. A; *Can. J. Chem.*, **1978**, 56, 3047.
- <sup>16</sup> D. G. Hendry. T. Mill. L. Piszkiwicz; *J. Phys. Chem. Ref. Data.* **1974**, 3, 937.
- <sup>17</sup> C. Walling. B. B. Jacknow; *J. Am. Chem. Soc.* **1960**, 82, 6108.
- <sup>18</sup> K. U. Ingold, G. A. DiLabio; *Org. Lett.* **2006**, 8, 5923.

- <sup>19</sup> P. Dokolas, S.M. Loffler, D.H. Solomon; *Aust. J. Chem.* **1998**, 51, 1113.
- <sup>20</sup> P. Dokolas, M.G. Looney, S. Musgrave, S. Poon, D.H. Solomon; *Polymer*. **2000**, 41, 3137.
- <sup>21</sup> E. Rizzardo, D. H. Solomon; *Polym. Bull.* **1979**, 1, 529.
- <sup>22</sup> P. Schmid, K. U. Ingold; *J. Am. Chem. Soc.* **1978**, 100, 2493.
- <sup>23</sup> A. L. J. Beckwith; *J. Chem. Soc.* **1962**, 2248.
- <sup>24</sup> M. Finn, R. Friedline, N. K. Suleman, C. J. Wohl, J. M. Tanko; *J. Am. Chem. Soc.* **2004**, 126, 7578.
- <sup>25</sup> J.B. Foresman, A. Frish, in: *Exploring Chemistry with Electronic Structure Methods*, second ed., Gaussian, Inc., PA, **1996**.
- <sup>26</sup> N. Argaman. G. Makov. Density-functional Theory - an introduction. <http://arxiv.org/abs/physics/9806013v2> [physics.ed-ph]. **1999**.
- <sup>27</sup> M. Born, J. R. Oppenheimer; *Ann. Phys. (Leipzig)* **1927**, 84, 457.
- <sup>28</sup> J. A. Montgomery, M. J. Frisch, J. W. Ochterski, G. A. Petersson; *J. Chem. Phys.* **1999**, 110, 2822.
- <sup>29</sup> B.S. Jursic;. *Int. J. Quantum Chem.* **1997**, 65, 75.
- <sup>30</sup> D. A. Pratt, G. A. DiLabio; *J. Phys. Chem. A.* **2000**, 104, 1938.
- <sup>31</sup> G. A. DiLabio, J. S. Wright; *J. Phys. Chem. A.* **1999**, 103, 1653.
- <sup>32</sup> J.W. Ochterski; *Gaussian*. [http://www.gaussian.com/g\\_whitepap/thermo.htm](http://www.gaussian.com/g_whitepap/thermo.htm). (27/01/10)
- <sup>33</sup> H. Basch, S. Hoz; *J. Phys. Chem. A.* **1997**, 101, 4416.
- <sup>34</sup> D. Bertin, S. Grimaldi, M. Leblanc, et al. *J Mol Struc-Theochem.* **2007**, 811, 255.
- <sup>35</sup> B. Mahiou, G.J. Gleicher; *J. Org. Chem.* **1987**, 52, 1555.
- <sup>36</sup> P.E. Elford, B.P. Roberts; *J. Chem. Soc. Perkin Trans. 2.* **1998**, 6, 1413.

- <sup>37</sup> C. A. Ogle, S. W. Martin, G. D. Mendenhall et al; *J. Org. Chem.* **1983**, 48, 3728.
- <sup>38</sup> P. G. Griffiths, G. Moad, E. Rizzardo; *Aust J. Chem.* **1983**, 36, 397.
- <sup>39</sup> H.C. Beachell, D. L. Beck; *J. Polym. Sci., Part A*, **1965**, 3, 457.
- <sup>40</sup> G. Mendenhall; *Tet Lett.* **1982**, 24, 451.
- <sup>41</sup> P. G. Griffiths, E. Rizzardo, D. H. Solomon; *J. Macromol. Sci., [Part A] Chem.*, **1982**, 17, 45.
- <sup>42</sup> J. A. Montgomery, M. J. Frisch.; *J. Chem. Phys.* **1999**, 110, 2822.
- <sup>43</sup> CRC Handbook of Chemistry and Physics, 90th ed, 2009-2010.  
<http://www.hbcpnetbase.com> (Accessed May 26<sup>th</sup>, 2010).
- <sup>44</sup> E. V. Anslyn, D. A. Dougherty, in: *Modern Physical Organic Chemistry*, University Science Books, VA, **2006**.
- <sup>45</sup> a) W. Kohn, Y. Meir, D. E. Makarov; *Phys. Rev. Lett.* **1998**, 80, 4153. b) Q. Wu, W. J. Yang; *Chem. Phys.* **2002**, 116, 515. c) S. Grimme; *J. Chem. Phys.* **2003**, 118, 9095. d) S. Grimme; *J. Comput. Chem.* **2004**, 25, 1463.
- <sup>46</sup> M. I. Sway; *J. Chem. Soc. Faraday. Trans.* **1991**, 87, 2157.
- <sup>47</sup> S. Li, W. Y. Fan; *Chem. Phys. Let.* **2006**, 427, 276.
- <sup>48</sup> Gaussian 03, Revision C.02, M. J. Frisch, et al. Gaussian, Inc., Wallingford CT, **2004**.
- <sup>49</sup> Gaussian 09, Revision A.02. M. J. Frisch, et al. Gaussian, Inc., Wallingford CT, **2009**.

## Appendix A

### Miscellaneous computational data

**Table A1:** All thermodynamic transition state parameters of the *t*-butoxyl and methoxyl H-atom abstraction as a function of the level of theory at 298.15 K and 1 atm. DFT and MP2 values were calculated using an unrestricted formalism at the UB3LYP/6-311++G(3df,3pd)//UB3LYP/6-31G(d,p) and UMP2/6-311++G(3df,3pd)//UMP2/6-31G(d,p) level.

Compound		PEN			DMP			TMP	
Position		p	s	s'	p	s	t	p	s
<b><i>t</i>-Butoxyl</b>									
DFT	$\Delta H^\ddagger$	7.4	6.7	6.7	8.0	7.9	6.5	8.3	9.7
	$\Delta G^\ddagger$	17.0	17.6	17.6	19.1	19.6	18.7	18.9	21.7
	$\Delta S^\ddagger$	-32.1	-36.7	-36.7	-37.1	-39.2	-41.0	-35.3	-40.1
MP2	$\Delta H^\ddagger$	5.7	3.3	3.3	4.9	2.9	2.1	4.5	3.7
	$\Delta G^\ddagger$	15.9	14.7	14.6	16.0	14.5	14.0	15.5	15.7
	$\Delta S^\ddagger$	-34.4	-38.0	-38.0	-37.2	-39.2	-40.2	-37.0	-40.3
CBS-QB3	$\Delta H^\ddagger$	4.9	1.5	1.5	4.1	2.0	0.7	3.8	2.4
	$\Delta G^\ddagger$	14.6	12.1	12.1	14.8	13.3	12.7	14.6	14.7
	$\Delta S^\ddagger$	-32.5	-35.6	-35.6	-36.0	-37.8	-40.3	-36.3	-41.1
<b>Methoxyl</b>									
DFT	$\Delta H^\ddagger$	7.9	4.9	4.9	7.3	5.1	3.9	7.5	5.4
	$\Delta G^\ddagger$	16.6	14.6	14.6	17.2	15.7	14.7	17.2	16.2
	$\Delta S^\ddagger$	-29.3	-32.7	-32.7	-33.5	-35.7	-36.2	-32.7	-36.2
MP2	$\Delta H^\ddagger$	7.8	5.3	4.8	6.9	4.0	3.2	6.7	3.3
	$\Delta G^\ddagger$	16.4	14.3	14.3	16.7	14.6	13.8	17.1	14.4
	$\Delta S^\ddagger$	-28.7	-30.1	-31.8	-32.9	-35.5	-35.4	-34.9	-37.2
CBS-QB3	$\Delta H^\ddagger$	6.7	3.7	3.7	6.0	2.4	1.7	5.8	1.8
	$\Delta G^\ddagger$	15.7	12.9	12.9	16.2	13.2	12.5	15.6	12.6
	$\Delta S^\ddagger$	-30.1	-31.0	-31.0	-34.3	-36.1	-36.2	-33.1	-36.4

## Product Distributions

### Pentane

$$\%[p] = \frac{k_p}{k_p + 2/3 k_s + 2/6 k_{s'}}$$

$$\%[s] = \frac{k_s}{k_s + 3/2 k_p + 1/2 k_{s'}}$$

$$\%[s'] = \frac{k_{s'}}{k_{s'} + 2k_s + 3k_p}$$

### 2,4-Dimethylpentane

$$\%[p] = \frac{k_p}{k_p + 1/6 k_s + 1/6 k_t}$$

$$\%[s] = \frac{k_s}{k_s + 6k_p + k_t}$$

$$\%[t] = \frac{k_t}{k_t + 6k_p + k_s}$$

### 2,2,4,4-Tetramethylpentane

$$\%[p] = \frac{k_p}{k_p + 1/9 k_s}$$

$$\%[s] = \frac{k_s}{k_s + 9k_p}$$



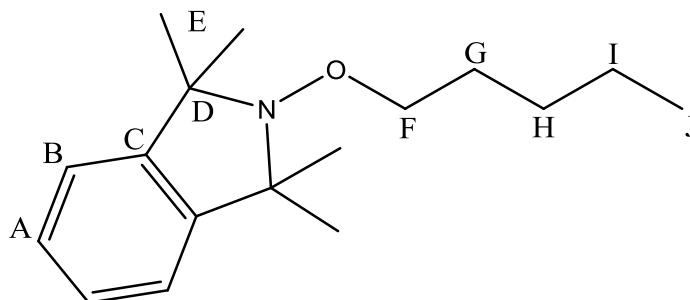
## Appendix B

### Characterization of radically trapped products

#### Pentane derivatives

There are three possible locations for H-atom abstraction from pentane; the primary position, and two secondary positions within one being in the center of the five carbon chain. Unfortunately, the two secondary positions could not be isolated from one another. What follows is the partial characterization of the primary position and of the secondary positions where the ratio of the two isomers is determined by NMR and GC-MS.

#### 1,1,3,3-Tetramethyl-2-(pentyloxy)isoindoline (PEN-p)



**Scheme B1:** Carbon and hydrogen labeling scheme for NMR characterization of the primary trapped radical product of pentane (DMP-p)

The carbon and hydrogen labeling scheme that will be used throughout the NMR characterization for PEN-p are shown in Scheme B1. PEN-p is not symmetrical and the main feature that will distinguish it from the secondary products is the splitting pattern at position F adjacent to the oxygen atom which should be a triplet which integrates for two H-atoms.

### <sup>1</sup>H NMR Peak assignments

The hydrogen NMR of PEN-p can be seen in Figure B1. The two aromatic positions are found at their usual positions, 7.22 and 7.09 ppm. Using these as a reference, the bridging C-O H-atoms at position F are located at 3.91 ppm and produce a triplet with coupling to position G.

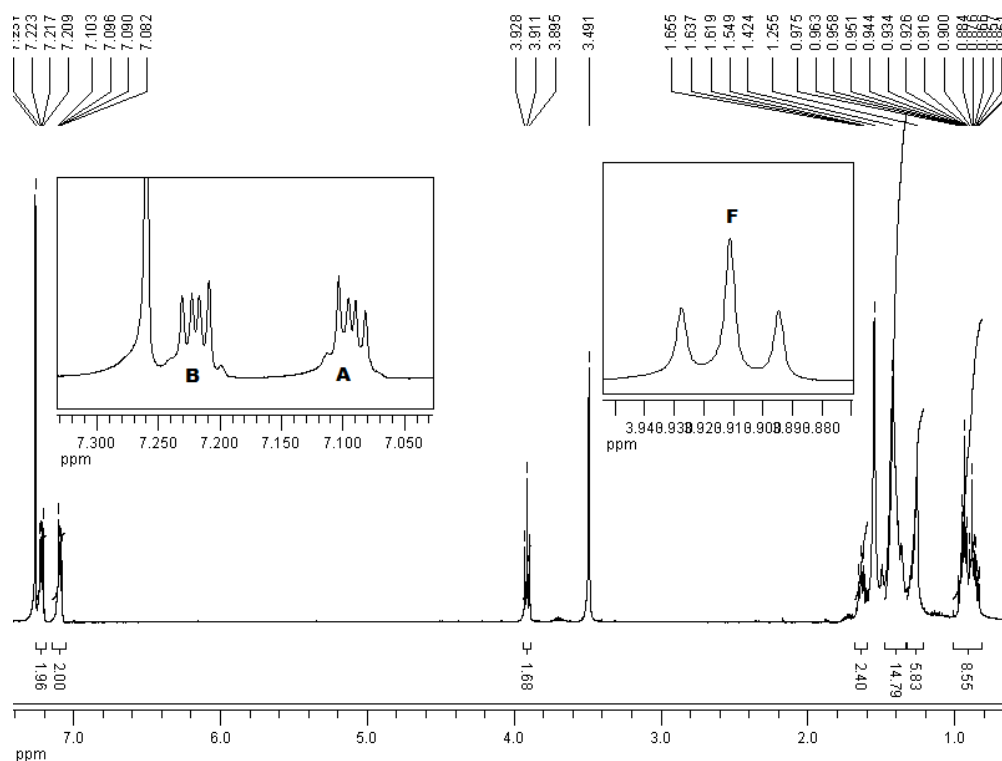


**Figure B1:** <sup>1</sup>H NMR spectrum of PEN-p with peak assignments referenced to chloroform at 7.26 ppm.

Taking a closer look at the aliphatic region of the NMR shown in Figure B2, the secondary position G forms a quintet at 1.64 ppm while the other two secondary positions overlap in the 1.26 ppm region. Unfortunately there is a water impurity at 1.55 ppm along with grease at 1.26 and 0.86 ppm which obscures the integration of H, I, and the primary position J. The methyl groups on the TMIO group form a broad singlet at 1.42 ppm.

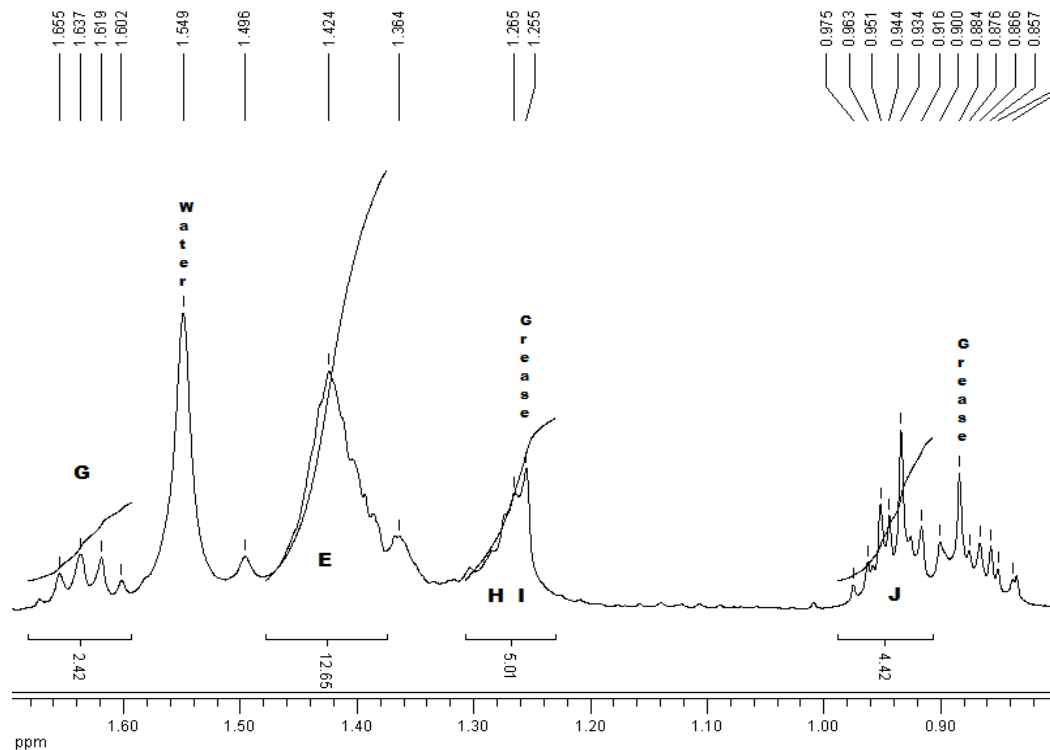


**Figure B2:** Aliphatic region of the  $^1\text{H}$  NMR of PEN-p with peak assignments referenced to chloroform at 7.26 ppm.

### *<sup>13</sup>C NMR peak assignments*

The characterization for the carbon NMR spectra is shown in Figure B3. The aromatic resonances are at their normal positions but the sample was not concentrated enough to obtain a signal for the two quaternary groups on the TMIO portion of the molecule. The bridging carbon at the primary position is found at 99.97 ppm, shifted down-field by the adjacent oxygen atom. The six methyl groups on the TMIO portion appear at 29.05 and 28.68 ppm.

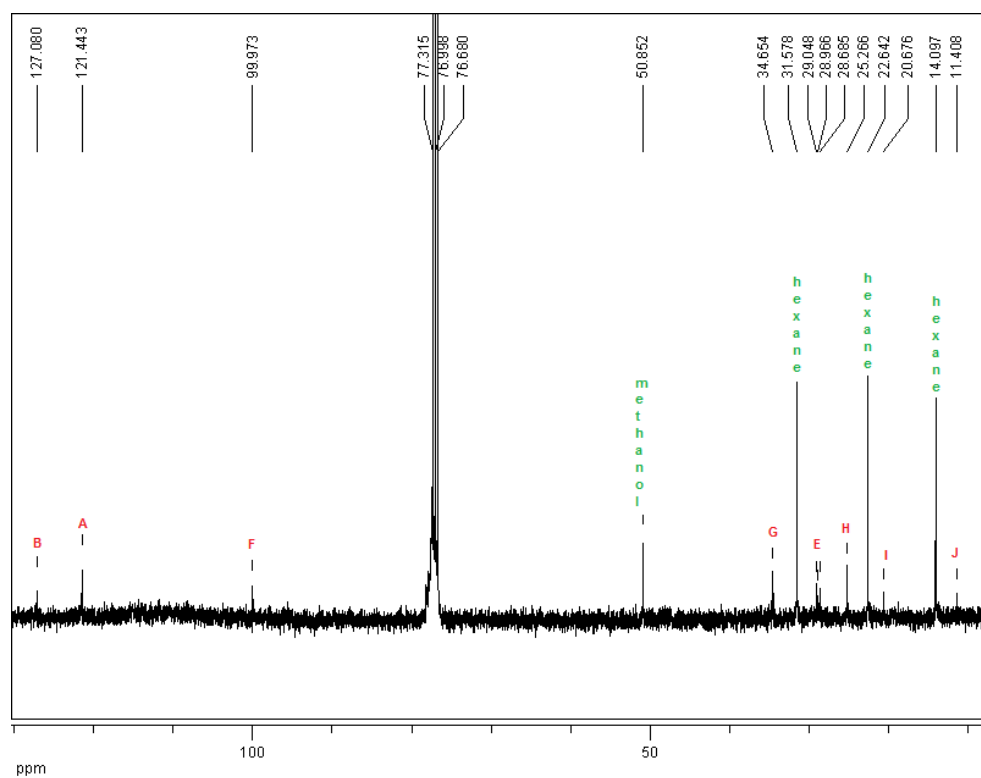


**Figure B3:** <sup>13</sup>C NMR of PEN-p with peak assignments referenced to chloroform at 77.00 ppm

### *Mass spectrometry*

Calculated Mass: 261.2093

Mass Found: 261.2088

ppm: -1.8

### *Retention time*

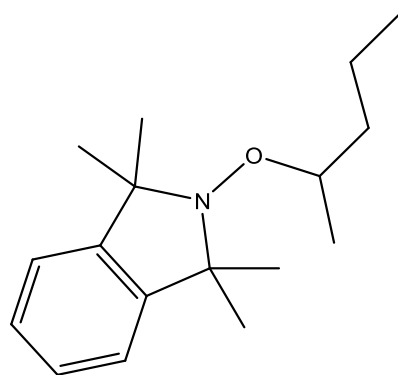
20.7 minutes at 4 mL/min of 85:15 MeOH:H<sub>2</sub>O

### *NMR Peak assignment summary*

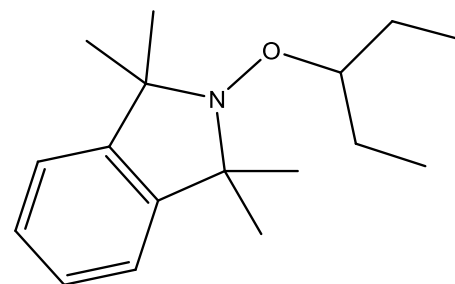
**Table B4-1:** Carbon and hydrogen NMR peak assignments for PEN-p

Position	<sup>13</sup> C Chemical Shift (ppm)	<sup>1</sup> H Chemical Shift (ppm)	Multiplicity	J (Hz)	H Integration
A	121.44	7.09	dd	5.5,3.2	2
B	127.08	7.22	dd	5.5, 3.2	2
C	-	-	-	-	-
D	-	-	-	-	-
E	29.05, 28.68	1.42	br s	-	12
F	99.97	3.91	t	6.6	2
G	34.65	1.64	m	-	2
H	25.27	1.26	m	-	2
I	20.68	1.26	m	-	2
J	11.41	0.98-0.92	m	-	3

### **1,1,3,3-Tetramethyl-2-(pentan-2-yloxy)isoindoline and 1,1,3,3-tetramethyl-2-(pentan-3-yloxy)isoindoline (PEN-s and PEN-s')**



**Scheme B2:** PEN-s carbon and hydrogen labeling system for NMR characterization.



**Scheme B3:** PEN-s' carbon and hydrogen labeling system for NMR characterization.

The two isomers form from trapping at the secondary positions of pentane, PEN-s and PEN-s' shown in Scheme B2 and Scheme B3, could not be isolated from one another by HPLC.

What follows is a partial characterization by NMR to identify that the two compounds are present followed by the determination of their product ratio by NMR and GC-MS.

### *<sup>1</sup>H NMR Peak assignments*

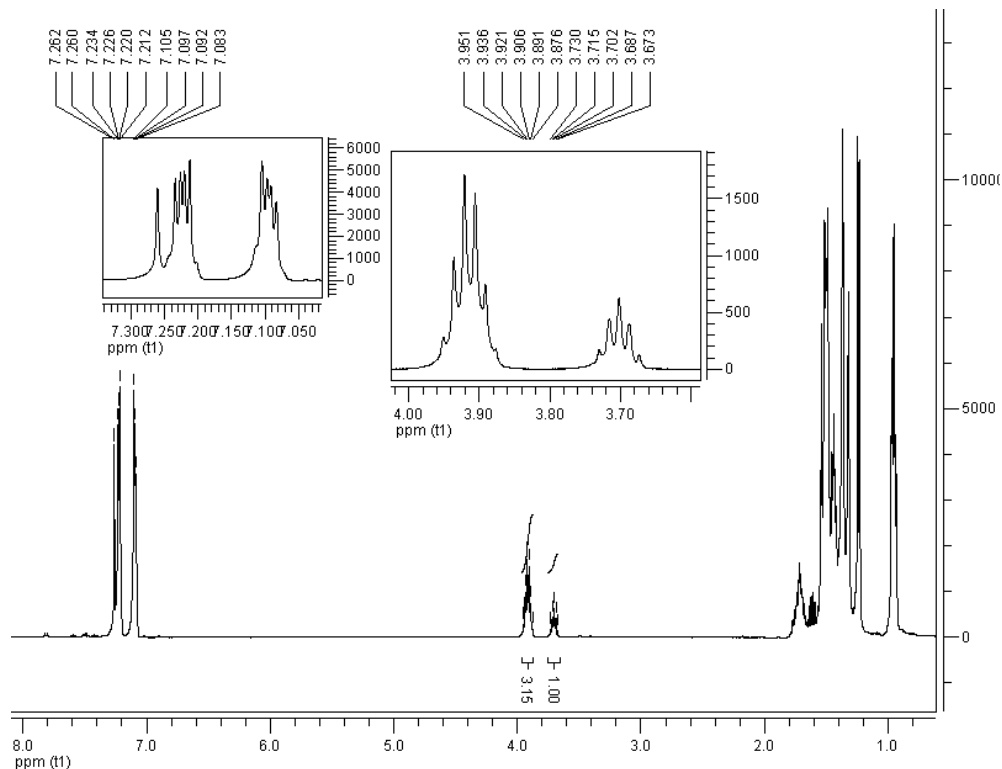


**Figure B4:** <sup>1</sup>H NMR of the mixture of secondary products, PNE-s and PEN-s' referenced to chloroform at 7.26 ppm.

The hydrogen NMR of the mixture of secondary isomers can be found in Figure B4. As per usual, the aromatic H-atoms in the two compounds are found at 7.23 and 7.10 ppm. The two resonances of the bridging carbon at the C-O bond will be used to distinguish between the two isomers. PEN-s' is the symmetrical isomer, where abstraction has occurred at the center secondary position while PEN-s is unsymmetrical. Because of this PEN-s' should have a quintet splitting pattern, coupling to the two adjacent secondary positions. PEN-s should form a sextet with coupling to the primary position and the secondary position at the center of the pentane.

Indeed, both of these are seen with the PEN-s sextet at 3.91 ppm and PEN-s' quintet at 3.70 ppm. The ratio of these two products by NMR 3:1 PEN-s: PEN-s'. From a statistical standpoint, the predicted ratios of these products should be 2:1. To determine the cause of this result, the isomers were injected into a GC-MS for further study.

#### *GC-MS product ratio determination*

The mixture of the two secondary isomers was injected into the GC-MS and the resulting trace is shown in Figure B5.

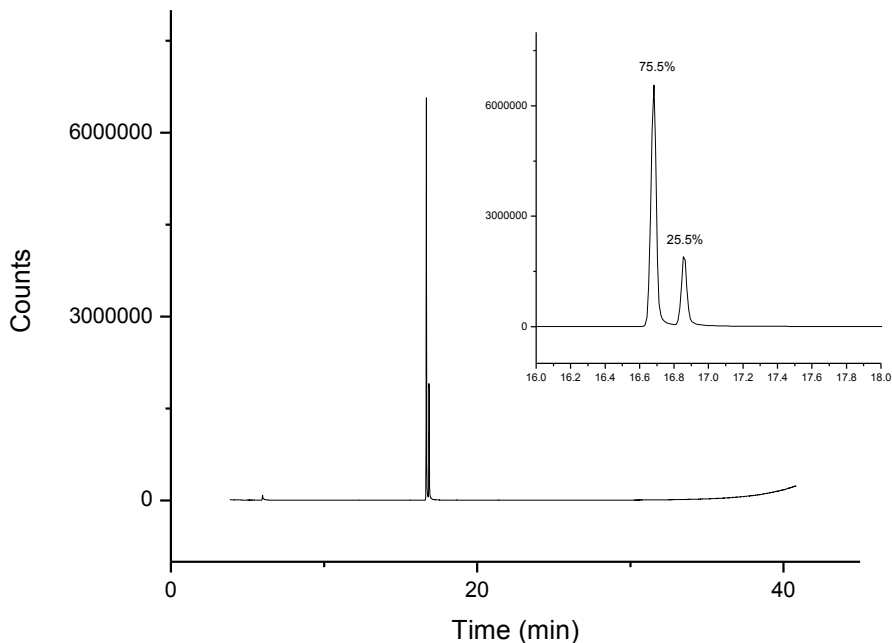


**Figure B5:** GS-MS injection trace of the PEN-s and PEN-s' mixture after HPLC separation

The injection was clean and the only two peaks located at 16.68 and 16.86 minutes were assigned to PEN-s and PEN-s' respectively after inspecting the MS spectra. The area integrations

are shown on Figure B5, and in agreement with the NMR analysis, a 3:1 ratio for PEN-s:PEN-s'. To ensure that the observed product ratio was not caused by error during the HPLC separation the crude mixture was injected on the GC-MS. The resultant trace can be found in Figure B6. Three peaks are shown in the inset of Figure B6, the first two correspond to PEN-s and PEN-s' and share the same residence times as the separated products.

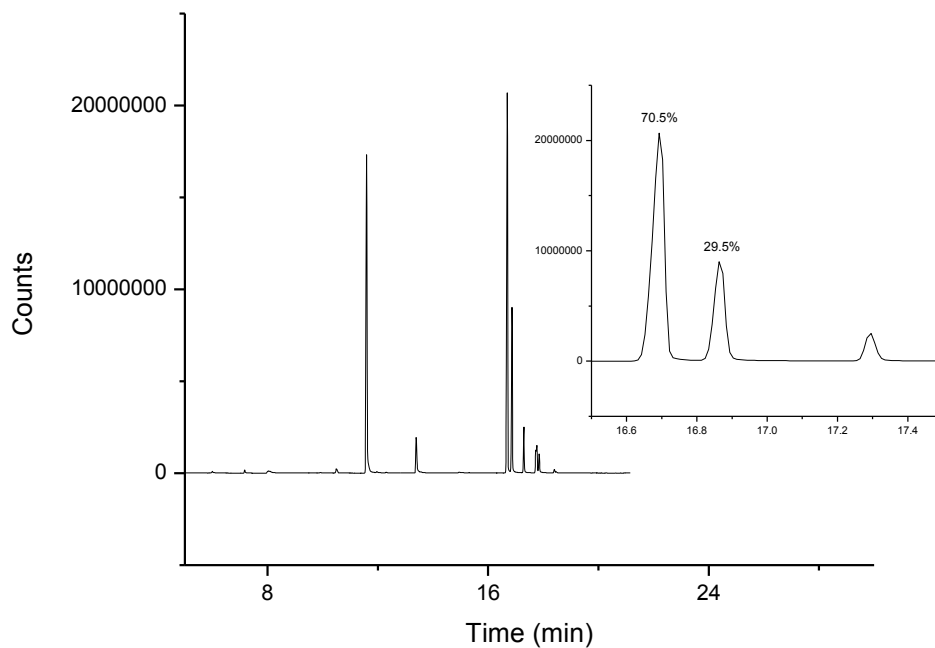


**Figure B6:** Crude GC-MS injection of the PEN radical trapping experiment.



The third peak corresponds to the primary trapped radical product, PEN-s, the isolated GC-MS trace of which can be found in Figure B7 and has a residence time of 7.30 minutes. The product ratio of the two secondary isomers in the crude sample is much closer to the expected with a value of 2.4:1 PEN-s:PEN-s'.

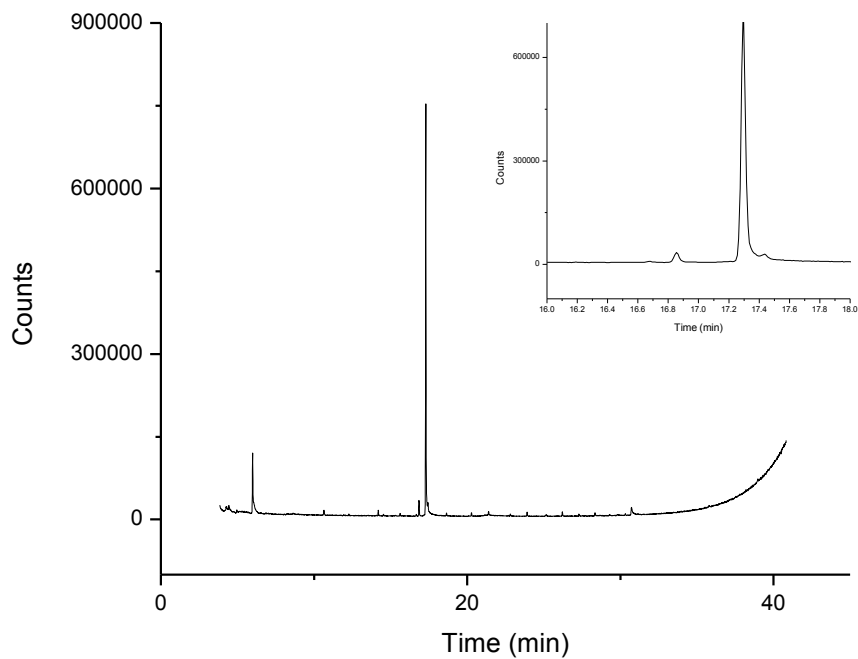


**Figure B7:** GS-MS injection trace of PEN-p after HPLC separation

### *HPLC separation analysis*

To explain the difference in ratios between the separated and crude products, a 10  $\mu\text{L}$  injection of the crude pentane mixture was passed through the HPLC. The resultant trace can be seen in Figure B8. The first peak shown in the inset is the primary product, PEN-p, while the second peak is the mixture of PEN-s and PEN-s'.

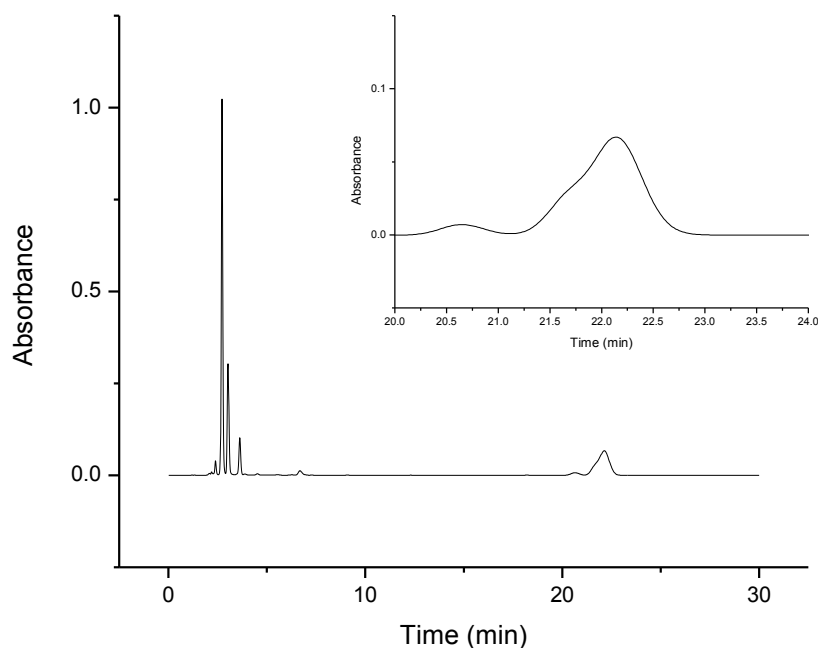


**Figure B8:** 10  $\mu\text{L}$  HPLC injection in 85:15 MeOH:H<sub>2</sub>O of the crude pentane radical trapping reaction mixture

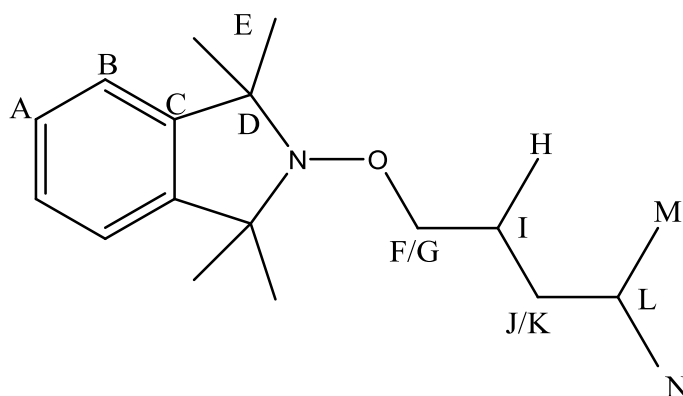
Inspecting the second peak one can see that there are two products coeluting with one another. Preparatory separation was carried out with the aid of a Waters fractionating device which was set to collect a sample every 30 seconds and injection volumes were increased, up to

120  $\mu\text{L}$  if the peak resolution could still be maintained. Usually there would be some overlap between the primary and secondary peaks and that overlap section would be discarded to maintain the purity of the separations. It appears that when the overlap was discarded, a portion of the smaller and faster elution time of the two coeluting peaks, undoubtedly PEN-s', would be discarded. After work up and NMR analysis this discarding artificially increased the product ratio of PEN-s: PEN-s' in the isolated sample.

## 2,4-Dimethylpentane derivatives

The following three compounds have been previously characterized by Dokolas,<sup>19</sup> regardless, their characterization is shown below.

### 2-(2,4-Dimethylpentyl-1,3,3-tetramethylisoindole) (DMP-p)



**Scheme B4:** Carbon and hydrogen labeling convention for NMR characterization of the primary trapped radical product of 2,4-dimethylpentane (DMP-p).

In Scheme B4 the carbon and hydrogen labeling convention is presented that will be used throughout the spectral assignment of DMP-p. There are several features of DMP-p that should

be noted. The tertiary carbon center I, closest to the TMIO adduct is a stereocenter, and as such the H-atoms on the alkoxy carbon center and the secondary position in the center of the molecule are diastereotopic and each hydrogen should have a unique signature in the  $^1\text{H}$  NMR spectrum.

### *$^1\text{H}$ NMR Peak assignments*

The  $^1\text{H}$  NMR spectra for the isolated DMP-p product is presented in Figure B9. Within there are two insets, the first on the left showing the four aromatic H-atoms which are a distinctive signal found in all the trapped products integrating for two H-atoms each at 7.2 and 7.1 ppm.

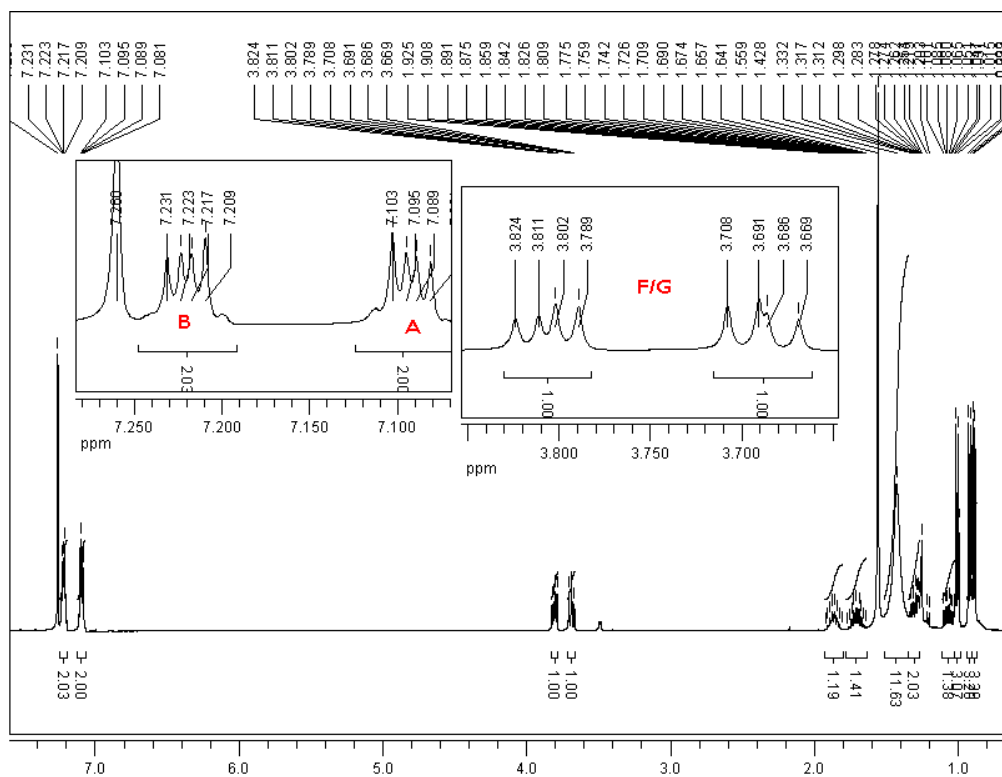


**Figure B9:**  $^1\text{H}$  NMR spectra of DMP-p with peak assignments referenced to chloroform at 7.26 ppm.

The second inset on the right presents the two diastereotopic H-atoms on the primary position of DMP, adjacent to the oxygen atom. They each form a doublet of doublets caused by

geminal  $J^2$  coupling and  $J^3$  coupling to the tertiary hydrogen, I, and are shifted down-field by the adjacent oxygen atom.

A closer look at the aliphatic region is shown in Figure B10. The two tertiary positions are present at 1.88 and 1.71 ppm for positions I and L, respectively. I appears as an octet while L as a nontet. The two secondary H-atoms appear as a doublet of doublet of doublets while the three terminal methyl groups on the DMP portion, H, M, and N, form doublets while the four methyl groups on the TMIO appear as a broad singlet.

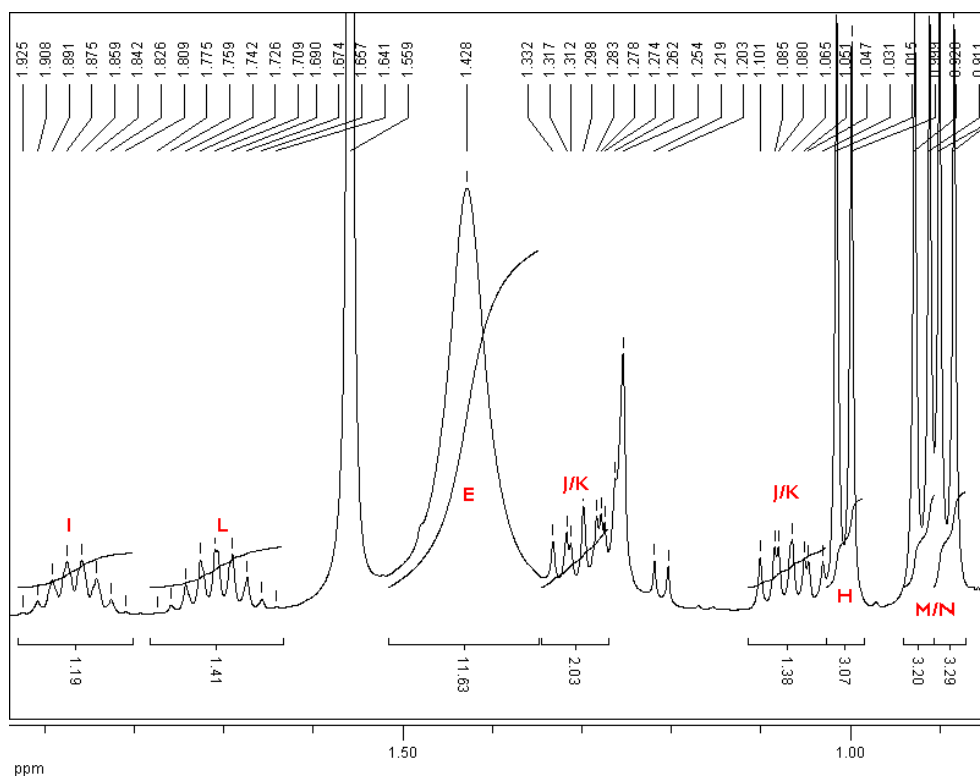


**Figure B10:** Aliphatic region of the  $^1\text{H}$  NMR of DMP-p with peak assignments referenced to chloroform at 7.26 ppm.

There are two impurity peaks present in the spectra that could not be removed and interfere with integration: a water resonance at 1.56 ppm and a hexane peak at 1.26 ppm.

To ensure the peak assignments were correct, a COSY 2D NMR was obtained of the sample and assignments confirmed by cross peak correlation. The COSY spectrum of the aliphatic region is presented in Figure B11.

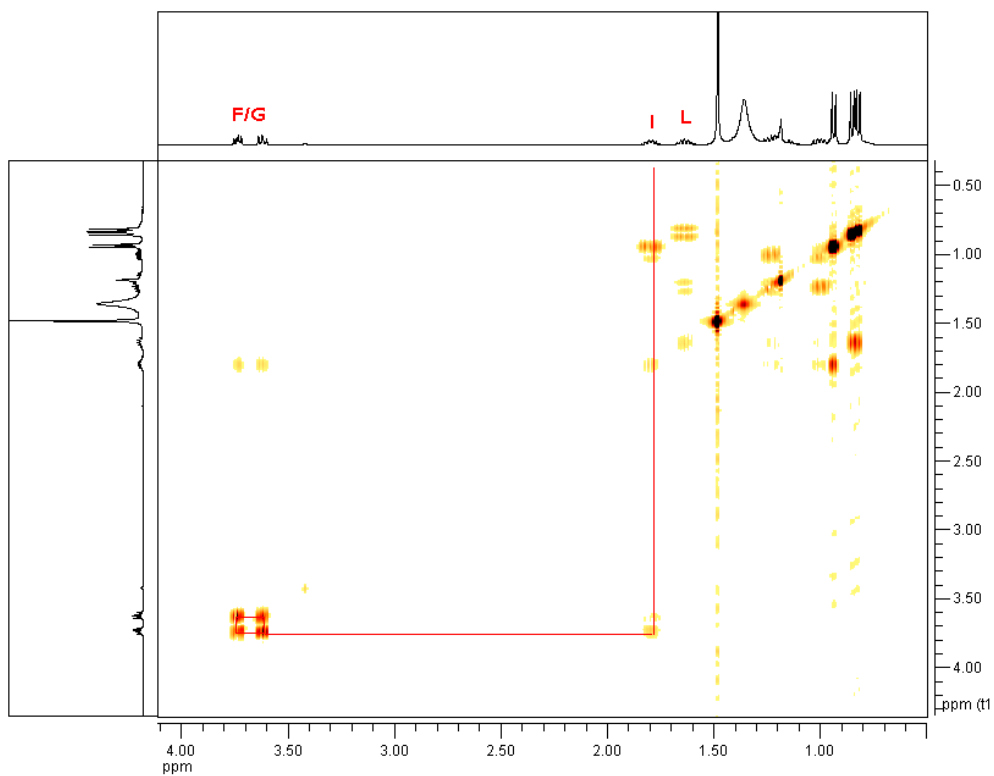


**Figure B11:** COSY 2D NMR of DMP-p from 4.00 to 0.00 ppm with correlation assignments.

From Figure B11 it is apparent that the two H-atoms at the primary position adjacent to the C-O bond couple to one another due to the adjacent stereocenter and to hydrogen I only.

Using hydrogen I as a starting point in Figure B12 (a closer look at the cross correlation of the aliphatic region) it can be seen that it is the sole group coupling to the primary H-atoms at H. Starting again from I, but now moving to the right there is coupling to J and K, the two secondary H-atoms. It is apparent that J and K couple to L, the second tertiary center, which couples to the last two primary centers M and N.

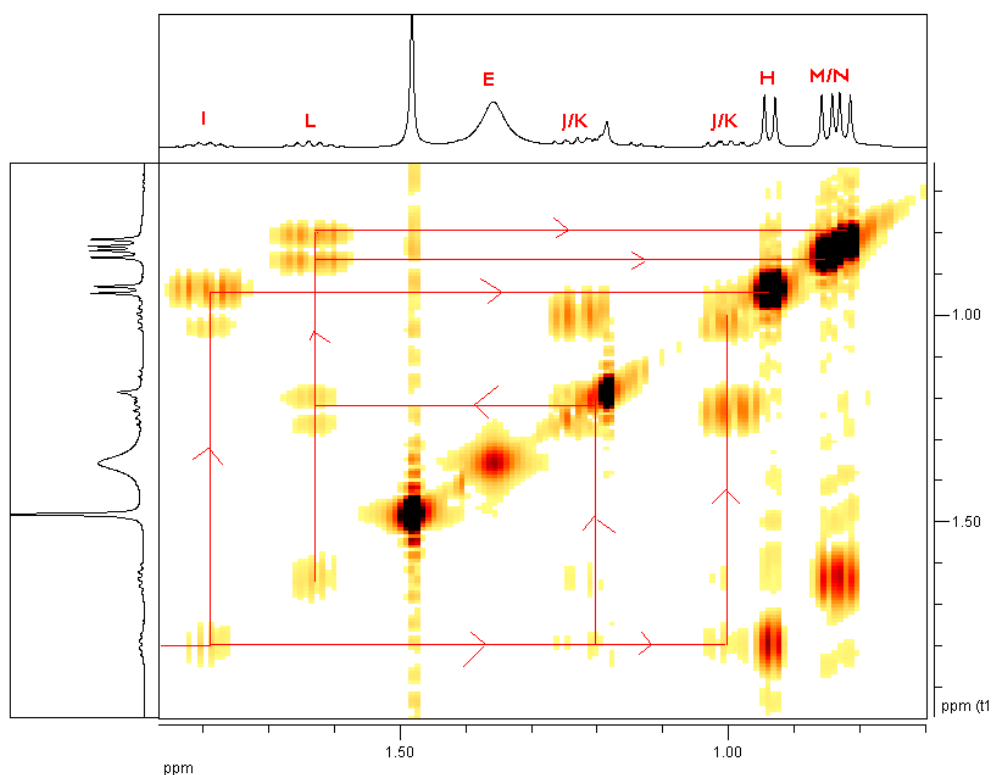


**Figure B12:** Aliphatic region of the 2D COSY NMR of DMP-p from 2.00 to 0.50 ppm with correlation assignments.

### <sup>13</sup>C NMR Peak assignments

The full carbon NMR can be seen in Figure B13.

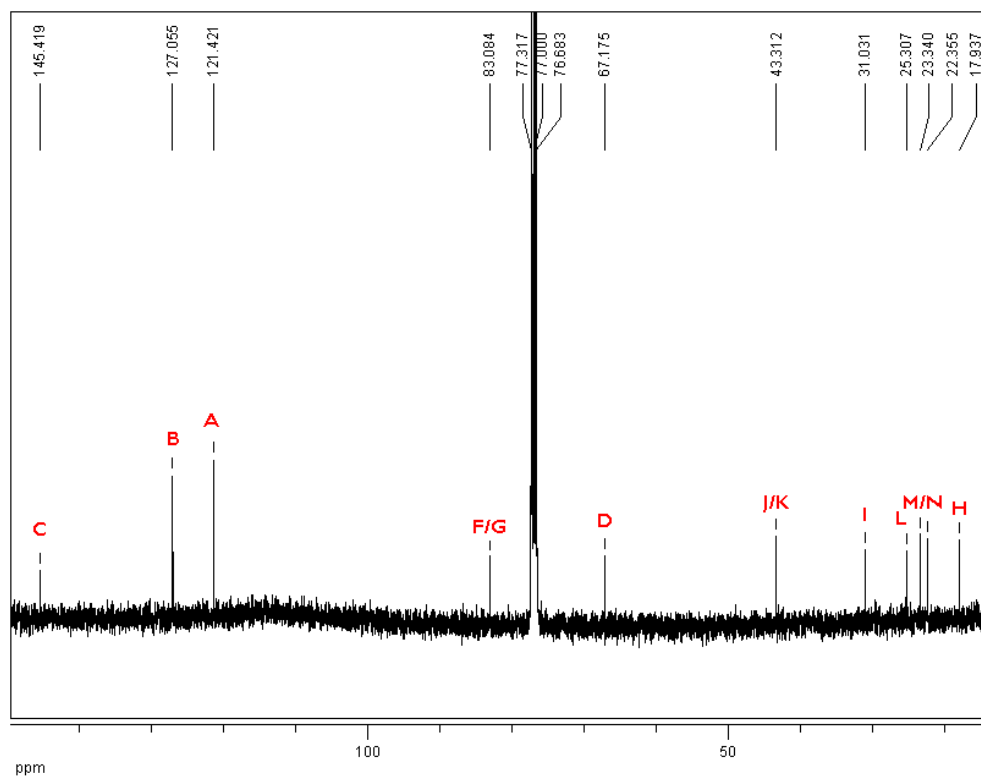


**Figure B13:** <sup>13</sup>C NMR of DMP-p with peak assignments referenced to chloroform at 77.00 ppm.

No resonance could be located for the methyl groups on the TMIO group. Dokolas references these to 29-30.5 ppm.<sup>19</sup> To help locate the methyl groups on the TMIO moiety, HSQC 2D NMR was carried out.



The HSQC can be seen below in Figure B14. While it does appear that the HSQC finds coupling in that region, no peak can be found in the carbon NMR.

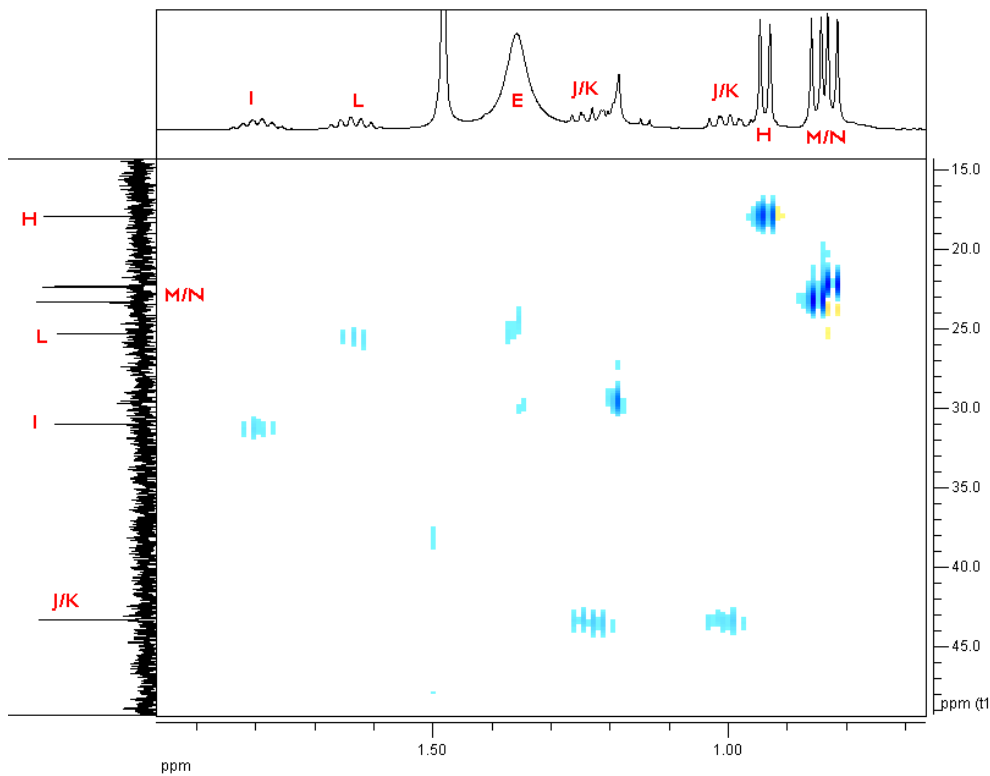


**Figure B14:** Aliphatic region of the HSQC 2D NMR of DMP-p with correlation assignments.

***Mass spectrometry***

Calculated Mass: 289.2406

Mass Found: 289.2412

ppm: 2.2

***Retention time***

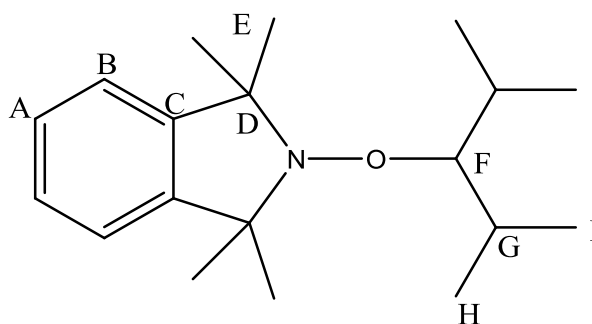
35.3 minutes at 4 mL/min of 85:15 MeOH:H<sub>2</sub>O

### NMR peak assignment summary

**Table B2:** Carbon and hydrogen NMR peak assignments for DMP-p.

Position	<sup>13</sup> C Chemical Shift (ppm)	<sup>1</sup> H Chemical Shift (ppm)	Multiplicity	J (Hz)	H Integration
A	121.42	7.09	dd	5.5,3.2	2
B	127.06	7.22	dd	5.5, 3.2	2
C	145.42	-	-	-	-
D	67.18	-	-	-	-
E	-	1.43	br s	-	12
F	83.08	3.81	dd	8.7, 5.1	1
G	83.08	3.69	dd	8.7, 6.9	1
H	17.94	1.01	dd	6.7	3
I	31.03	1.88	m	-	1
J/K	43.31	1.05-1.33	m	-	2
L	25.31	1.71	m	-	1
M	23.34	0.92	d	6.6	3
N	22.36	0.89	d	6.6	3

### 2-(2,4-Dimethylpentan-3-yloxy)-1,1,3,3-tetramethylisoindoline (DMP-s)



**Scheme B4-5:** Carbon and hydrogen labeling convention for NMR characterization of the secondary trapped radical product of 2,4-dimethylpentane (DMP-s).

In Scheme B4-5 the carbon and hydrogen labeling convention is presented that will be used throughout the spectral assignment of DMP-s. There are several features of DMP-s that should be noted. There are no stereocenters in this compound and is symmetric about the

secondary position on the DMP moiety. In theory, both tertiary centers, G, should be equivalent as well as the methyl groups I and H.

### *<sup>1</sup>H NMR Peak assignments*

The full hydrogen spectrum is presented in Figure B15. The characteristic aromatic protons on the TMIO moiety are presented in the left inset. These peaks confirm that trapping has occurred as they do not resolve when TMIO is a nitroxyl. Also presented is the tertiary center G, which is adjacent to the trapped secondary position. It integrates for two H-atoms which confirms the symmetry of the system.

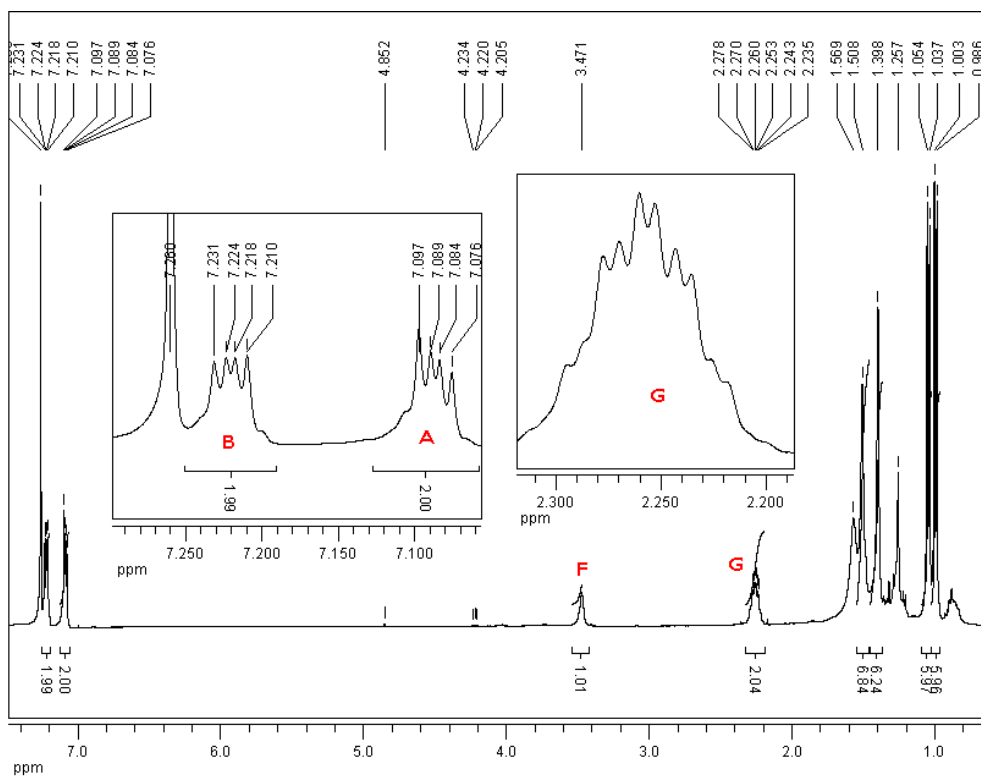


**Figure B15:** <sup>1</sup>H NMR of DMP-s with peak assignments referenced to chloroform at 7.26 ppm.

Taking a closer look at the aliphatic region shown in Figure B16, the methyl groups on the TMIO portion of the molecule appear as two broad singlets, integrating for six H-atoms each. The more down-field of the peaks is slightly obscured by a water impurity. The two methyl groups on the DMP portion appear as two doublets, each integrating for six. There appears to be C2 symmetry in the molecule, groups on the TMIO and DMP portion being unique.

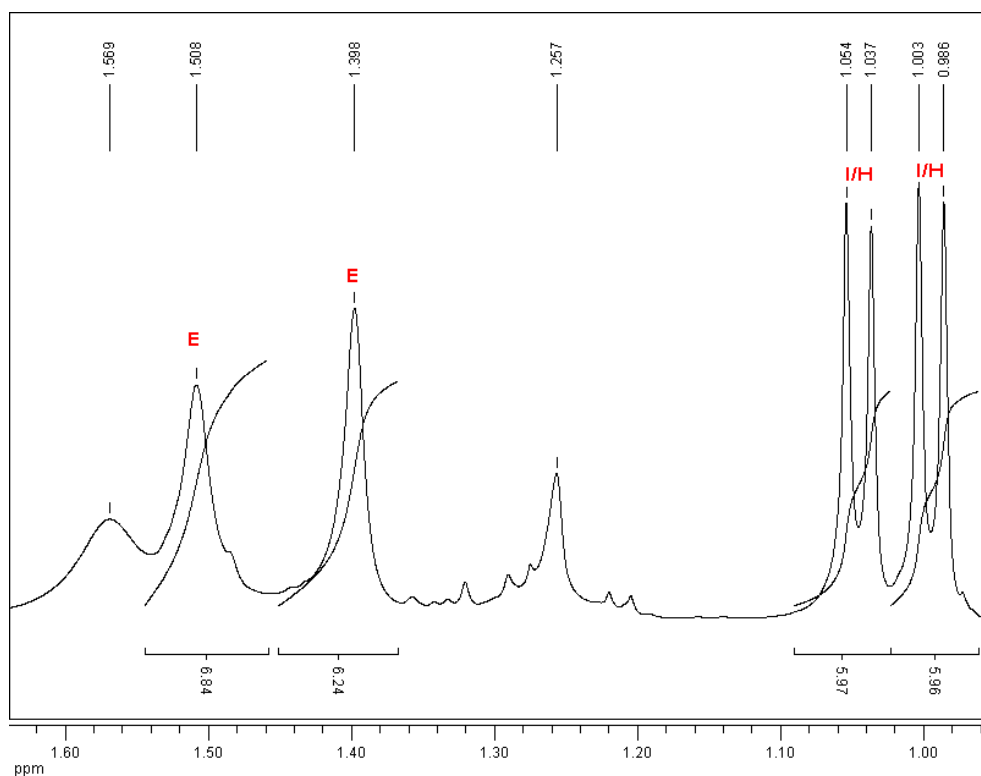


**Figure B16:** Aliphatic region of the  $^1\text{H}$  NMR of DMP-s with peak assignments referenced to chloroform at 7.26 ppm.

A COSY NMR was also obtained for DMP-s. The cross correlation confirms the peak assignments. The COSY can be seen below in Figure B17.

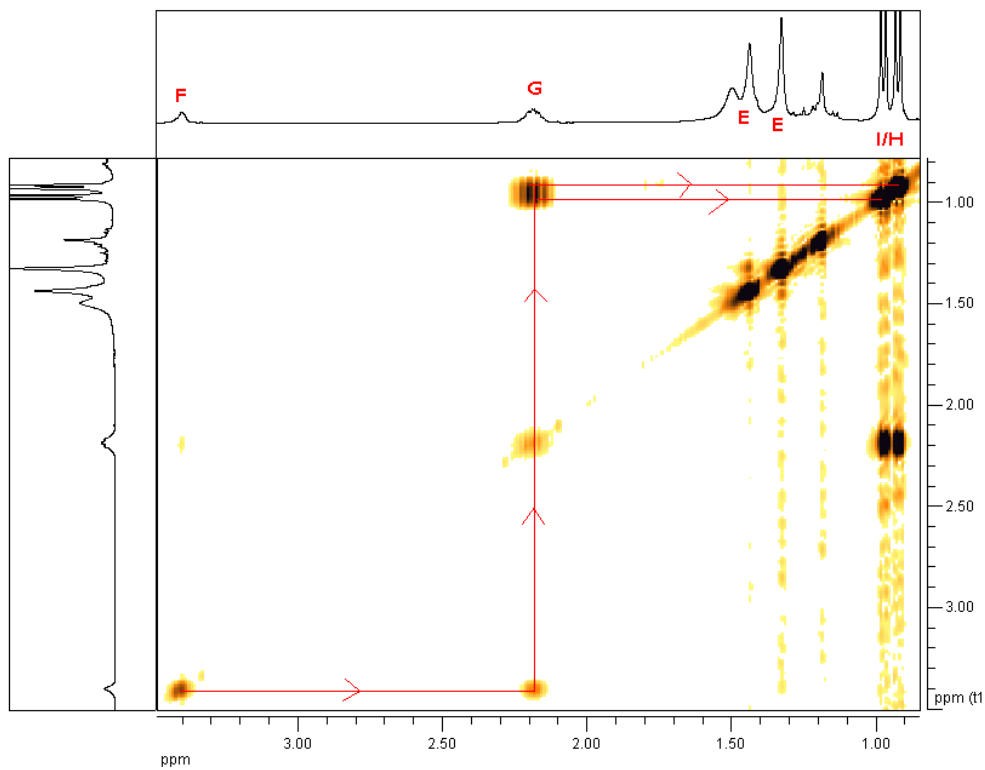


**Figure B17:** COSY 2D NMR of DMP-p from 4.00 to 0.85 ppm with correlation assignments.

### <sup>13</sup>C NMR Peak assignments

The <sup>13</sup>C NMR spectra of DMP-s, which is presented in Figure B18, has several features of note. The aromatic carbons are in their usual positions, however there is no resonance for the secondary carbon bonded to the TMIO group. The aliphatic region is also cluttered with two small peaks assigned to the methyl groups on the radical trap.

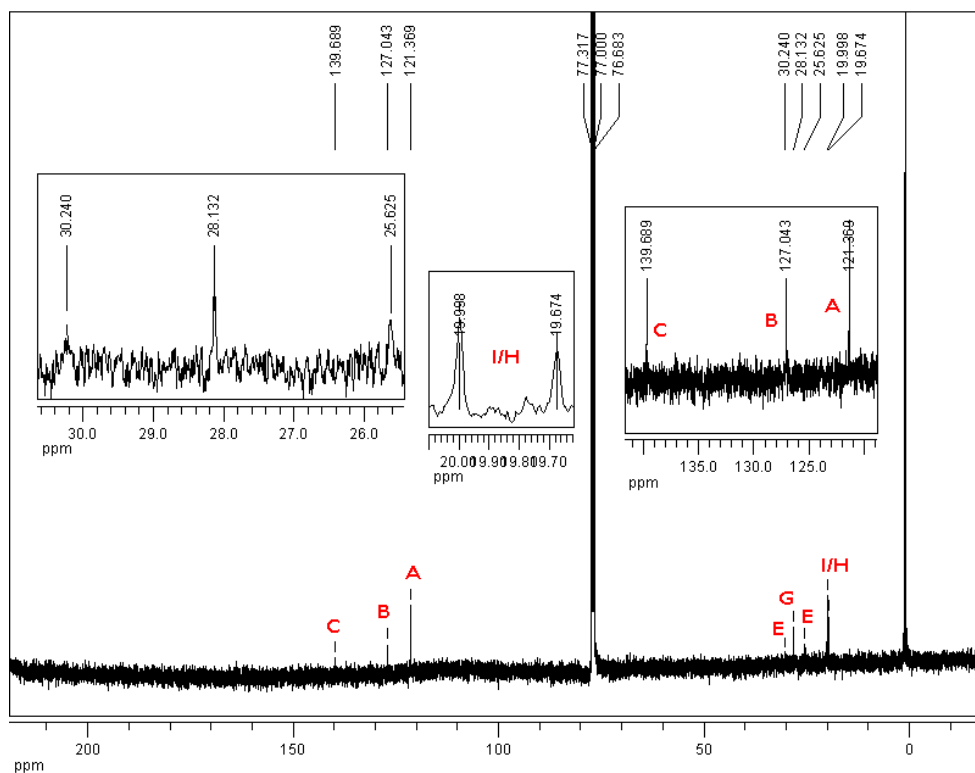


**Figure B18:** <sup>13</sup>C NMR of DMP-s with peak assignments referenced to chloroform at 77.00 ppm.

These features can be explained through the help of HSQC. The full HSQC spectrum is presented in Figure B19. Here, it can be seen that the secondary carbon comes in at about 90.21 ppm, but no peak could be found over the noise.

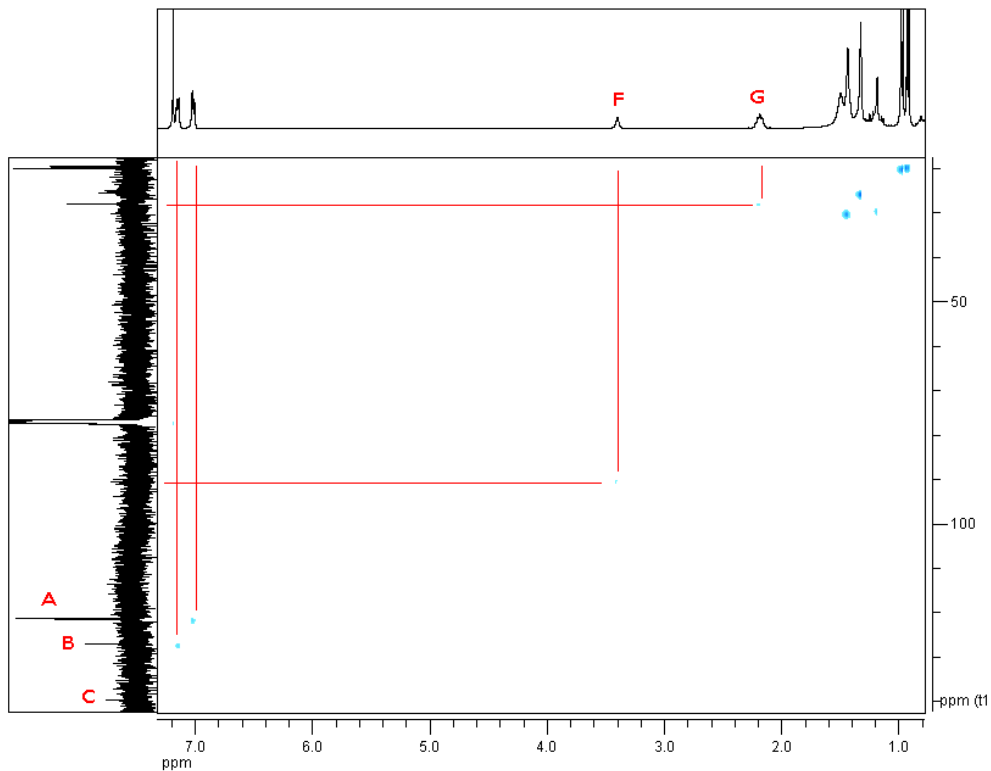


**Figure B19:** Full HSQC 2D NMR spectra of DMP-s with correlation assignments.

Examining the aliphatic region in Figure B20, the two methyl peaks on the TMIO appear as very faint peaks and the two methyl groups resolve independently. The quaternary peak D, on the aromatic ring could not be located.

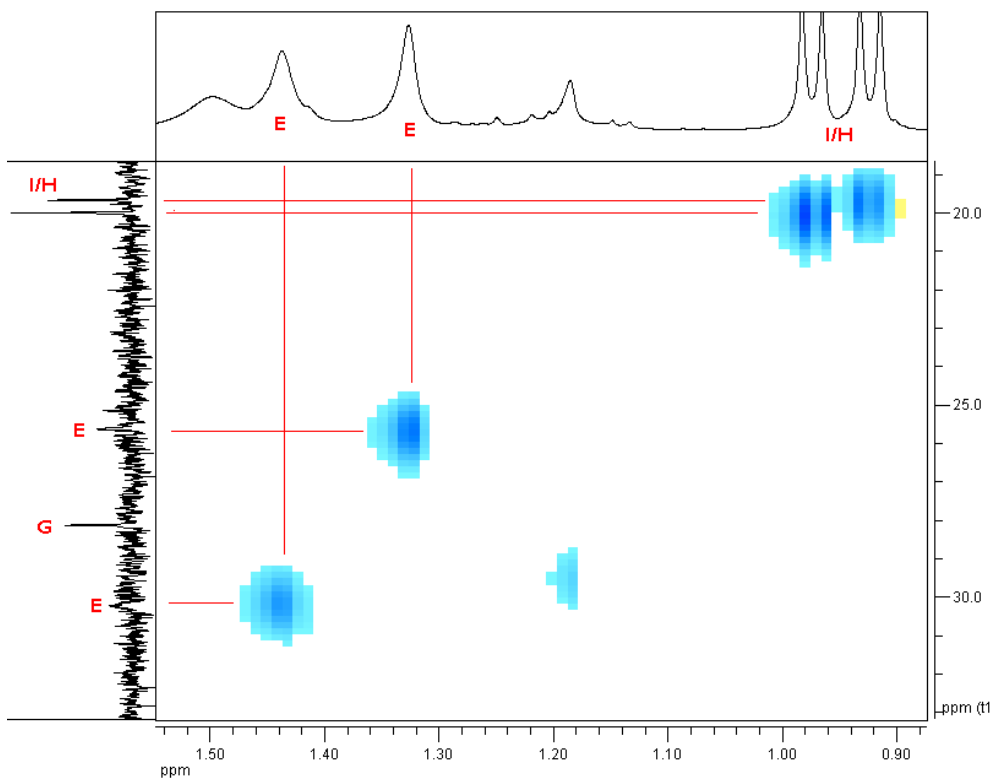


**Figure B20:** Aliphatic region of the HSQC 2D NMR of DMP-s with correlation assignments.

***Mass spectrometry***

Calculated Mass: 289.2406

Mass Found: 289.2416

ppm: 3.6

***Retention time***

38.8 minutes at 4 mL/min of 85:15 MeOH:H<sub>2</sub>O

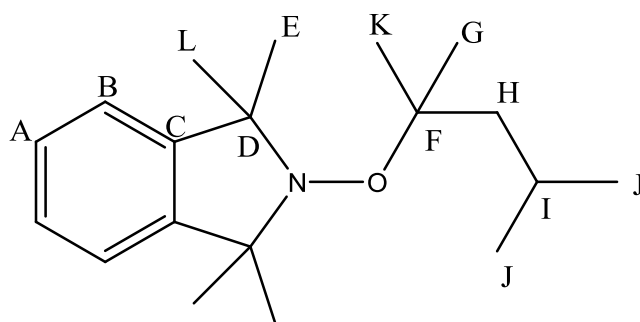


### NMR Peak assignment summary

**Table B3:** Carbon and hydrogen NMR peak assignments for DMP-s.

Position	<sup>13</sup> C Chemical Shift (ppm)	<sup>1</sup> H Chemical Shift (ppm)	Multiplicity	J (Hz)	H Integration
A	121.37	7.09	dd	5.5,3.2	2
B	127.04	7.22	dd	5.5, 3.2	2
C	139.69	-	-	-	-
D	67.18	-	-	-	-
E	30.24	1.51	br s	-	6
E'	25.62	1.4	br s	-	6
F	90.21	3.47	s	-	1
G	28.13	2.26	m	-	2
H	20	1.04	d	7	6
I	19.67	1	d	7	6

### 2-(2,4-Dimethylpentan-2-yloxy)-1,1,3,3-tetramethylisoindoline (DMP-t)



**Scheme B6:** Carbon and hydrogen labeling convention for NMR characterization of the tertiary trapped radical product of 2,4-dimethylpentane (DMP-t).

The tertiary radically trapped product of DMP and TMIO is shown in Scheme B6 with the carbon and hydrogen labeling assignments that will be used throughout its characterization.

There are no stereocenters present in this molecule, nor is it symmetrical like DMP-s.

### *<sup>1</sup>H NMR Peak assignments*

The full <sup>1</sup>H NMR can be found in Figure B21. The aromatic H-atoms resonances are located at their usual positions of 7.08 and 7.22 ppm. There is no down-field resonance for the radically trapped carbon as it is now a quaternary center. In Figure B21 there is an inset of the remaining tertiary center, I, which produces a nonet due to similar coupling constants between the secondary position and the two adjacent methyl groups.

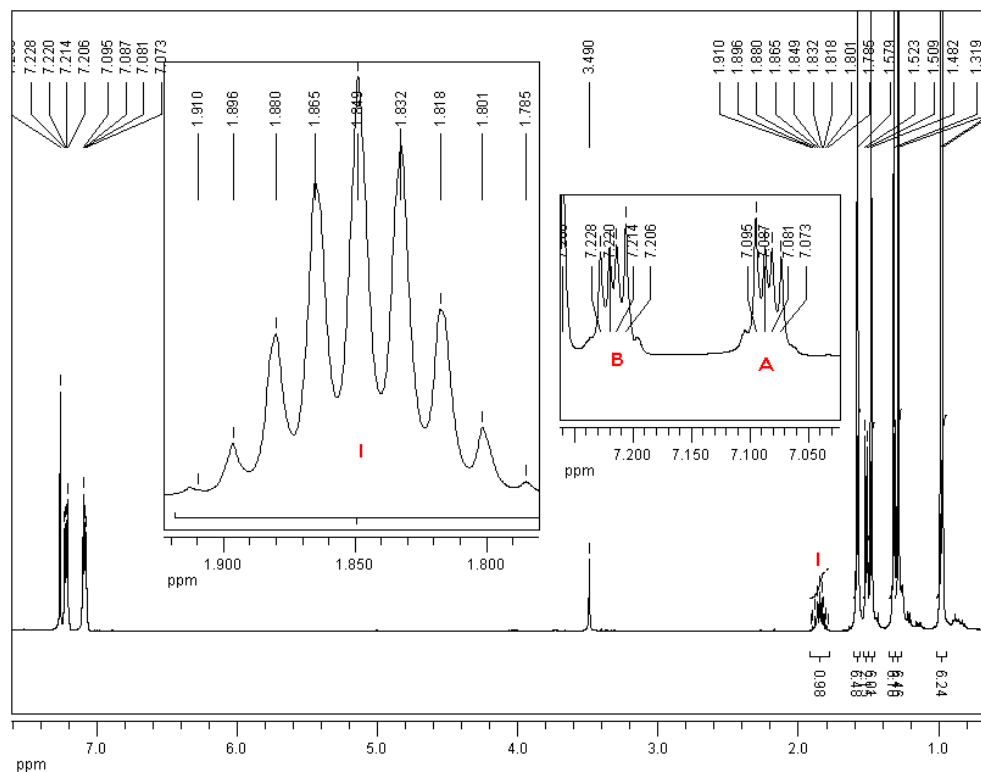


**Figure B21:** Full <sup>1</sup>H NMR of DMP-t with peak assignments referenced to chloroform at 7.26 ppm.

Focusing on the aliphatic region of the  $^1\text{H}$  NMR shown in Figure B22, there are two sharp singlets corresponding to the methyl groups on the TMIO, as well as a doublet for the secondary position, which couples to the tertiary center, I. The two methyl groups adjacent to the newly trapped quaternary center are shifted down-field and appear as two singlets, while the methyl groups adjacent to I appear as a single doublet that integrates for six H-atoms.

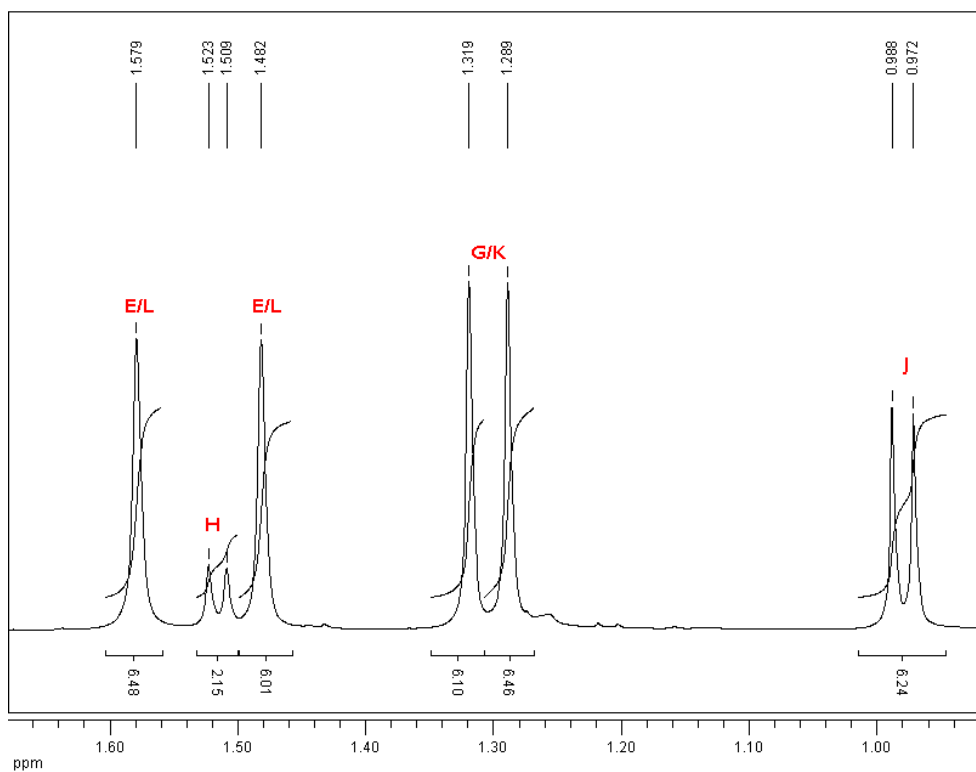


**Figure B22:** Aliphatic region of the  $^1\text{H}$  NMR of DMP-t with peak assignments.

A 2D COSY NMR was also carried out and is shown in Figure B23. The only coupling present is between the tertiary center, I, and the adjacent secondary and methyl positions, as well as aromatic coupling that is not shown.

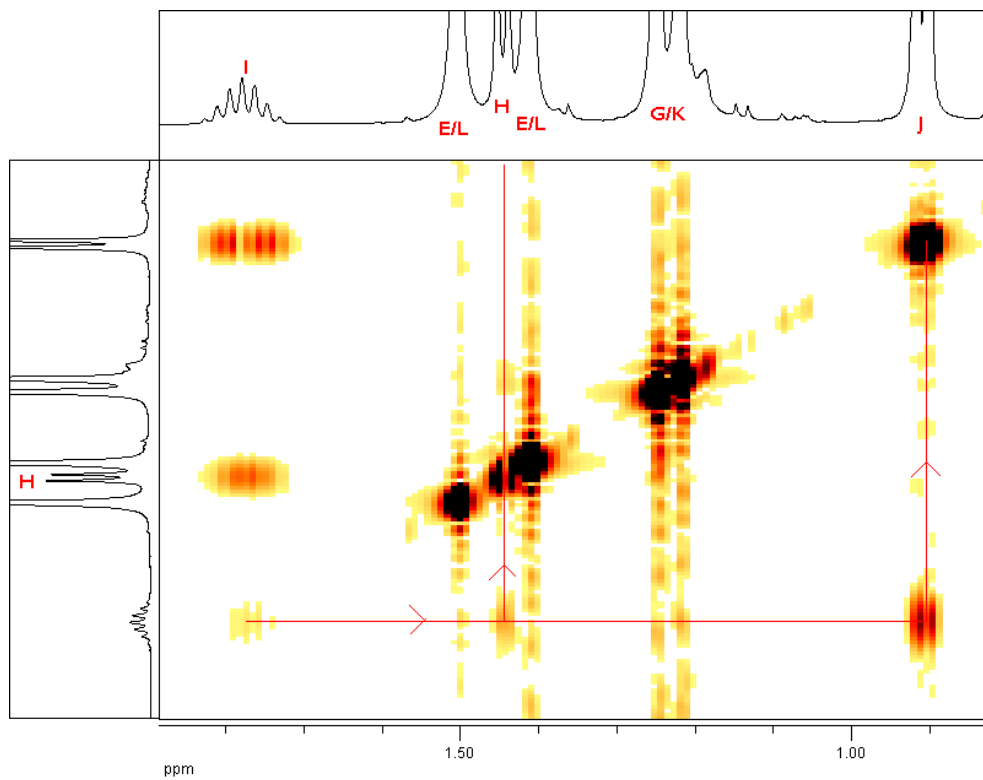


**Figure B23:** COSY 2D NMR of the aliphatic region of DMP-t from 2.00 to 0.60 ppm with peak correlation assignments.

### <sup>13</sup>C NMR Peak assignments

The full carbon NMR can be seen below in Figure B24. The aromatic resonances were assigned analogously to the previous compounds. The resonances for F and D were assigned based on the previous compounds and their chemical shifts.

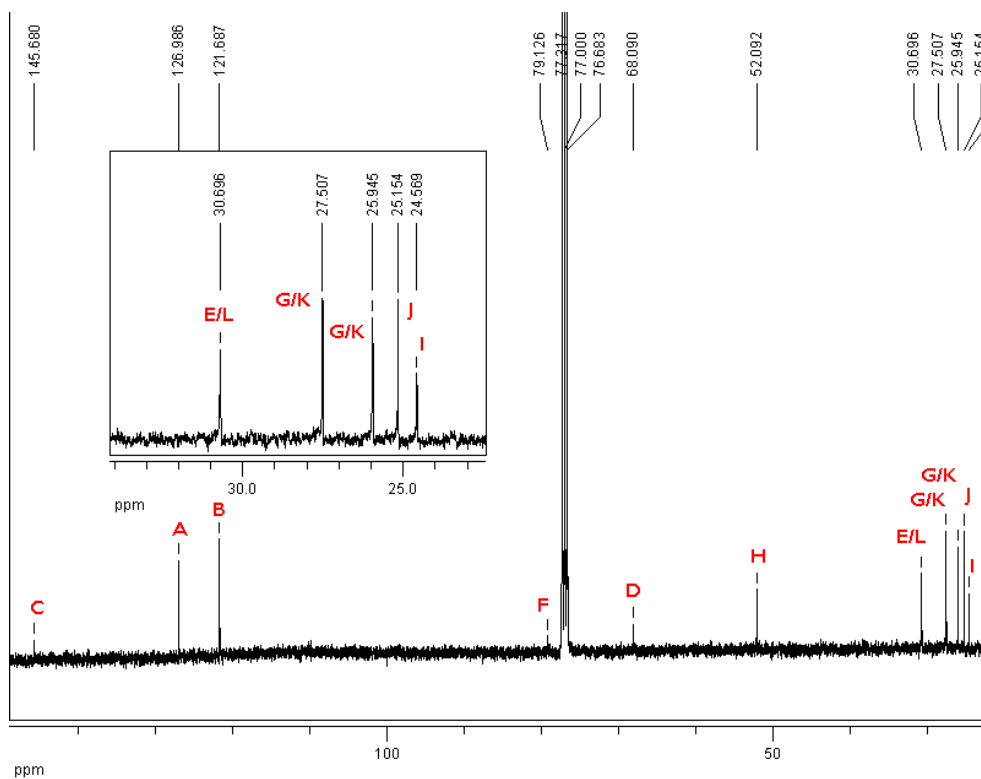


**Figure B24:** Full <sup>13</sup>C NMR spectra of DMP-t with peak assignments referenced to chloroform at 77.00 ppm.

All assignments were also aided by the HSQC spectrum shown in Figure B25.

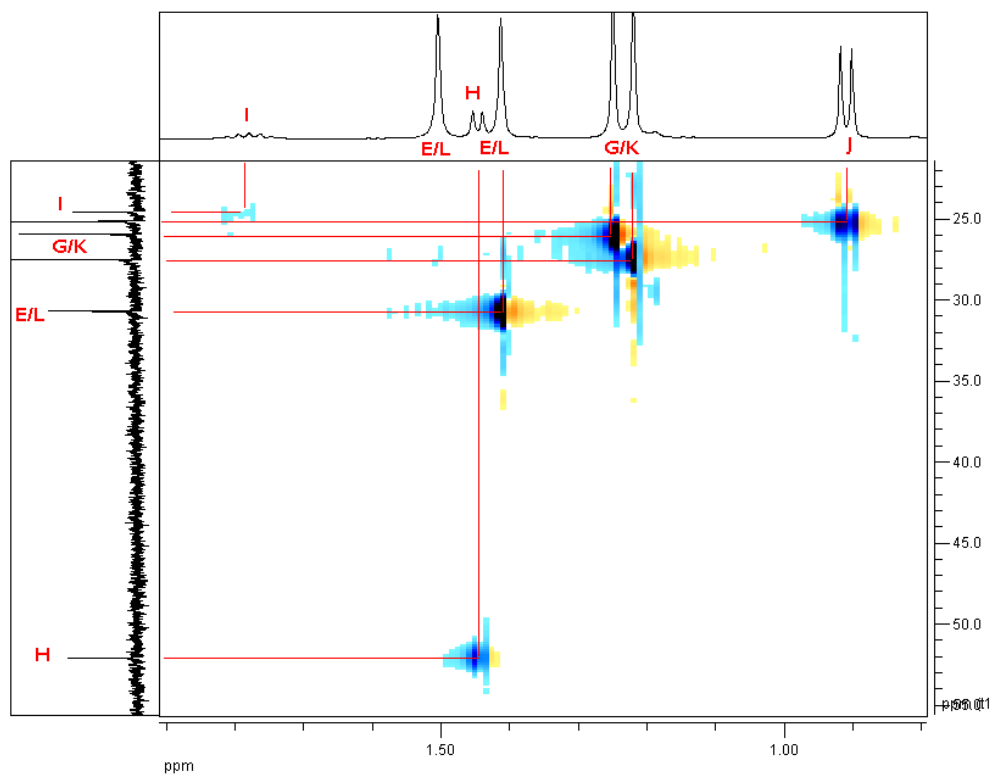


**Figure B25:** Aliphatic region of the HSQC 2D NMR of DMP-t with correlation peak assignments.

***Mass spectrometry***

Calculated Mass: 289.2406

Mass Found: 289.2417

ppm: 3.9

***Retention time***

43.4 minutes at 4 mL/min of 85:15 MeOH:H<sub>2</sub>O

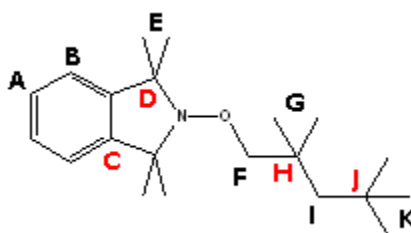
### NMR Peak assignment summary

**Table B4:** Carbon and hydrogen NMR peak assignments for DMP-t.

Position	<sup>13</sup> C Chemical Shift (ppm)	<sup>1</sup> H Chemical Shift (ppm)	Multiplicity	J (Hz)	H Integration
A	126.99	7.08	dd	5.6, 3.2	2
B	121.69	7.22	dd	5.6, 3.2	2
C	145.68	-	-	-	-
D	68.09	-	-	-	-
E	30.7	1.58	s	-	6
F	79.13	-	-	-	-
G	25.947	1.32	s	-	6
H	52.09	1.52	d	5.6	2
I	24.57	1.85	m	-	1
J	25.15	0.98	d	6.7	6
K	30.7	1.29	s	-	6
L	27.51	1.48	s	-	6

### 2,2,4,4-Tetramethylpentane derivatives

#### 1,1,3,3-Tetramethyl-2-(2,2,4,4-Tetramethylpentan-3-yloxy)isoindoline (TMP-p)



**Scheme B4-7:** Carbon and hydrogen labeling convention for NMR characterization of the primary trapped radical product of 2,4-dimethylpentane (DMP-t). Quaternary positions are denoted in red.

The primary radically trapped product of TMP and TMIO is shown Scheme B4-7 with the carbon and hydrogen labeling assignments that will be used throughout its characterization. There are no stereocenters present in this molecule and it is not symmetrical.

### <sup>1</sup>H NMR Peak assignments

The proton NMR is displayed in Figure B26. The aromatic resonances are found in their normal positions at 7.23 and 7.10 ppm. There is a singlet at 3.67 ppm that integrates for two H-atoms and corresponds to the two hydrogens adjacent to the TMIO group at the primary position. The H-atoms at the secondary position create a singlet at 1.42 ppm which overlaps with the broad singlet of the two methyl groups on the TMIO moiety and all together integrate for fourteen hydrogens. The remaining methyl groups on the TMP group integrate for six and nine H-atoms and correspond to the two methyl groups closest to the bridge and the three methyl groups furthest away. There are two impurities present in the sample which could not be removed from the work up, methanol at 3.49 and hexanes at 1.26 ppm.

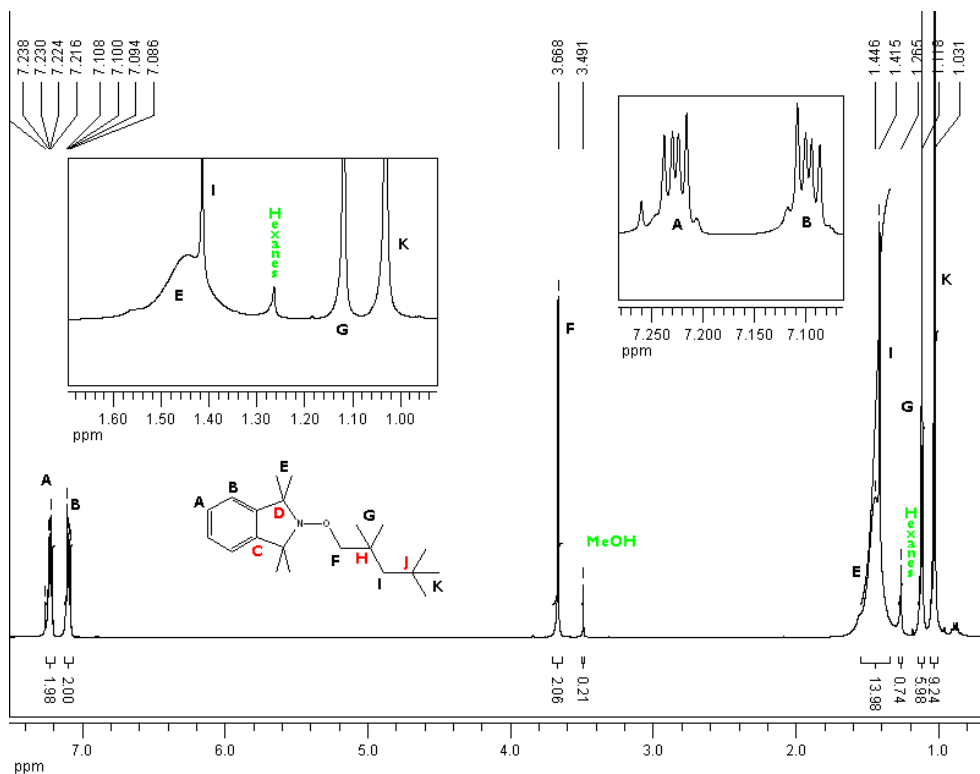


**Figure B26:** <sup>1</sup>H NMR of TMP-p with peak assignments referenced to chloroform at 7.26 ppm.



### <sup>13</sup>C NMR Peak assignments

The carbon NMR assignments can be seen in Figure B27. The aromatic carbons are in their usual positions. The quaternary position adjacent to the nitrogen atom on the TMIO group is also located in its usual position at 67.51 ppm. The bridging carbon is shifted down-field at 88.21 ppm due to the adjacent oxygen atom.

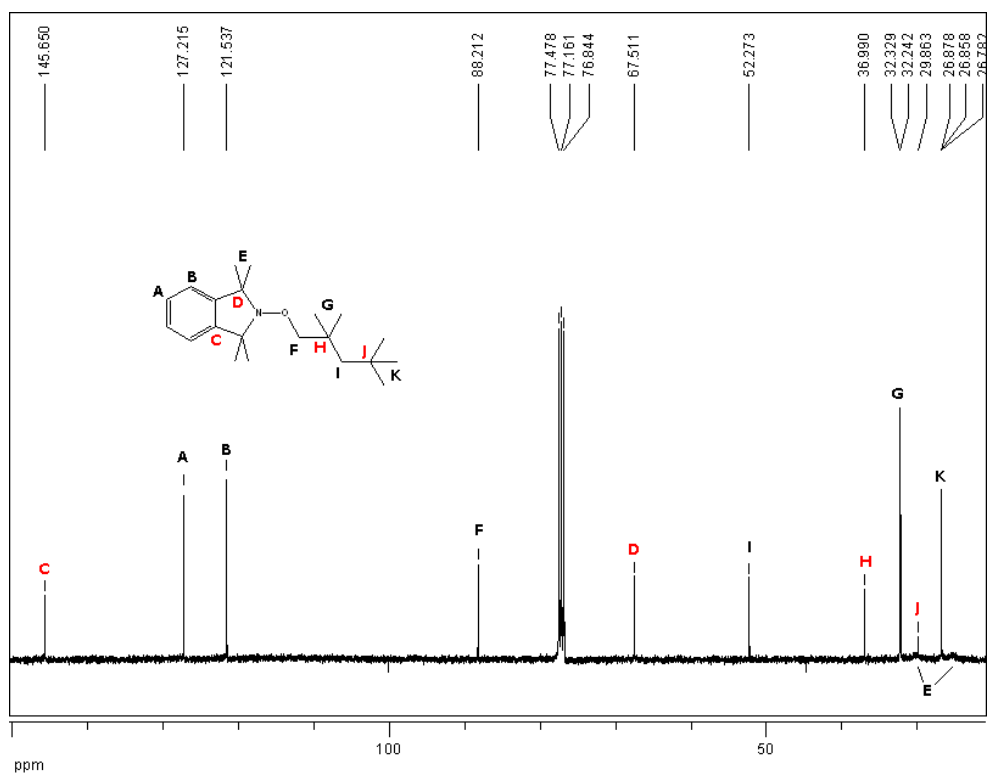


**Figure B27:** <sup>13</sup>C NMR of TMP-p with peak assignments referenced to chloroform at 77.00 ppm.

The assignments in the aliphatic region are straight forward from the HSQC in Figure B28, except for the methyl resonances from the TMIO group. They appear to create two very broad and shallow peaks at about 30 and 23 ppm. Unfortunately the signal to noise ratio is not adequate to clearly define these peaks.

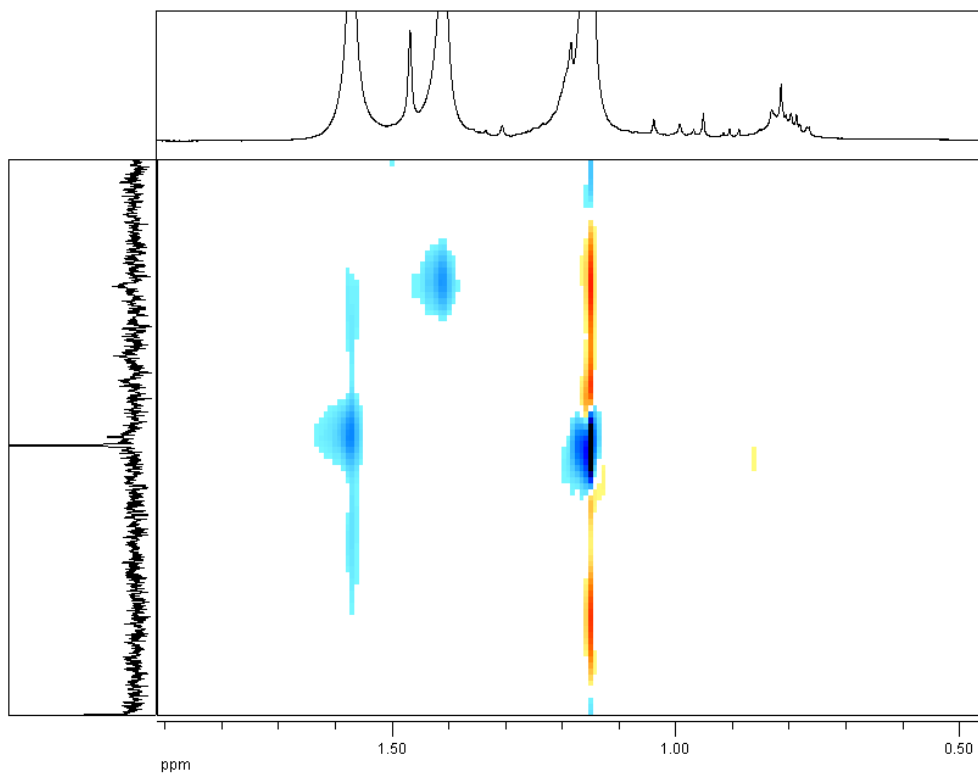


**Figure B28:** HSQC 2D NMR of TMP-p.

***Mass spectroscopy***

Calculated Mass: 317.2719

Mass Found: 317.2731

ppm: 3.9

***Retention time***

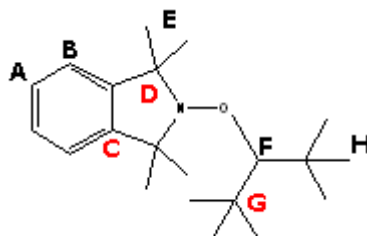
20.7 minutes at 4 mL/min of 90:10 MeOH:H<sub>2</sub>O

### NMR Peak assignment summary

**Table B5:** Carbon and hydrogen NMR peak assignments for TMP-p.

Position	<sup>13</sup> C Chemical Shift (ppm)	<sup>1</sup> H Chemical Shift (ppm)	Multiplicity	J (Hz)	H Integration
A	127.22	7.1	dd	5.5, 3.2	2
B	121.54	7.23	dd	5.5, 3.2	2
C	145.65	-	-	-	-
D	67.51	-	-	-	-
E	-	1.45	br s	-	12
F	88.21	3.67	s	-	2
G	32.24	1.12	s	-	6
H	36.99	-	-	-	-
I	52.27	1.42	s	-	2
J	29.86	-	-	-	-
K	26.782	1.03	s	-	9

### 1,1,3,3-Tetramethyl-2-(2,2,4,4-Tetramethylpentyl-2-yl)isoindoline (TMP-s)



**Scheme B8:** Carbon and hydrogen labeling convention for NMR characterization of the primary trapped radical product of 2,4-dimethylpentane (DMP-t). Quaternary positions are denoted in red.

The labeling formalism that will be used during the characterization of TMP-s can be found in Scheme B8. This molecule is symmetric about the secondary position.

### *<sup>1</sup>H NMR peak assignments*

The <sup>1</sup>H NMR spectra for TMP-s is found in Figure B29. The aromatic H-atoms are found at 7.22 and 7.06 ppm. The hydrogen at the secondary position attached to the bridging C-O bond is found at 3.71 ppm and integrates for one H-atom. The two methyl groups on the TMIO group appear at 1.64 and 1.48 ppm and integrate for six hydrogens each, while the six methyl groups on the TMP portion are found as one singlet at 1.22 ppm. Unfortunately there is a hexanes impurity that overlaps with the six methyl groups and interferes with the integration but it is unmistakably the correct peak.

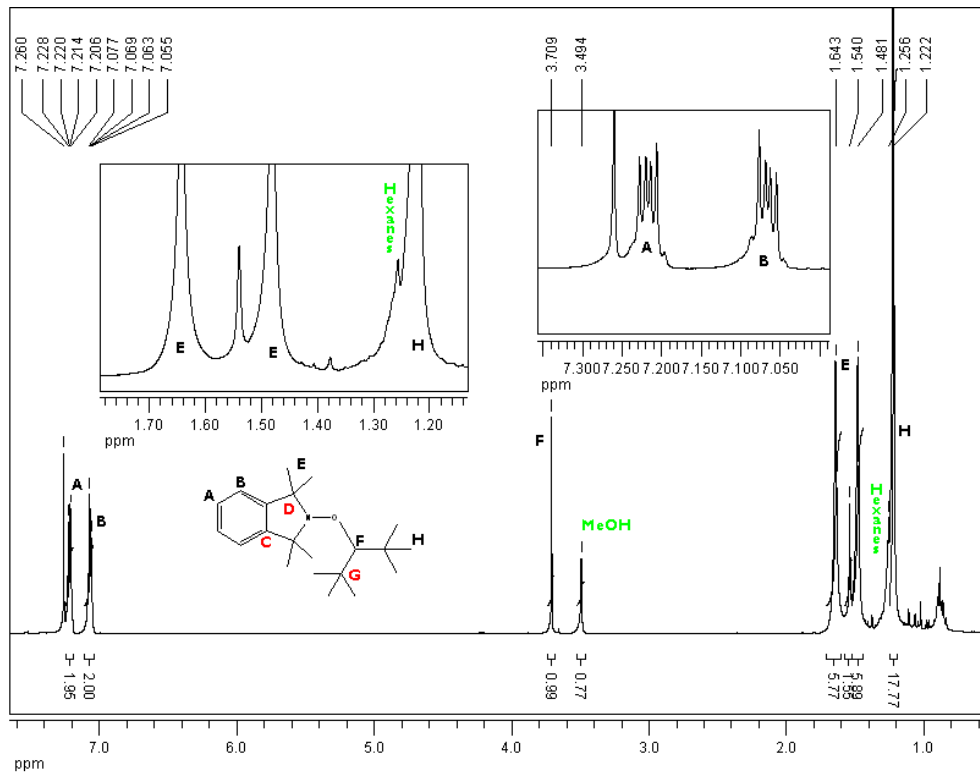


**Figure B29:** <sup>1</sup>H NMR of TMP-s with peak assignments referenced to chloroform at 77.00 ppm.

### <sup>13</sup>C NMR Peak assignments

The characterization for the carbon NMR spectra is shown in Figure B30. The aromatic resonances are at their normal positions as well as the quaternary group adjacent to the nitrogen atom in TMIO. The bridging carbon at the secondary position is found at 93.04 ppm, shifted down-field by the adjacent oxygen atom. The six methyl groups on the TMP appear as one peak at 31.54 ppm while the quaternary carbons on TMP are present at 38.83 ppm. Similar to the <sup>13</sup>C NMR of TMP-p, the two methyl groups on the TMIO group form broad peaks.

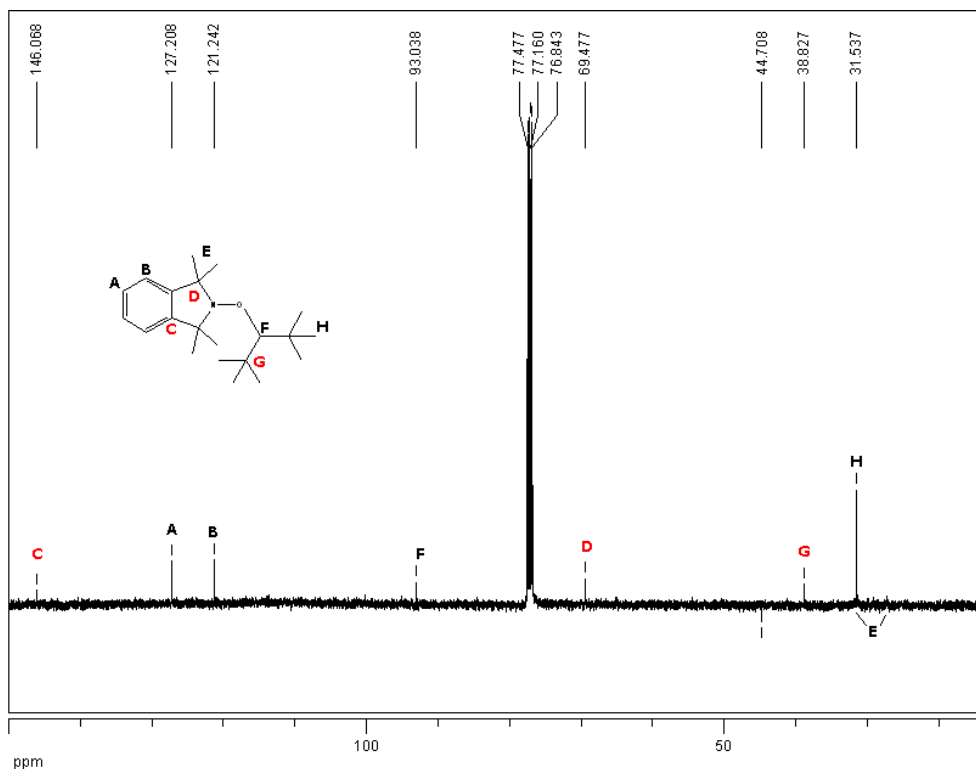


**Figure B30:** Full <sup>13</sup>C NMR of TMP-s with peak assignments referenced to chloroform at 77.00 ppm.

These broad peaks can be seen more clearly in the HSQC of the aliphatic region shown below in Figure B31.

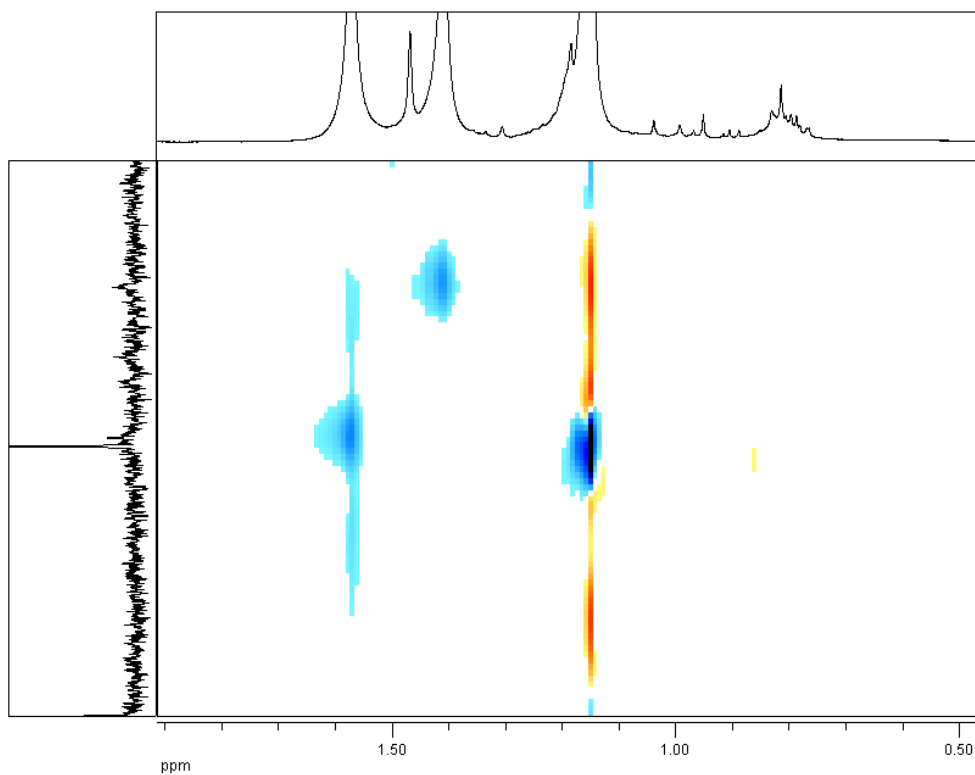


**Figure B31:** Aliphatic region of the HSQC 2D NMR of TMP-s.

***Mass spectroscopy***

Calculated Mass: 317.2719

Mass Found: 317.2727

ppm: 2.6

***Retention time***

25.7 minutes at 4 mL/min of 90:10 MeOH:H<sub>2</sub>O

*NMR Peak assignment summary*

**Table B6:** Carbon and hydrogen NMR peak assignments for TMP-s.

Position	<sup>13</sup> C Chemical Shift (ppm)	<sup>1</sup> H Chemical Shift (ppm)	Multiplicity	J (Hz)	H Integration
A	127.21	7.22	dd	5.6, 3.2	2
B	121.24	7.07	dd	5.6, 3.2	2
C	146.07	-	-	-	-
D	69.48	-	-	-	-
E	-	1.64, 1.54	s	-	6, 6
F	93.04	3.71	s	-	1
G	38.83	-	-	-	-
H	31.54	1.22	s	-	18